The Pennsylvania State University

The Graduate School

College of Engineering

THE PROPERTIES AND 3D STRUCTURE OF MEDIUM SCALE TRAVELING IONOSPHERIC DISTURBANCES

A Dissertation in

Electrical Engineering

by

Ilgın Şeker

Submitted in Partial Fulfillment
of the Requirements
for the Degree of

Doctor of Philosophy

August 2009

The dissertation of Ilgın Şeker was reviewed and approved* by the following:

John D. Mathews
Professor of Electrical Engineering
Dissertation Advisor
Chair of Committee

C. Russell Philbrick
Professor of Electrical Engineering

Julio V. Urbina
Assistant Professor of Electrical Engineering

Eugene E. Clothiaux
Associate Professor of Meteorology

W. Kenneth Jenkins
Professor of Electrical Engineering
Head of the Department of Electrical Engineering

*Signatures are on file in the Graduate School

ABSTRACT

Perhaps the most persistent and prominent of the mid-latitude ionospheric phenomena are the Medium-Scale Traveling Ionospheric Disturbances (MSTIDs) in the F-region that are usually observed when geomagnetic activity is low. These MSTIDs have been identified and associated with various other phenomena such as plasma depletion bands, plasma bubbles, ionospheric slabs, and thermospheric waves. Using a combination of instruments to simultaneously observe these MSTIDs proves to be useful. In particular, allsky images provide the horizontal information complement to the narrow-beam Incoherent Scatter Radar (ISR) vertical and (nearly vertical) azimuth-scanned profiles.

A new description of the 3D geometry of these structures is presented. This model-based description results from using a specific observational technique that is based on combined or fused ISR and allsky imager observations that define the horizontal and vertical features of night-time F-region MSTID structures over the Arecibo Observatory (AO) in Puerto Rico. This is the first application of the azimuth-scanning radar data combined with the imager data to develop the picture of the electrodynamic structures in the ionosphere. In particular, by using the azimuth-scanning ISR data and allsky images together, this research has shown for the first time that the southern part of an MSTID band reaches higher altitudes than its northern part implying that the MSTID bands are vertically tilted towards but not aligned with the orientation of the geomagnetic field lines. To confirm and further investigate these findings on the 3D structure of MSTID bands, a simple empirical 3D model of night-time MSTID bands is constructed. This empirical model is intended to show the bubble shape of MSTID bands in 3D and to replicate both the azimuth-scanning ISR and the allsky imager observations.

Furthermore, the model is especially useful in explaining how these complex structures appear in azimuth-scanning ISR data. In particular, the causes of various complex features seen in the azimuth-

scanning ISR data, such as the packets of thinner spikes, mirror-spikes, and high-altitude striations, are easily explained using the model. For example, it was found that MSTID bands are both uplifts and depletions and that the high-altitude striations seen in the azimuth-scanning ISR data can be caused either by the MSTIDs or the midnight collapse. Also, ISR and allsky imager results derived from the model are compared with the actual observations to confirm that the model is valid and to better understand various properties of MSTIDs.

The results of the empirical model provide clues on what to expect from the theoretical models of geomagnetically quiet, nighttime, mid-latitude, F-region electrodynamics. Finally, the technique described here is not limited to F-region or mid-latitudes only. It can be applied to any other ionospheric phenomenon which can be observed by both radar and imager.

TABLE OF CONTENTS

LIST OF FIGURES

LIST OF TABLES

LIST OF ABBREVIATIONS

AACGM	Altitude Adjusted Corrected Geomagnetic Coordinates
AO	Arecibo Observatory
BW	Brightness Wave
CCD	Charged-Coupled Device
COFIs	Coherent Omnipresent Fluctuations in the Ionosphere
CSSL	Communications and Space Sciences Laboratory
ESF	Equatorial Spread-F
EUV	Extreme Ultra-Violet
FOV	Field of View
FPI	Fabry-Perot Interferometer
GPS	Global Positioning System
GUVI	The Global Ultraviolet Imager
IDL	Interactive Data Language
IMAGE	Imager for Magnetopause-to-Aurora Global Exploration
ISR	Incoherent Scatter Radar
Kp	Geomagnetic Activity Index
MS	Master of Science
MSTID	Medium Scale Traveling Ionospheric Disturbances
MTM	Midnight Temperature Maximum
MU	Middle and Upper Atmosphere Radar
NSF	National Science Foundation
PHD	Doctor of Philosophy
PSASI	Penn State Allsky Imager
PSU	The Pennsylvania State University
RTI	Range Time Intensity
SUPIM	The Scheffield University Plasmasphere Ionosphere Model
SNR	Signal-to-Noise Ratio
TEC	Total Electron Content
TID	Traveling Ionospheric Disturbances
TIMED	Thermosphere Ionosphere Mesosphere Energetics and Dynamics Satellite

ACKNOWLEDGEMENTS

First of all, I would like to express my gratitude to my encouraging and supportive adviser Prof. John D. Mathews for all the resources, mentoring, and guidance he provided throughout my Ph.D. studies. Without him, none of this would be possible.

I am thankful to my committee members Prof. C. Russell Philbrick, Prof. Julio V. Urbina, and Prof. Eugene E. Clothiaux for their constructive comments and suggestions, and for sharing their expertise with me. Also thanks to my colleagues Dorey J. Livneh and Qina Zhou with whom I have collaborated on several papers. Furthermore, I appreciate the constant support of my colleague Akshay Malhotra, who kept encouraging and motivating me. I would also like to express my appreciation to Prof. Jonathan J. Makela for his insights and endless efforts in helping me learn the field of allsky imaging.

This effort was supported under NSF Grant ATM 07-21613 to the Pennsylvania State University. The Arecibo Observatory is part of the National Astronomy and Ionosphere Center, which is operated by Cornell University under cooperative agreement with the National Science Foundation. I would like to thank many members of the Arecibo Observatory staff including Raul Garcia, Craig Tepley, Jonathan Friedman, Nestor Aponte, Angel Vazquez, and Sixto Gonzalez for their constant support.

Special thanks to my mother Ayşe Bülbül and brother Çağıl Şeker for all the unconditional encouragement and support they provided. Without them this journey would not even start. And finally, I would like to express my gratitude to a very special person, Zeynep Sıla Yalçın. Without her constant moral support and encouragement, this journey would be much more difficult for me. She has always been nearby radiating her positive thoughts and giving me a different perspective when I much needed it.

1. INTRODUCTION

This chapter provides the background necessary to understand the results presented in this dissertation which involves the study of Medium-Scale Traveling Ionospheric Disturbances (MSTIDs) using allsky imager and radar. First, the ionosphere and airglow science are introduced to give an idea on the core science involved. Then, the two instruments used in this study, the Penn State Allsky Imager (PSASI) and the Incoherent Scatter Radar (ISR) at Arecibo Observatory (AO), are briefly introduced and followed by a summary of allsky imager observations of the mid-latitude F-region. Afterwards, general properties of MSTIDs, along with various instruments and techniques used to observe them, are reviewed. Two research questions are posed at the end of the chapter. It should be noted that, since this dissertation is a continuation of the Ph.D. candidate's M.S. thesis (**Seker, 2006**), the first three of the eight sections in this introduction chapter (ionosphere, airglow, and PSASI) are mostly taken from there.

In Chapter 2 the radar and imager datasets are introduced followed by a description of the fusion technique used to combine them and the empirical 3D model based on that. In Chapter 3, the observational findings derived from this technique along with the model results are presented and compared with each other. The last chapter starts with a detailed discussion of these findings and concludes with a discussion of the results and their significance with respect to mid-latitude ionospheric electrodynamics.

1.1. Ionosphere

The ionospheric region is a most interesting and important part of the upper atmosphere. In the ionosphere, many factors play roles in creating the various interesting phenomena occurring there. Ionization by solar radiation is the primary source of ion production above 90 km as O_2, N_2, and O are photoionized by EUV radiation. At lower altitudes, X-rays, energetic particles, and cosmic radiation impinge on specific species with low ionization potential, resulting in ionization. Ionization is followed by many different ion chemical reactions which produce other ions. This occurs while preserving a large scale (greater than Debye sphere) charge neutrality, which is a primary characteristic of plasma. Ion-electron recombination as well as ion-neutral reactions in the ionosphere gives rise to excited states and airglow at specific wavelengths. Airglow emissions are similar to the optical emission in auroras, except the initial excitation source is solar photons instead of the energetic particles in aurora. **Figure 1.1a** shows the neutral atmosphere layered structure, which is defined by the temperature profile, and **Figure 1.1b** shows the daytime and nighttime ionosphere charge density profiles which are defined by the electron concentration. The D-layer (~60-90 km) peaks around 90 km. The D-region plasma electrons form negative ions which are destroyed at night by photodetachment at visible wavelengths, associative detachment, and mutual neutralization. The E-layer extends between ~90 km and ~140 km and peaks around 110 km. The primary loss of E-region ions is due to dissociative recombination of O_2^+ and NO^+. In this region, there exist thin patches of longer lifetime metallic ions extra ionization that form the so called sporadic-E layer. These longer life ions are effectively laid by **V**×**B** forces from the neutral wind shear. The F1-layer is at ~140-200 km and peaks around 200 km; however it only exists during daytime. Here N_2^+ and O^+ ions charge transfer to form NO^+ and O_2^+. This molecular ionization disappears rapidly by dissociative recombination. F2-Layer is around ~200-500 km and peaks at ~300 km. Large variations might occur in this region which persists during the nighttime. The ionization of O dominates this region. Topside ionosphere is dominated by O^+, and the plasmasphere at higher altitudes mostly consists of H^+. As **Figure 1.1b** illustrates, at nighttime, the D-layer and the F1-layer disappear due to recombination of the molecular ions leaving a weak E-layer and a single F layer behind.

The ionosphere is not a stable, calm, homogenous region. Its composition and structure varies temporally with diurnal, seasonal, and solar cycle variation, and also spatially with latitude and altitude. It is also affected by the changes in the atmosphere, magnetosphere, and solar events. Many different phenomena are seen in the ionosphere such as the equatorial (Appleton) anomaly, equatorial electrojet, Sq current system, fountain effect (**Appleton, 1946; Hanson and Moffett, 1966; Forbes and Lindzen, 1976; Forbes, 1981; Jursa 1985; Tascione, 1994**), gravity waves (**Philbrick, 1985; Taylor, 1997**), mesospheric bores (**Taylor et al., 1995**; **Smith et al., 2003**), sporadic-E (**Mathews, 1998; Mathews et al., 2001a**; **Kelley et al., 2003a**), equatorial spread-F (ESF) plumes (**Chaturvedi and Ossakow, 1977**; **Mendillo et al., 1997**; **Mathews et al., 2001b**; **Makela et al., 2004**; **Makela, 2006**), traveling ionospheric disturbances (TIDs) (**Mendillo et al., 1997**; **Kelley et al., 2000b**; **Kelley et al., 2002**), midnight temperature maximum (MTM) and brightness waves (BW) (**Herrero and Meriwether, 1980**; **Colerico et al., 1996**; **Mendillo et al., 1997**). Examples of various F-region phenomena observed at mid-latitudes are given in **Section 1.5.**

1.2. Airglow

The airglow is weak emission of visible light by the Earth's atmosphere, which means that the night sky is never completely dark. It was first noticed in 1868 by Anders Ångström. It can also be defined more technically as the quasi-steady radiant emission from the upper atmosphere over middle and low latitudes, to be distinguished from the sporadic emission of auroras that occur over high latitudes. Airglow is a photochemical luminescence arising from chemical reactions in the upper atmosphere. An excellent book on early studies of airglow and aurora is available for detailed information (**Chamberlain, 1961**). **Figure 1.2a** shows an example of airglow spectra in optical wavelengths (**Broadfoot and Kendall, 1968**). Two of the OI emission lines in the figure at 630 nm and 557.7 nm, as well as the near infrared line at 777.4 nm, are the wavelengths observed by the PSASI instrument.

The responsible thermospheric chemical reactions that create the optical emissions at two of the three different wavelengths which PSASI can observe are:

$O^+ + O_2 \rightarrow O_2^+ + O$ Charge Exchange **(1.1)**

$O_2^+ + e^- \rightarrow O^* + O$ Dissociative Recombination **(1.2)**

The rates of these reactions depend both on plasma height and number density as well as the neutral atmosphere and atomic oxygen concentrations. The excited atomic oxygen (O*) may be in either the $O(^1D)$ or $O(^1S)$ states resulting in the corresponding OI emission. The $O(^1D)$ state emission is at 630 nm, the deep-red end of the visible spectrum with a lifetime of ~110 s. As **Figure 1.2b** shows, 630 nm airglow emission peaks around ~250 km altitude providing information on the F2-region (**Ogawa et al., 2002**). The $O(^1S)$ state emission is located at 557.7 nm, in the green, with ~1 s lifetime, but yielding only ~15% of the photon emission rate when compared with 630 nm emission (**Makela et al., 2001b**). Although the allsky images from the 557.7 nm emission can occasionally show intense F-region structures, this emission has a significant mesospheric component (proportional to $[O]^3$, so mostly around ~96 km in the E-region), so it can be used to analyze both F-region (e.g., depletions, plumes) and mesospheric (e.g., gravity waves) events.

The responsible mesospheric chemical reactions for 557.7 nm emission are:

$O + O + M \rightarrow O_2^* + M$ **(1.3)**

$O_2^* + O \rightarrow O_2 + O^*$ **(1.4)**

$O^* \rightarrow O + hv$ **(1.5)**

Lastly, 777.4 nm emission is predominantly a result of the following reaction:

$$O^+ + e^- \rightarrow O^* + hv \qquad \text{Radiative Recombination} \qquad \textbf{(1.6)}$$

Since O^+ is the dominant plasma constituent near the F peak, we can assume that $[O^+]$ is equal to $[e^-]$. Thus, the photon flux emitted at 777.4 nm is approximately proportional to the electron number density squared, n_e^2. The emission is from around the F-peak, which is at ~300 km. While generally associated with auroral zone airglow features, this emission has been observed at AO.

Clearly, monitoring these emissions provides the 2-D mesoscale context related to ionosphere height/concentration, and the ISR and other AO instruments provide the vertical component to enable studies of the phenomena occurring in the ionosphere.

1.3. Penn State Allsky Imager (PSASI)

With the development of high-quality image-intensified cameras and highly sensitive charge-coupled devices (CCDs), which replaced the traditional film for recording photons, a new era of observing the optical emissions associated with the ionosphere has started. These CCDs are used in newly emerging instruments called “allsky imagers” which can now provide large-scale, instantaneous, two-dimensional, digital snapshots of the ionosphere; whereas almost all the previously developed instruments (e.g., ionosonde, radar, photometer, FPI, GPS, satellite, rockets, etc.) can record a quantity along just a single look angle at a given time. Due to their high sensitivities, CCDs are also capable of recording faint emissions, which in turn allows the use of shorter integration times, providing higher temporal resolutions. These features of CCDs are what make allsky imaging a precious modern tool to investigate the ionosphere (**Makela, 2006**).

The Penn-State All-Sky Imager (PSASI), a high-resolution optical imaging instrument which has been operating since April 2003, is installed at Arecibo Observatory (AO), Puerto Rico (AO: 18.3° N, 66.75° W, altitude 350 m, L = 1.43 at 300 km, dip angle 46°, geomagnetic latitude 31.5° N). It is controlled remotely and maintained by the Communications & Space Sciences Laboratory (CSSL) at the Penn State University (PSU) under several National Science Foundation (NSF) grants. Even though it is operated by CSSL, it is a public-access instrument and access is provided by means of a MAC Apache server hosting a public website which is updated automatically whenever new data are available. Allsky imager data for more than three years are available online (allsky.ee.psu.edu) and are being used to study various ionospheric phenomena.

PSASI is an allsky imager based on a CCD camera, enhanced by many lenses and a fish-eye lens at the end, allowing a 180° field-of-view. **Figure 1.3** shows a photo of PSASI and the basic schematic of its optical system. The fish-eye lens creates the barrel distortion, which is the main distortion in the images due to the mapping of the image from a 180° FOV to a planar surface. As a result, the shapes are distorted near the edges. The edges also look brighter than the central region due to longer path lengths and thus larger line-of-sight emissions at low elevation angles (Van Rhijn effect). More detailed information about various distortions and how to correct for them is given in Section 2.2 of **Seker (2006)**.

PSASI is a passive device and it continuously takes images serially of the whole sky at distinct emission frequencies by means of a filterwheel. PSASI is designed to autonomously record the airglow (on moonless nights when the faint emissions are relatively observable), which occurs in the ionosphere due to many chemical recombination reactions. The airglow intensity, recorded as images and movies, provides information about the density and the dynamics of the emission relevant ions, which in turn reveal the details of some important ionospheric events and irregularities. These data show the phenomena of the plasma depletions and enhancements in the allsky images. The imager is being used primarily to monitor E-region (e.g., mesospheric waves and bores) and mesoscale F-region (e.g., spread-F plumes, MSTIDs, midnight collapse) processes using the 180° field-of-view (FOV) primary lens and 557.7-nm, 630.0-nm, and 777.4-nm narrowband filters at typically 60 sec. integrations. More details on PSASI and allsky imaging in general are also available in **Seker (2006)**.

Arecibo Observatory was a natural choice for the imager because the site is geographically in the tropics and at geomagnetic mid-latitudes, which allows observations of mid/low latitude ionospheric phenomena. **Figure 1.4** shows the geomagnetic field line geometry associated with the site and the coverage of the imager (limited to 150º field of view) assuming an emission height of 300 km. The site also has an Incoherent Scattering Radar (ISR) along with many other passive and active instruments (such as FPI, photometer, lidar, magnetometer, etc.) to observe the ionosphere, which allows the fusion of data from multiple instruments.

1.4. Incoherent Scatter Radar (ISR) at Arecibo Observatory (AO)

The usual procedure established for determining the electron concentration profiles has been the ionospheric sounding technique (the ionosonde, a swept-frequency radar), which is based on the time-delay of the coherently back-scattered radio-echos. The time-delay depends on the reflection height, which in turn depends both on the electron concentration and the frequency of the radio pulse. So, by sweeping the frequency of the transmitter, the electron concentration at different heights can be calculated using the time-delay of the echo. However, this technique has a major drawback. Since the radio waves do not reflect above the altitude of the maximum electron concentration, it is not possible to probe beyond the peak of the F2-region.

On the other hand, the incoherent scattering radar (ISR) can measure above the F-peak as it is based on the weak incoherent scatter from the electrons in the ionosphere. A detailed theoretical explanation of incoherent scatter radar is given by **Mathews (1984)**. Since incoherent scatter is from individual electrons, the waves do not constructively interfere with each other resulting in a weak return signal. The weak signal requires that the transmitter power must be high and antenna gain large for the ISR to detect the small backscatter power (**Tascione, 1994**). The electron concentration can be calculated from the intensity of this return echo which is proportional to the number of scatterers (electrons) in the volume illuminated by the ISR beam. As with the ionosonde, the scattering height is measured by the time delay. As the electrons in the ionosphere have random thermal motions, the doppler shifted return signal covers a range of frequencies. Furthermore, the various ions in the ionosphere interact with the electrons and alter their motion. Consequently, in addition to the electron concentration, the temperatures and line-of-sight drift velocities of the electrons and ions can also be calculated from the shape and central frequency of the spectrum of the return echo, which depends on these two factors.

The Arecibo Telescope, which is shown in **Figure 1.5**, was built in 1963. It can be operated at frequencies from 50 MHz up to 10 GHz (3 cm – 6 m wavelength) in receive (radio astronomy mode). In radar mode it has a very large signal-to-noise-ratio (SNR) in addition to high temporal (10 ms) and range (150 m) resolution due to its high transmit power (2.5 MW at 430 MHz) and the large size of its dish. In fact, AO ISR is the world's largest single-dish telescope with a diameter of 305 m (1000 feet) resulting in a very narrow beam-width (~1 km width at 300 km range). Since the focus of the spherical dish is along a line rather than a single point (which would be the case for a parabolic reflector), a 96-foot linefeed tuned to 430 MHz is used both as a transmitter and a receiver. The AO ISR actually has another radar feed for ionospheric studies: the Gregorian reflector (which focuses the waves at a single point). Both of these radars (which can be seen in **Figure 1.5**) can be operated in either fixed-zenith (vertical-beam with 0° zenith angle) or azimuth-scanning (beam-swinging) mode. For azimuth-scanning mode, the zenith angle is limited by mechanical constraints to within 20° and is usually kept at 15° to avoid interference with local broadcasts at radio frequencies and to improve gain. The ISR range-time-intensity (RTI) plots shown in **Figures 2.1b** and **3.1** are obtained using a Barker code technique (**Mathews, 1986**), time-averaged (downsampled to 10 s and 40 s for the fixed-beam and azimuth-scanning datasets respectively), and processed to remove noise, meteors, and interference (**Wen et al., 2006**) and converted to signal temperatures (power expressed in Kelvins) from the relative incoherent scatter strength (signal plus noise) (**Livneh, 2009**).

1.5. Allsky Imager Observations of the Mid-Latitude F-region

Allsky imagers have been extensively used at high-latitudes to observe the aurora and at low-latitudes to observe the plasma depletions (such as equatorial spread-F) by means of the 557.7-nm, 630.0-nm, and 777.4-nm airglow emissions. **Makela (2006)** gives a detailed review of imager observations of ionospheric irregularities at low-latitudes. Although plasma irregularities at low-latitudes have been observed using imagers since 1981 (**Moore and Weber, 1981**), the imaging technique has been applied to mid-latitudes only in the last decade revealing that the mid-latitude F-region is also active with plasma depletions such as Medium-Scale Traveling Ionospheric Disturbances (MSTIDs) and spread-F plumes; and plasma enhancements such as Midnight Temperature Maximum (MTM), Brightness Waves (BW), enhanced spread-F plumes, and mesospheric gravity waves (**Mendillo et al., 1997; Garcia et al., 2000; Kelley et al., 2000b, 2002; Shiokawa et al., 2003b; Otsuka et al., 2003; Seker et al., 2007**).

The most prominent F-region events among these, MSTIDs, appear in the allsky images as periodic dark bands aligned northwest to southeast and propagating southwest in the northern hemisphere (**Figure 1.6a**). Since this dissertation is on MSTIDs, a separate section (**Section 1.6**) is devoted to a detailed introduction of this phenomenon. A well studied low-latitude F-region irregularity feature is equatorial spread-F (ESF), depletions which are formed due to the Rayleigh-Taylor Instability at equatorial latitudes where the geomagnetic field lines are horizontal (**Makela, 2006**). Surprisingly, similar structures have been recently observed at mid-latitudes also (**Figure 1.6b**). Allsky images reveal that these spread-F plumes appear from south of AO, and only when the geomagnetic activity (i.e., Kp) is high, whereas MSTIDs appear only when Kp is low (though MSTIDs are not always observed when Kp is low). This suggests that somehow equatorial spread-F plumes reach mid-latitudes when geomagnetic activity is high, but it has not been possible to prove this yet due to the limited coverage of a single allsky imager. Furthermore, like ESF plumes and unlike MSTIDs, these mid-latitude plumes exhibit fractal shaped bifurcations and they sometimes drift eastward. Conjugate allsky imager observations of plumes from Puerto Rico and Argentina (**Martinis and Mendillo, 2007**), and plumes (**Otsuka et al., 2004; Ogawa et al., 2005**) and MSTIDs (**Shiokawa et al., 2005**) from Japan and Australia revealed the strong conjugate electrodynamic coupling between the mid-latitudes of the northern and southern hemispheres through the geomagnetic field lines. Since these plume-shaped depletions appear from the south in the allsky images during geomagnetic storms, they could be associated with the poleward surge of high-altitude equatorial spread-F bubbles at the magnetic equator. Studies done with the GUVI imager instrument on the TIMED satellite clearly show that the equatorial ESF plumes can reach mid-latitudes following magnetic flux tubes (**Kelley et al., 2003c; Kil et al., 2004**).

In addition to plasma depletions, the mid-latitude F-region is also active with plasma enhancement structures. The most well known one is the Midnight Temperature Maximum – Brightness Wave (MTM-BW or known as “midnight collapse” at AO) (**Nelson and Cogger, 1971)**. The midnight collapse (or brightness wave) is caused by lowering of the F-region due to reversal of the meridional winds from equatorward to poleward due to the MTM pressure bulge, which is thought to be formed by a nonlinear interaction between the higher tidal mode components of the thermospheric winds and the diurnal cycle of F-region ionization (**Herrero and Meriwether, 1980; Colerico et al., 1996**). During the midnight collapse, the allsky images appear brighter due to an increased recombination rate (**Figure 1.6c**). Other enhancement structures have also been observed rarely at mid-latitudes, including fractal shaped plasma enhancement plumes (**Figure 1.6d**) which look similar to depletion plumes and also occur when Kp is high. Occasionally, a depletion plume turns into an enhancement plume (**Figure 1.6e**). It is thought to be caused by the depleted flux tubes suddenly being filled by plasma due to an unknown triggering mechanism. None of these mid-latitude phenomena (except MTMs) have been studied thoroughly. More detailed information about various mid-latitude events observed by PSASI is given in **Seker (2006).**

1.6. Medium-Scale Traveling Ionospheric Disturbances (MSTIDs)

It is now well known that one of most common mid-latitude night-time F-region phenomenon observed with allsky imagers is the MSTID (also called plasma depletion bands, ionospheric slabs, mid-latitude spread-F, plasma waves, and plasma bubbles). Although we think that none of the aforementioned names (including "MSTID") are specific enough to be a good nomenclature, we use the term "MSTID" as it has been widely used in the literature for a long time. Perhaps a better name is "Coherent Omnipresent Fluctuations in the Ionosphere (COFIs)" which was used by **Livneh et al. (2009)** to emphasize the coherence, periodicity, and prevalence of these bands apparent throughout the day and over multiple days.

MSTIDs have been frequently observed using allsky imagers at various mid-latitude locations such as Puerto Rico (**Mendillo et al., 1997; Garcia et al., 2000; Seker et al., 2008**), Argentina (**Martinis et al., 2006**), and simultaneously at conjugate points in Japan and Australia (**Otsuka et al., 2004; Shiokawa et al., 2005**). The occurrence rate of mid-latitude MSTIDs is very high. According to **Shiokawa et al. (2005)**, MSTIDs were present in allsky images for almost all clear-sky nights. **Tsugawa et al. (2007a)** observed MSTIDs 85% of the time using total electron content (TEC) maps and allsky imagers. Similarly, the analysis of a three year dataset from our allsky imager at AO revealed that the MSTIDs were present ~75% (123 out of 167 nights) of the time for clear-sky (none or very few clouds), moon-down (more than 100 images per night), low Kp (< 4) conditions. According to **Shiokawa et al. (2003a)** the occurrence rate of MSTIDs over Japan is higher during low solar activity and has a major peak in summer and a minor peak in late winter, whereas the MSTIDs over Arecibo mostly occur during the winter (**Garcia et al., 2000**).

Based on allsky imager observations (e.g., **Figure 1.6a**), a typical MSTID event is characterized as a series of medium-scale, quasi-periodic, F-region plasma depletion bands that are aligned northwest to southeast and that propagate southwestward at night in the northern hemisphere. These waves are usually observed in the F-region when geomagnetic activity is low and have a typical horizontal wavelength of 100-300 km and a period of ~1 hr. The MSTID bands appear as dark spikes (due to uplift or depletion of the bottom-side of the nighttime F-region) in plots of electron density profiles obtained by incoherent scatter radar (ISR) (e.g., **Figure 2.1b**). These MSTID features appear to be more intense during the "midnight collapse" period (**Herrero and Meriwether, 1980; Colerico et al., 1996**), especially when the geomagnetic activity is low. **Livneh et al. (2007)** showed, using high-pass filtered ISR results that these waves are a manifestation of a quasi-periodic (~1 hr period) wave process that extends through the whole ionosphere (from 200 km up to 600 km) (**Figure 1.7**). **Tsugawa et al. (2007b)** showed, using TEC maps, that the MSTIDs also exist during the day and propagate southwestward during the night and southeastward during the day over the continental United States (**Figure 1.8**).

By analyzing high-pass filtered ISR results from several radars at various latitudes, **Livneh et al. (2009)** found that the vertical wavelength of MSTIDs increases not only with altitude but also with latitude.

This dependence on latitude can be explained if the MSTIDs are actually field-aligned since the geomagnetic dip angle becomes larger at high latitudes. On the other hand, the dependence on altitude is likely due to the decoupling of neutrals and ions above a certain altitude causing the plasma to more closely follow the vertically tilted field lines at higher altitudes. The ISR and imager observations of MSTIDs from AO, along with specific properties inferred from these observations, are given in detail in **Section 2.1.**

Although the origins of MSTIDs are not yet clear, several possible explanations have been proposed: Perkins instability, atmospheric gravity waves, and magnetospheric processes (**Perkins, 1973; Garcia et al., 2000; Kelley and Makela, 2001; Shiokawa et al., 2003b; Zhou and Mathews, 2006; Livneh et al., 2007, 2009**), all of which can explain only some of the observed properties of MSTIDs. The nighttime F-region electrodynamics, and thus the MSTIDs seen in the allsky images, are presumed to be described by the so called Perkins Instability equations (nighttime F-region appropriate electron/ion momentum and continuity equations along with divergence of current density set to zero) (**Perkins, 1973; Garcia et al., 2000; Kelley and Makela, 2001; Zhou and Mathews, 2006**).

As **Figure 1.9** illustrates, results from numerical models based on the Perkins Instability agree with the observations in terms of orientation and propagation direction (**Zhou et al., 2006**). However, the Perkins instability works only during the night and requires a seeding mechanism. On the other hand, atmospheric gravity waves can provide the observed periodicity and necessary seeding but not the alignment and propagation direction of the MSTID bands, which are best explained by the Perkins instability. Although it is not trivial to explain how tropospheric, or even mesospheric, gravity waves can reach F-region altitudes without dissipating, it seems that both gravity waves and the Perkins Instability play a role in the generation and electrodynamics of the MSTID bands in the F-region. Others (e.g., **Shiokawa et al., 2003a; Seker et al., 2008**) proposed a combination of these theories (e.g., gravity waves acting as the seeding mechanism for the Perkins Instability) as the source of the MSTIDs.

Recent studies using satellite data suggest that there might be a connection between ionospheric waves, the magnetosphere, and the solar wind via coupling among these regions. Recent studies (e.g., **Kepko and Spence, 2003; Kelley et al., 2003d; Livneh et al., 2009**) showed that there are waves in the magnetosphere and possibly in the solar wind with periods similar to that of MSTIDs (i.e., ~1 hr). This magnetospheric origin theory requires either direct coupling between the ionosphere and magnetosphere such as the modulation of the whole magnetosphere-ionosphere system or the penetration of electric fields across geomagnetic field lines to low L-shells, or indirect coupling by the propagation (without dissipating) of gravity waves generated within auroral regions (via joule heating and the Lorentz force) to mid/low-latitudes as Earth-reflected waves (**Samson et al., 1990**).

None of these theories have been proven to date. More elaborate research using a larger set of instruments is required in order to better understand this F-region phenomenon and its seeding mechanism. The study proposed here aims to explore these issues and provide useful insights. The electrodynamics of the MSTIDs is discussed in detail in **Section 4.2** taking into account the new results obtained from this study.

1.7. MSTID Observations Using Various Instruments and Techniques

Allsky imagers, which provide local (mesoscale), horizontal, two-dimensional information with temporally and spatially-high resolution (~1 min and ~1 km) are perhaps the most suitable instruments for observing MSTIDs. Recent papers such as **Otsuka et al. (2004), Shiokawa et al. (2005), Vlasov et al. (2005), Martinis et al. (2006), Tsugawa et al. (2007a),** and **Seker et al. (2008)** used allsky imagers to observe MSTIDs. The MSTIDs have also been observed recently using single-point instruments such as ISR (**Nicolls et al., 2004; Vlasov et al., 2005; Livneh et al., 2007, 2008; Seker et al., 2007, 2008**), and GPS satellites (**Vlasov et al., 2005; Martinis et al., 2006; Tsugawa et al., 2007a; Seker et al., 2008**). One way to have a larger coverage is to create TEC maps using multiple GPS receivers (**Nicolls et al., 2004; Tsugawa et al., 2007a, 2007b**). Another recent technique combines the advantages of satellites and imagers (by putting imagers on satellites), providing global coverage of ionospheric irregularities such as ESF plumes and MSTIDs (**Kil et al., 2004; Ogawa et al., 2005**) (**Figure 1.10**). A basic but effective technique is to map the ground-based allsky image onto the wide maps created from the GPS-TEC data (**Tsugawa et al., 2007a**) or onto the global images obtained from imagers onboard satellites (**Ogawa et al., 2005**). At the moment there is consensus within the MSTID community on the necessity of using multiple instruments together for understanding the MSTID phenomenon. For example, recent papers explored MSTIDs using ISR and allsky imager (**Vlasov et al., 2005; Livneh et al., 2007**)**,** allsky imager and TEC (**Martinis et al., 2006; Tsugawa et al., 2007a**), ISR and TEC (**Nicolls et al., 2004**), and all three instruments (**Seker et al., 2008**).

Figure 1.11 shows the results from an MSTID event on 17 June 2004 obtained using a technique (which was initially created by **J. J. Makela** to analyze the equatorial spread-F plumes) that enables the study of MSTIDs using a combination of imager and GPS-TEC datasets (**Makela et al., 2000, 2001a; Seker et al., 2008**). The positions of the satellite-to-receiver ray path at 350 km are shown in these allsky images. By following the track of the GPS satellites (mapped to the airglow altitude) on the allsky images and plotting the TEC, it is possible to reveal whether the MSTID bands are caused by depletions or uplifts. Azimuth-scanning ISR observations on the same day were also made (**Figure 3.1**) and, along with the allsky images, make up the major dataset of this dissertation. **Figure 1.11** clearly reveals that the MSTID dark bands are associated with a significant drop in TEC. This means MSTIDs are not only uplifts (as ISR results suggest), but also depletions. In fact, when these ionospheric slabs rise, depletions have to occur also since the recombination rate is lower (less intense airglow) at higher altitudes due lower neutral density (**Seker et al., 2008**).

Thome (1964) was the first study to use the Arecibo ISR in the azimuth-scanning mode to reveal the basic properties of MSTID bands such as their period, propagation speed and direction. **Behnke (1979)** improved the azimuth-scanning technique by comparing the variation of the height of the peak electron density (h_{max}) with the azimuth angle variation in time allowing him to track the location of the radar beam at F-peak heights. Other studies used the azimuth-scanning ISR to obtain E-field and charge drift information (**Aponte et al., 2000; Kelley et al., 2003b**). In order to show the directionality of the azimuth-scanning ISR data, it is possible to create the azimuthal maps as used in **Aponte et al. (2000)**. An azimuthal map is a polar plot displaying each column of the ISR data with respect to angle; so each azimuthal map shows 16 min. of data (a full circle). However, without the allsky images complementing the azimuth-scanning ISR data, the information derived from the narrow ISR beam will always be limited and aliased unless the ionospheric structures are stationary or slow moving. Observations from radar and allsky imager (along with other instruments) were shown together in several recent studies: **Kelley et al. (2000a)** (imager, ISR), **Pi et al. (2000)** (imager, ISR, FPI), **Kelley et al. (2002)** (imager, ISR, GPS), **Otsuka et al. (2003)** (imager, MU radar, FPI). However, these studies were typically limited to comparing the radar "image" and the allsky image by looking at them simultaneously, rather than using the two jointly to infer additional information about the structures being studied. Here, we employ a different technique to visualize the directionality of ISR data which also allows us to compare the imager and ISR results. This new technique, which involves fusing the two datasets by tracking the azimuth-scanning ISR beam on the allsky images, is introduced in **Section 2.2**. This technique makes it possible to construct an empirical 3D model of the MSTID structures to further enable interpretation of relevant datasets. Such a model is presented in **Section 2.3**.

1.8. Research Questions

The study presented here aims to answer two main questions regarding MSTIDs:

1) What do the various features seen in the azimuth-scanning ISR observations represent?

As described earlier, the AO ISR can be used in two modes: fixed-zenith and azimuth-scanning (which can provide E-field and charge drift information). The fixed-zenith results are much easier to interpret than the azimuth-scanning results since when the radar beam is in rapid motion relative to the propagating ionospheric structures with horizontal gradients, the resultant RTI plot exhibits vertical striations with sharp edges. In other words, the information representing a certain ionospheric structure is scattered in time in the RTI plot, and it is nearly impossible to make any direct inference regarding medium-scale ionospheric structures from such a plot.

2) What is the three dimensional shape of the MSTID structures? Are MSTID bands field-aligned?

Although observations of MSTIDs using various instruments have revealed many of their properties, the 3D shape of the MSTID bands has so far remained a mystery. For example, radars have been used to obtain 1D information regarding the vertical structure of MSTIDs whereas imagers have provided the 2D horizontal structure. However, since the MSTID structures are in motion and the radar data are in one dimension, the limited information obtained from the radar is aliased in space/time. On the other hand, although the information obtained from the allsky imager is two dimensional, the vertical information is lost since the imager data are a result of the integration of airglow emissions from a large range of altitudes that cover the whole nighttime F-region. Furthermore, although various theories assume or claim that the MSTID bands are (geomagnetically) field-aligned, it has not yet been shown whether that is the case due to the lack of information on the 3D shape of MSTIDs.

(a) Neutral atmosphere (b) Ionosphere

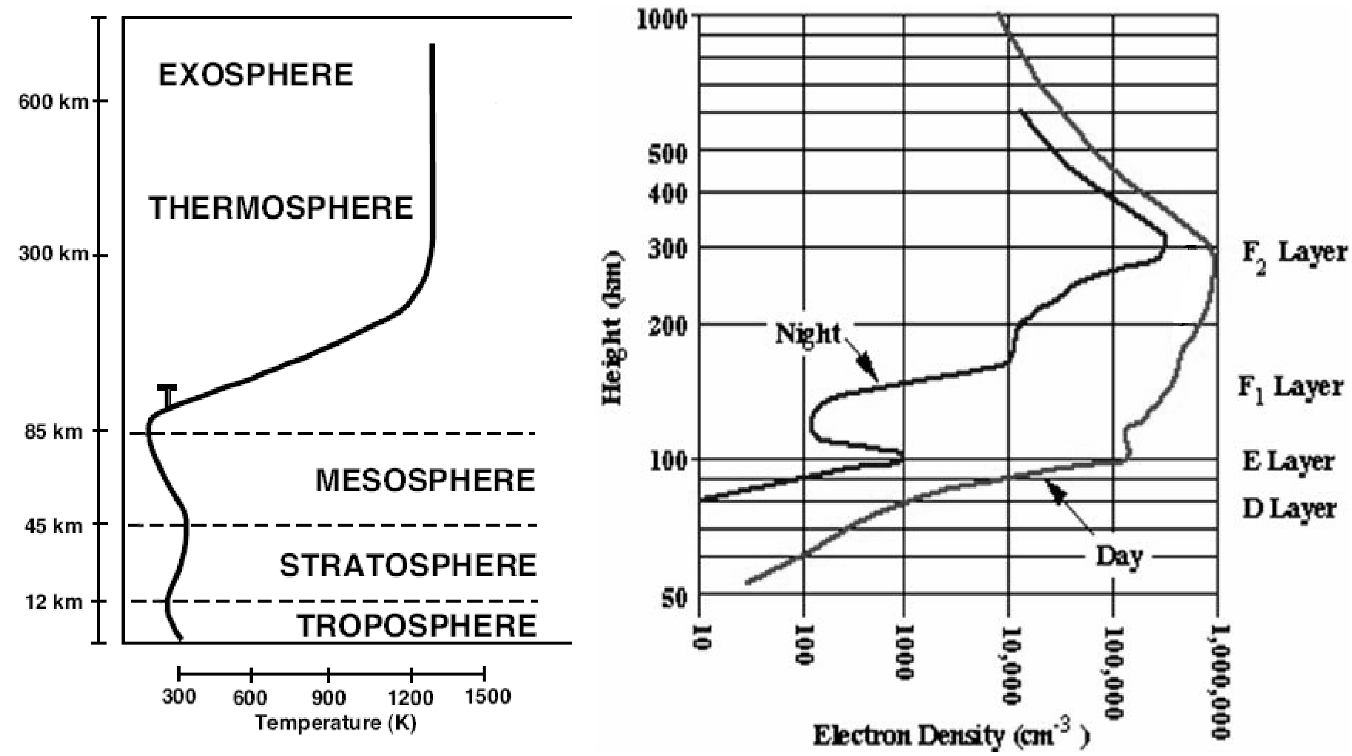

Figure 1.1. Temperature and electron density structuring of atmospheric layers. (source: http://encyclopedia.quickseek.com)

(a)

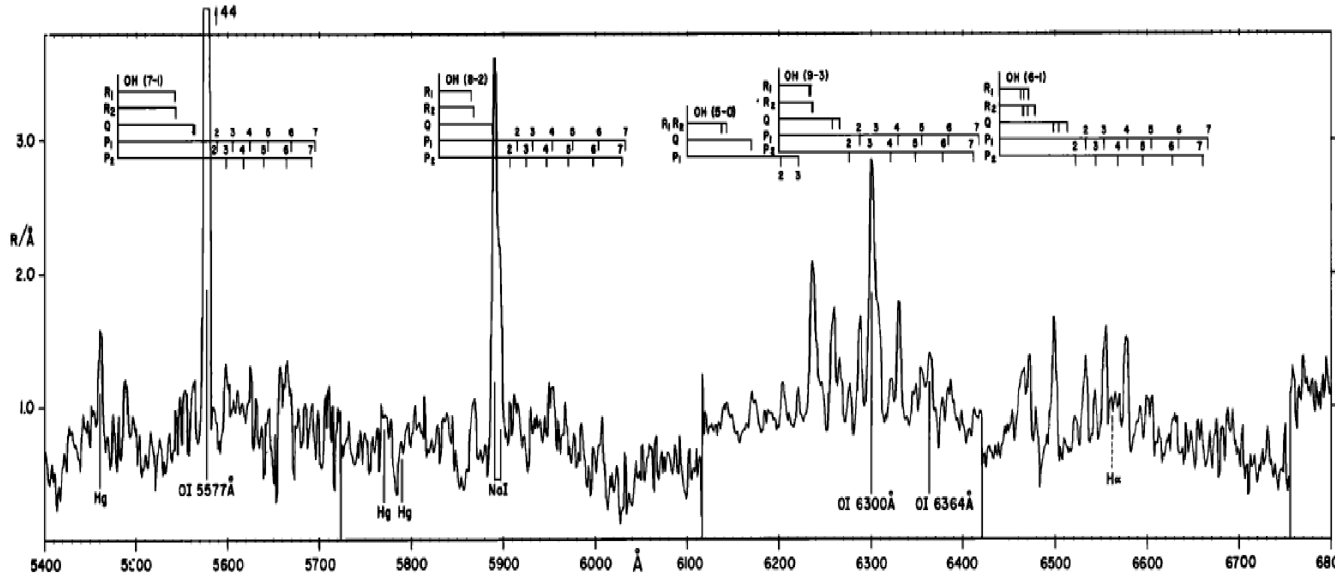

(b)

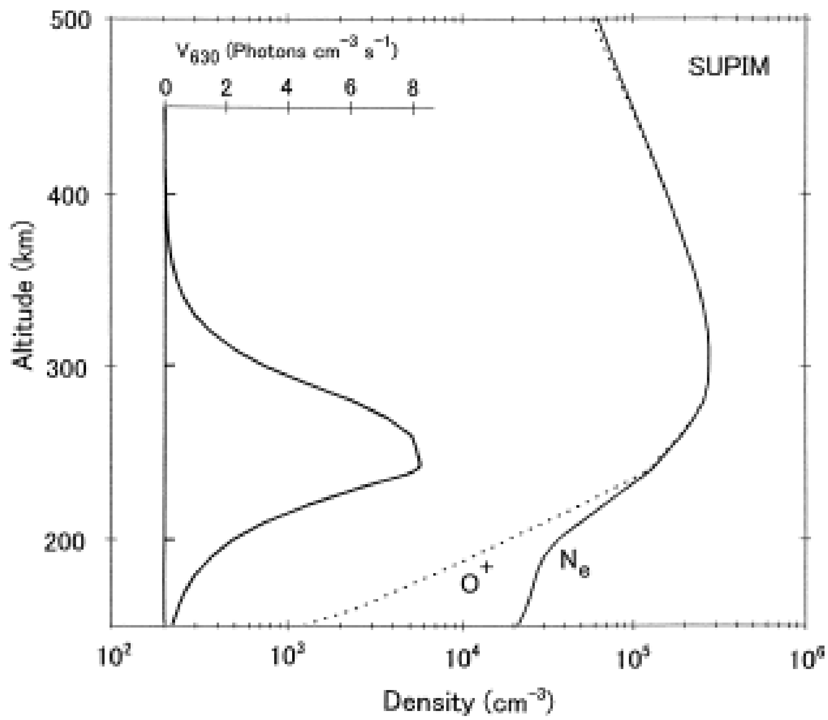

Figure 1.2. (a) Optical spectra of airglow. (**Broadfoot and Kendall, 1968**) (b) N_e, [O^+], and 630 nm volume emission rate profiles at 1400 UT on 22 May 1998 over Japan. The profiles are derived from The Scheffield University Plasmasphere Ionosphere Model (SUPIM). (**Ogawa et al., 2002**)

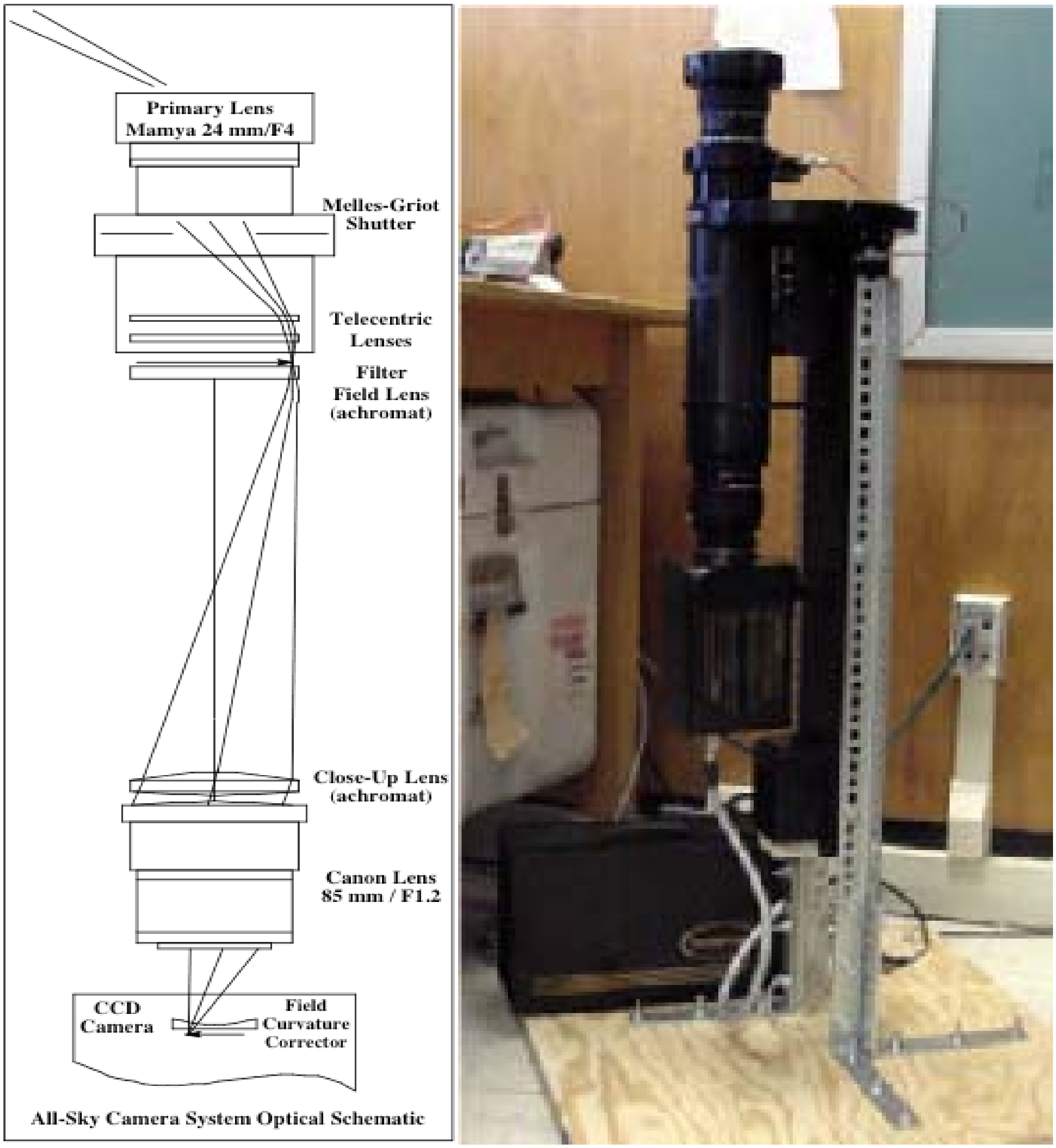

Figure 1.3. The schematic of the optical system and a photo of PSASI. (**Seker, 2006**)

(a) (b)

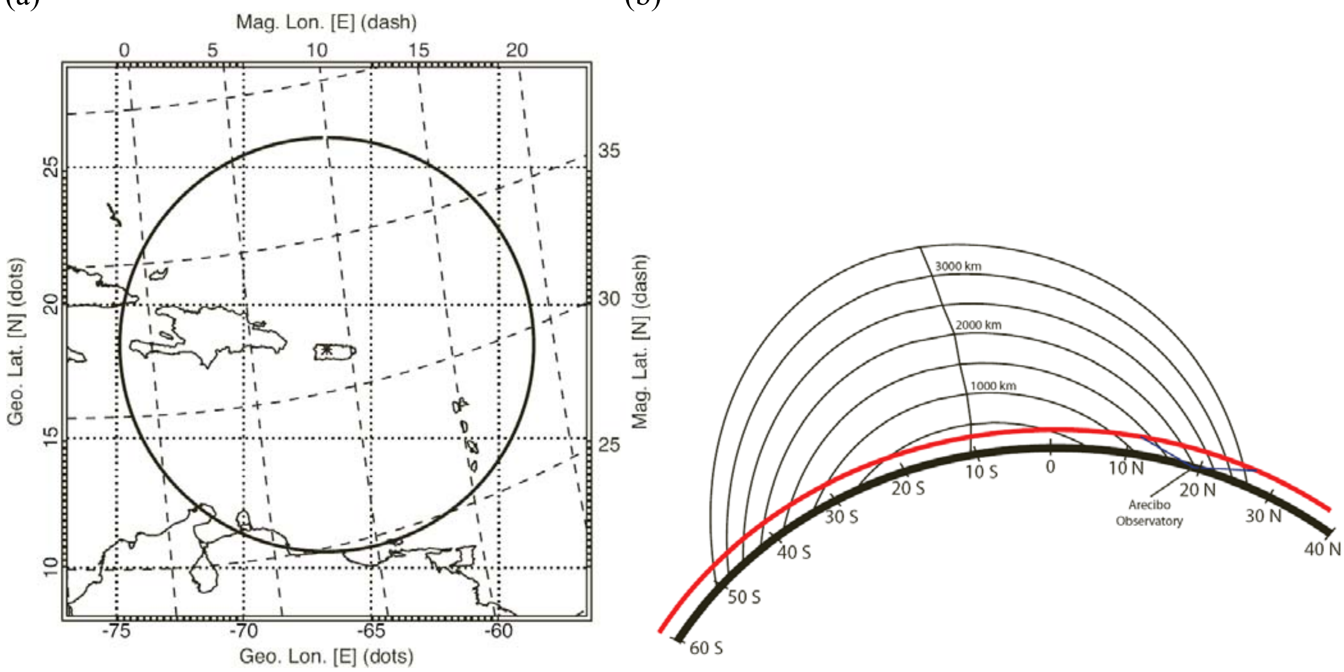

Figure 1.4. (a) Geographic coordinate (latitude vs. longitude) map centered on AO showing coverage of the imager with a field of view of 150º assuming an emission height of 300 km. (b) Geomagnetic field line distribution (latitude vs. altitude) in the magnetic meridional plane of AO mapping the 630 nm airglow depletions at 300 km seen in the imager to an apex height of 1500-3500 km. Altitude Adjusted Corrected Geomagnetic Coordinates (AACGM) are used. (**Seker, 2006; Seker et al., 2008**)

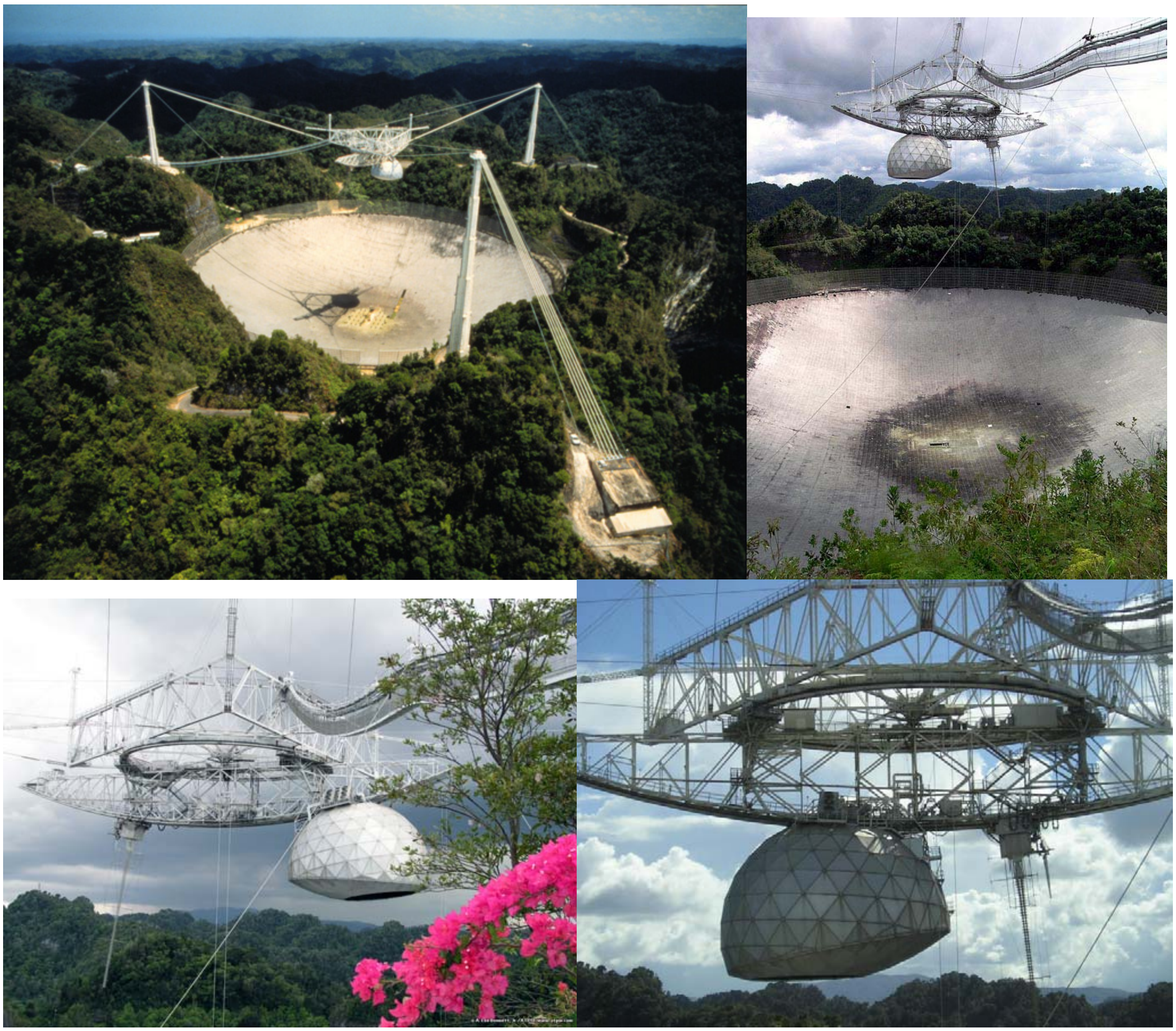

Figure 1.5. Photo of the Arecibo Telescope. The close-up photos of the Gregorian and linefeed receivers are also shown.

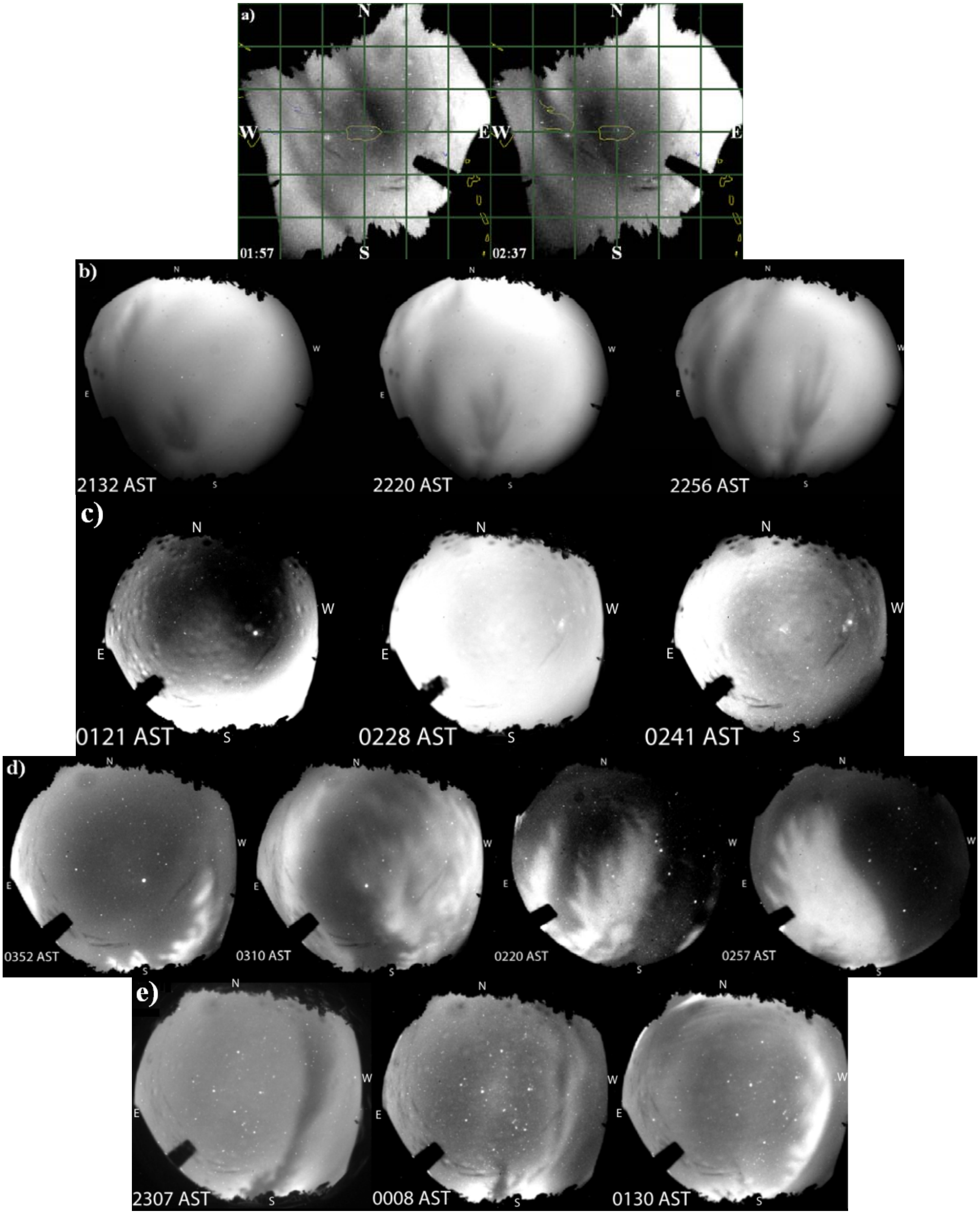

Figure 1.6. Allsky images taken by PSASI at AO showing (a) MSTID bands (from 23 March 2004), (b) a spread-F plume event (from 29 May 2003), (c) a brightness wave (from March 19, 2004) which appears from the southwest, covers the whole image, and then leaves the field of view from the northeast, (d) enhancement plumes (from 27 January 2004, 22 January 2004, 17 January 2005, and 18 December 2004), (e) showing a depletion plume becoming an enhanced plume (from 26 December 2003). (**Seker, 2006**)

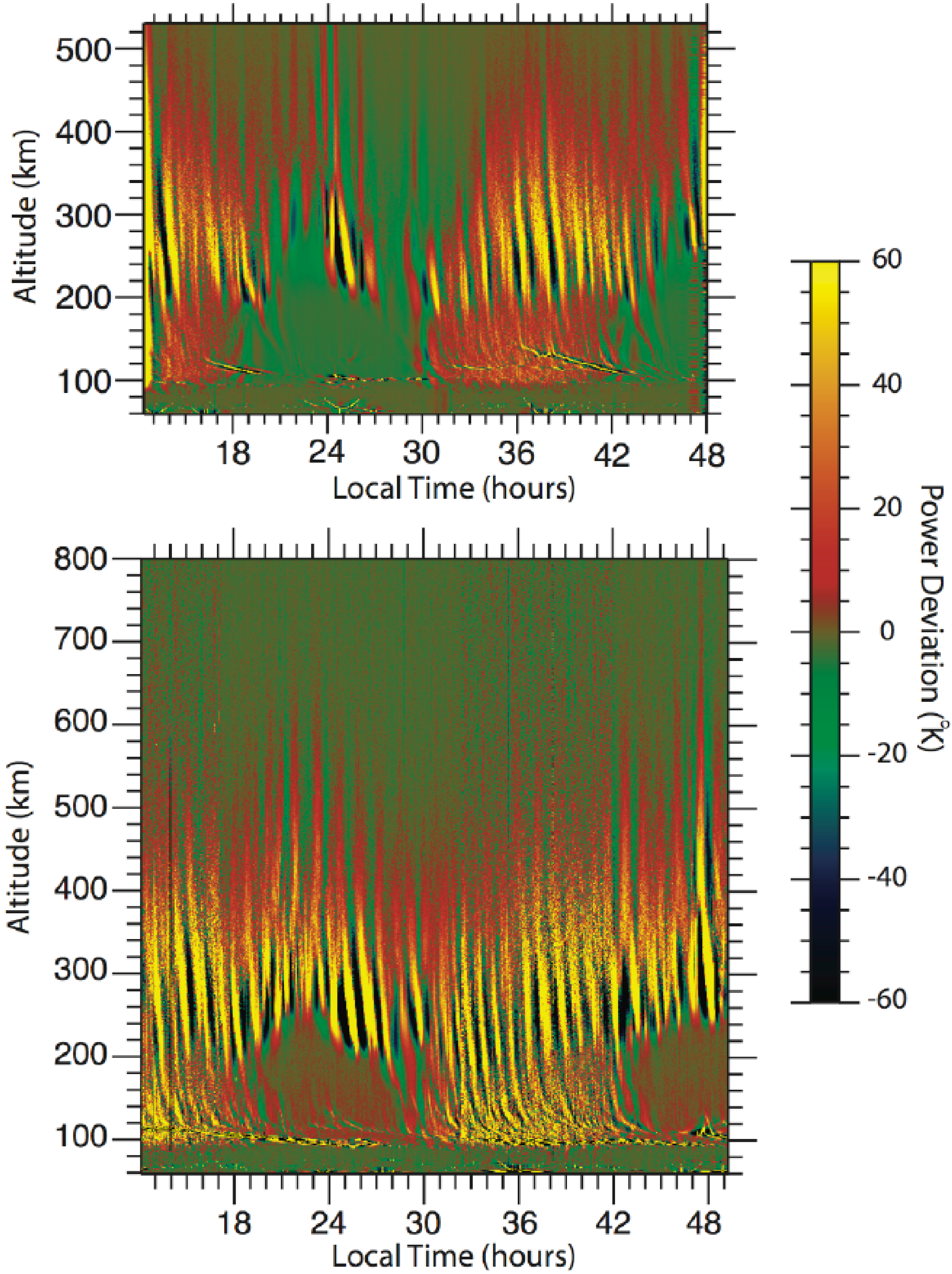

Figure 1.7. High-pass filtered fixed-zenith ISR results from AO on 22-23 March 2004 and 5-6 June 2005 revealing the quasi-periodic MSTID bands. (**Livneh et al., 2007**)

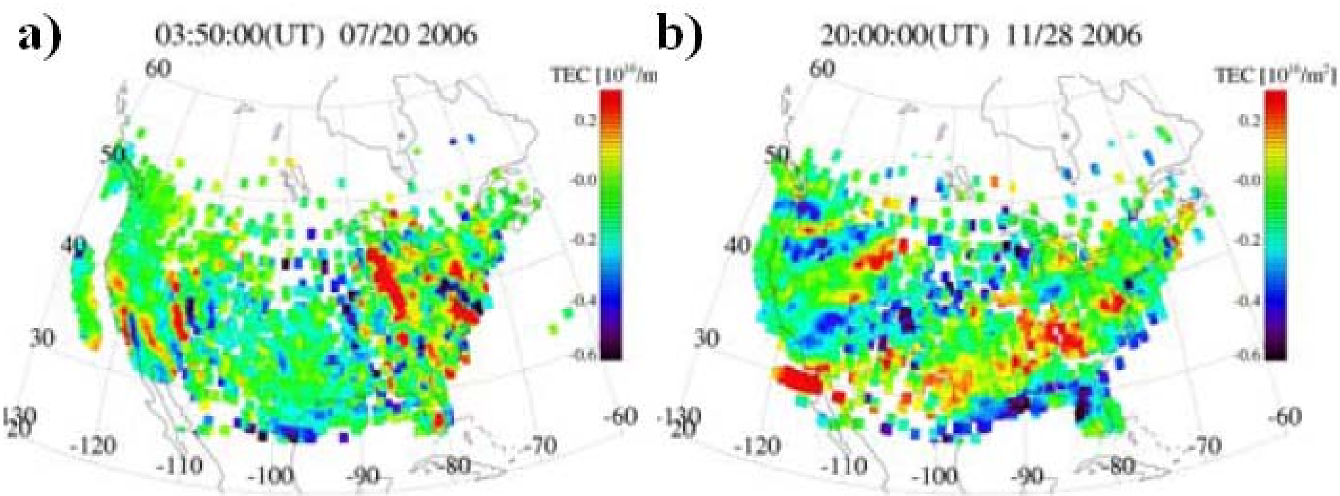

Figure 1.8. 2D TEC maps over the continental United States showing the MSTID bands for (a) nighttime and (b) daytime. (**Tsugawa et al., 2007b**)

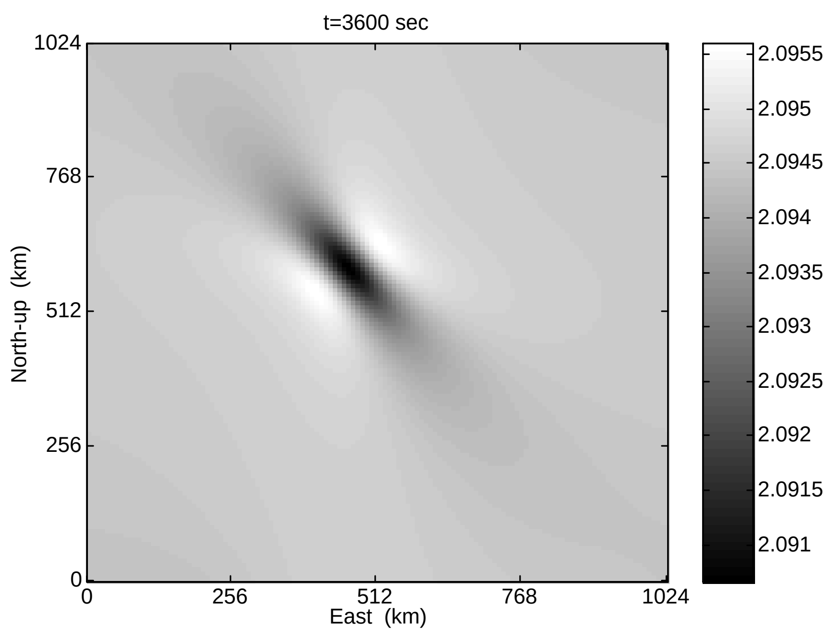

Figure 1.9. The integrated Pedersen conductivity development in a real-time electric field numerical simulation of the Perkins Instability. The instability structure grows along northwest-southeast direction and moves toward the southwest. (**Zhout et al., 2006**)

(a)

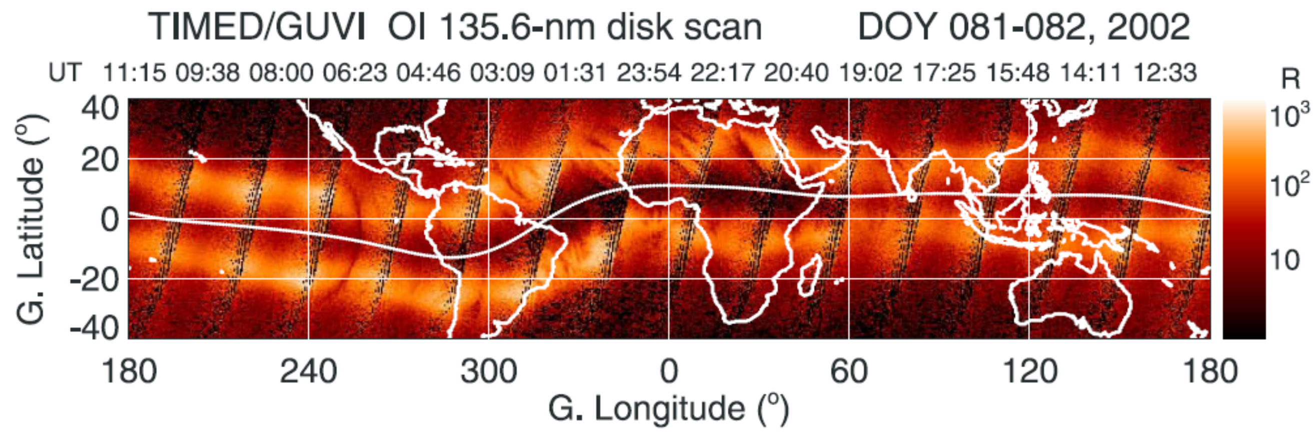

(b)

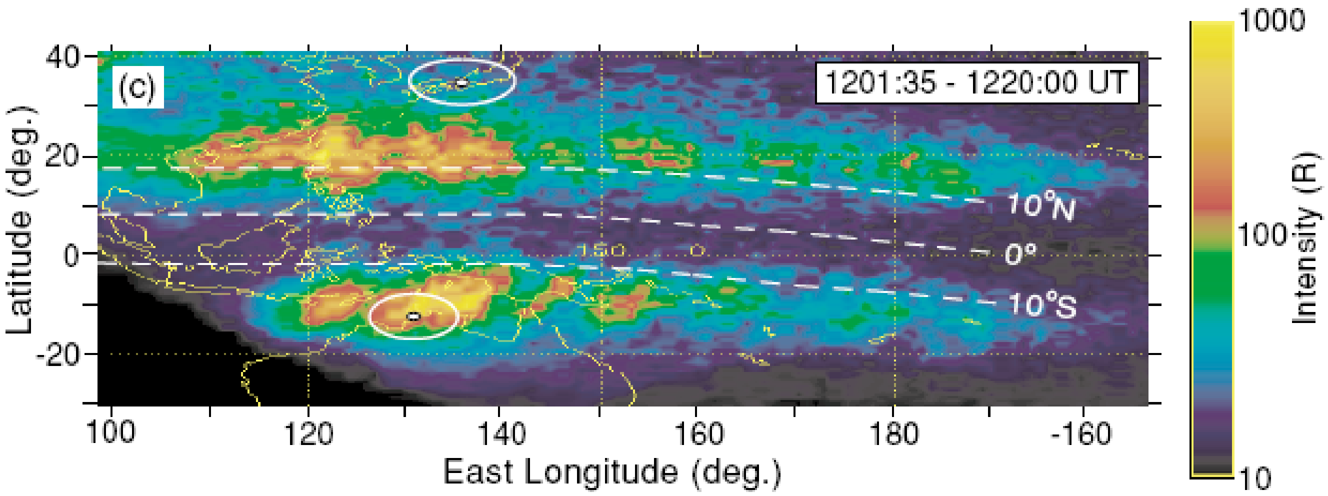

Figure 1.10. (a) Composite disk scan (136.5 nm) image from the GUVI instrument on the TIMED satellite showing ESF plumes. (**Kil et al., 2004**) (b) A similar (136.5 nm) image from the IMAGE satellite. The dots and ovals show the location and field-of-view of the two allsky imagers in Japan and Australia. (**Ogawa et al., 2005**)

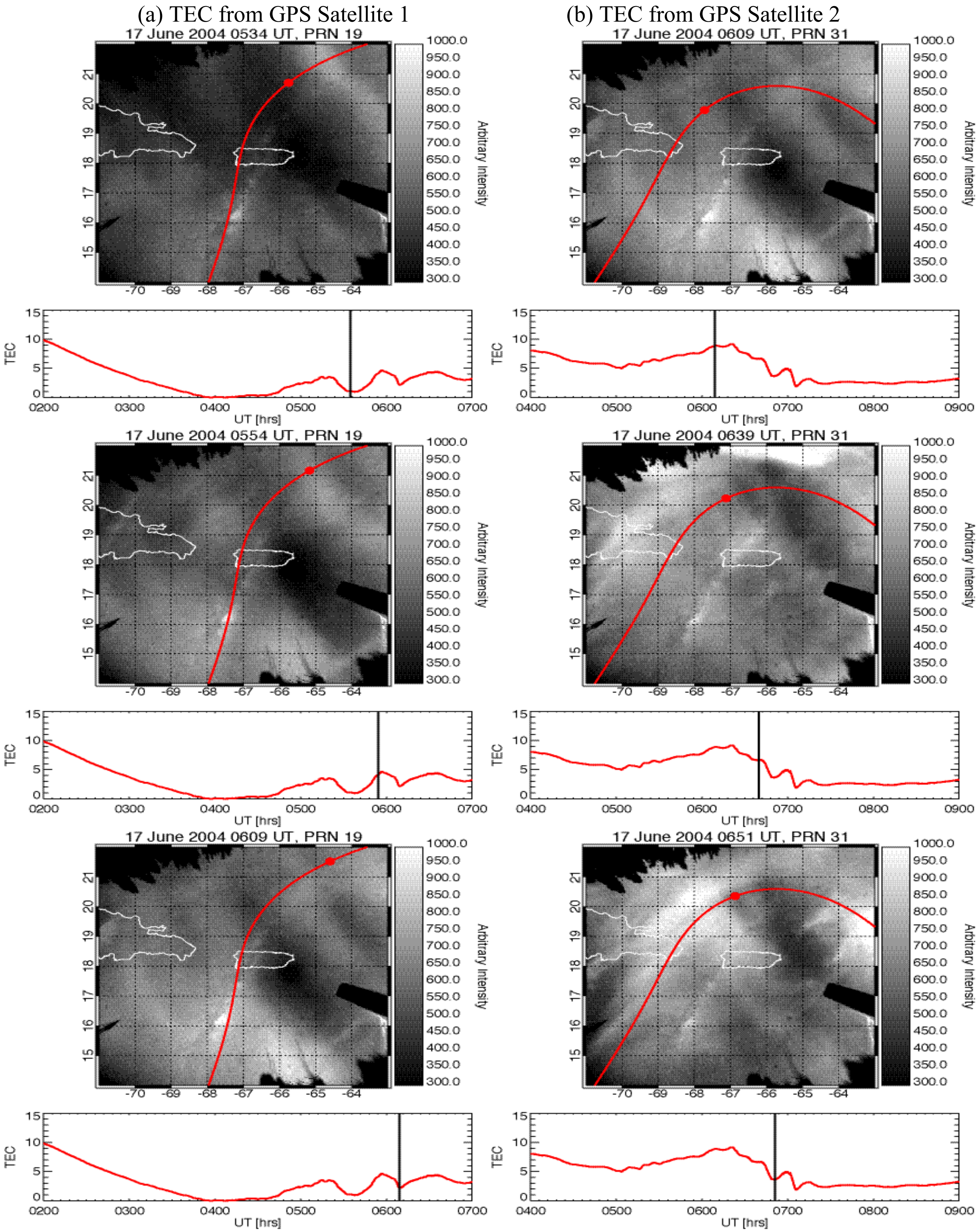

Figure 1.11. TEC data on 17 June 2004 from two different GPS satellites, the tracks of which are shown in the allsky images. The vertical lines on the TEC plot for each frame denotes the time at which the allsky image data was collected. (source: **J. J. Makela**) (**Seker et al., 2008**)

2. METHODOLOGY

In order to answer the aforementioned research questions, a three step approach has been employed. The first step involves a simple analysis of the data from the allsky imager and (vertical-beam) ISR observations which, in the literature, has usually been the only step in the study of MSTIDs using ISR and/or allsky imager. This was already done in Section 3.2.3 of the Ph.D. candidate's M.S. thesis (**Seker, 2006**). Nevertheless, the results (**Figures 2.1-2.4**) will be repeated here for completeness. Next, these two datasets are combined or fused using a new technique which will be explained in detail later in this chapter. This fusion technique enables extraction of more information which would not be possible if each instrument was used by itself. Finally, an empirical 3D model based on the observational findings is used both to confirm the results and to reveal more information on MSTIDs and how they appear in ISR and imager results.

2.1. Imager and Radar Observations

It should be mentioned that the Penn State Allsky Imager (PSASI) and Incoherent Scatter Radar (ISR) measure different parameters in the ionosphere. An imager can measure the airglow at a specific wavelength by counting the photons emitted during a specific time interval as a result of the recombination reactions in the ionosphere. The airglow intensity (e.g., at 630 nm), in turn, depends on certain neutral and ion concentrations. If the ion involved in the reaction is a dominant ion (e.g., O^+) of the ionospheric plasma, then its concentration gives an estimate of the plasma density. Consequently, allsky images can provide plasma density information. On the other hand, the ISR measures the intensity of the back-scatter echo which is proportional to the number of electrons in the illuminated volume. From this information, the electron concentration (e.g., plasma density) can be directly calculated. Each allsky image is a result of the time-integration of photon counts which depends on the reaction rate involved (e.g., ~1 min for 630 nm). However, as PSASI uses several filters in series, the time interval between two consecutive images taken with the same filter is larger (~4 min). The spatial resolution depends on the emission altitude and the number of pixels in the CCD (~1 km at 630 nm altitudes for PSASI). The AO ISR has much better temporal and spatial resolutions compared to PSASI (10 msec and 150 m); however, an imager can provide (horizontal) information in 2D, whereas a radar can provide (vertical) information only along a single look angle. In other words, both instruments have advantages and disadvantages.

Figures 2.1a and **2.1b** show a typical observation of MSTID bands from 22-23 March 2004 by the Penn State Allsky Imager (PSASI) and Incoherent Scatter Radar (ISR) at Arecibo Observatory (AO). The same allsky images were already shown in **Figure 1.6a**, and are repeated here for convenience. In addition, high-pass filtered version of the ISR data in **Figure 2.1b** was shown in **Figure 1.7**. It is possible to extract much information on the properties of MSTIDs from these observations alone. The ISR and imager intensity variations for MSTIDs are of order 5-15%.

The MSTIDs appear as a series of dark, bubble-shaped depletion bands in the allsky images. As can be seen from the allsky images in **Figure 2.1a**, the bands appear larger in the south compared to the north and are aligned along geographic northwest-southeast (~30° off north-south) with a typical horizontal wavelength of ~150 km. In the figure there are four consecutive bands; the first one from the left is nearly outside of the image (farthest southwest) and the third one does not reach south to AO latitudes. The bands appear from the northeast and propagate southwestward with a typical speed of ~150 km/hr (~40 m/s) causing a spike train in the ISR plot with a ~1 hour period.

Figure 2.1b shows the corresponding fixed-beam ISR RTI plot from AO. The MSTIDs appear as a series of dark spikes in the ISR plot. These dark features seen in the figure form a saw tooth pattern (in the fixed-zenith mode), i.e., the peaks are very sharp and the leading (southwestward) edge appears to be much steeper than the trailing (northeastward) edge. As expected, there is a gap in the ISR plot between the second and fourth bands since the third band does not pass over AO, as can be seen in the allsky images. Further inspection reveals that these three dark spikes seen in the ISR data from 23-27 LT correspond to the imager MSTID bands, and they are actually caused by vertical uplift of the whole night-time F-layer, meaning both the top-side and bottom-side of the F-layer are affected. This uplift causes the appearance of an enhanced spike above each dark spike in the vertical ISR data.

From the ISR data the magnitude of this vertical uplift appears to be ~100 km from the altitude of the bottom-side of the F-layer, which varies between 200 km and 300 km as caused both by diurnal variations and the MTM-BW (or "midnight collapse" at AO) (**Nelson and Cogger, 1971**). In other words, depending on the altitude of the F-layer, the imager dark depletion bands extend from 200-300 km up to 300-400 km and the enhancement bands extend from 400-500 km up to 500-600 km assuming that the F-layer is ~200 km thick.

Another interesting point that surfaced from these observations is the differences in intensity variations of the data recorded by each instrument. The ISR data varies ~10-15% if averaged over whole ionospheric heights, and ~15-30% if averaged only between 210 km and 330 km. The allsky imager data (around 250 km) varies ~10-15%. On the other hand, the GPS-TEC (shown in **Figure 1.11**) varies by a large percentage of ~50-70%. These differences may yet yield additional insight into the processes involved. However, it is necessary to note that each of these instruments is sensitive to different aspects of the ionosphere and so the possible significance must be regarded with caution.

Table 2.1 summarizes the properties of the MSTID bands inferred from the allsky imager and ISR observations. Similar parameters (wavelength: 100–300 km, velocity: 50–100 m/s, period: 0.5–1.5 h, amplitude: 5–15%) were reported by other studies, such as **Shiokawa et al. (2003a)** who analyzed two years of allsky imager data. More discussion on the interpretation of these observed values is given in **Chapter 4**.

2.2. The Fusion Technique

2.2.1. ISR Fixed-Zenith Mode

Although the data from the radar in the fixed-zenith (e.g., vertical beam) mode are unaliased, they give no horizontal information. In this mode it is straightforward to compare the radar and imager results by simply matching (the time of) each allsky image with the corresponding vertical ISR profiles. This was already done in **Seker (2006)**, but the results will be briefly repeated here for completeness and in order to make it easier to understand the much more complex azimuth-scanning method which will be explained in the next section.

In order to better show the depletion spikes in **Figure 2.1b**, an enlarged version of the rectangular area is shown in **Figure 2.2**. **Figure 2.3** shows a series of allsky images taken with the 630 nm filter of PSASI. The images are mapped to geographical coordinates. Since the radar beam was vertical, the center of each image, which corresponds to the location of the AO ISR, also corresponds to the location of the radar beam. The frame numbers correspond to the numbers shown in the ISR result in **Figure 2.2**. The dashed lines and numbers shown in **Figure 2.2** correspond to the (integration) time of all available allsky images and the allsky frames shown in **Figure 2.3**, respectively.

The allsky frames illustrate various horizontal properties of the MSTIDs, such as their oblong bubble shape, the northwest-southeast alignment, and their southwestward propagation. The ISR result reveal the vertical extents of the MSTID depletion bands embedded in the midnight collapse. However, each instrument has limitations and cannot fully characterize these F-region structures. The horizontal information obtained from the imager and vertical information obtained from the radar complement each other revealing more information on the structure of the MSTID bands. To verify that both instruments are seeing the same features, it is sufficient to compare Frames 2, 4, and 7 of **Figure 2.3** (when the AO ISR beam is inside the depletion band) with the corresponding vertical profiles shown in **Figure 2.2**, which clearly show three separate vertical spikes. In addition, Frames 3, 4, and 5 track the **Figure 2.2** radar results almost exactly with the progression from F-region low (bright band overhead), high (dark band overhead), and lowering (dark band passing). In the ISR data corresponding to Frames 3 and 6 in the imager data, we see that the ionosphere base is lower due to the midnight collapse, resulting in higher recombination. This leads to a brighter emission, as seen in the allsky imager data. These comparisons show that the allsky imager and ISR results agree very well with each other.

Figure 2.4 shows the airglow intensity at the location of the ISR beam (i.e., the zenith is at the center of flattened allsky images) and the corresponding ISR signal temperatures averaged through the 630 nm airglow layer (**Seker, 2006**). Depletion bands, clouds, and midnight collapse are also indicated. The similarity between these two plots once again confirms that the ISR and imager results agree very well with each other. The intensity of the airglow across (from southwest to northeast) the thick depletion band at 24.5 LT (corresponding to Frame 4 in **Figure 2.3**) is given in **Figure 2.5a**. On the other hand, **Figure 2.5b** shows the ISR electron concentration averaged from 300 km to 330 km across the two MSTID bands at 24 LT and 24.6 LT (corresponding to Frames 2 and 4 in **Figure 2.3**). Also shown in the same figure are the heights of the depletions or uplifts calculated using a constant threshold for each ISR vertical profile. It is clear from all three results that the intensity transition at the southwestern edge of an MSTID band is sharper than the transition at its northeastern edge. This suggests that, during the formation of MSTID bands, somehow the nighttime F-layer suddenly rises and then gradually falls back forming the saw-tooth shape of MSTID bands.

2.2.2. ISR Azimuth-Scanning Mode

In this section, a technique that makes it possible to combine the azimuth-scanning ISR and allsky imager data is introduced. The results of employing this technique not only reveal important clues on the 3D structure of MSTID bands (which in turn enables us to construct an empirical 3D model of them), but also allows us to better understand the complex ISR results. The results from this fusion technique and the model, which are currently being published (**Seker et al., 2009),** are shown in **Chapter 3** and discussed in detail in **Chapter 4**.

As mentioned earlier, each beam of AO ISR can be operated in two modes: the fixed-zenith (vertical-beam) mode and the azimuth-scanning (beam-swinging) mode. In the azimuth-scanning mode, the radar beam is swept 0º-360º-0º cyclically (0º being north and 180º being south), usually at a 15º-zenith angle, and with an approximate period of 16 minutes per half-cycle. Although data from the radar in beam-swinging (azimuth-scanning) mode provide additional information, such as electric fields and plasma drifts which can not be obtained if the beam is vertical, medium-scale features are blurred and artificial periodic vertical striations are introduced in the ISR results as a result of this rapid swing of the beam. Fixed-beam and corresponding azimuth-scanning ISR RTI plots from the same time interval in **Figure 2.6** illustrate how the dark spikes caused by the propagating MSTIDs alias in time and space due to beam swinging. **Figures 2.6a** and **2.6b** show the same MSTID structure observed by both the vertical linefeed beam and the azimuth-scanning Gregorian beam. As can be seen, although both beams sample the same ionospheric structure, it is much more difficult to interpret the azimuth-scanning result compared to the fixed-beam result without the assistance of allsky images.

Although, at AO, this swing can occur at a maximum of 15º zenith-angle, nevertheless, at F-region heights, it involves considerable and relatively rapid horizontal motion providing a link to the imager results which can provide the horizontal structure only. More specifically, the diameter of the circle on which the beam swings reaches 160 km at 300 km altitude, which is similar to the horizontal wavelength of MSTIDs. And, the beam full-circle period (16 minutes) is much shorter relative to the horizontal propagation period of MSTIDs (~1 hour) enabling the study of the 3D structure of a single MSTID band when the ISR data are used in conjunction with the allsky images. Therefore, the imager and radar data can be used together to better analyze the plasma features, especially when the radar beam is swinging. In other words, the fusion technique described here is most useful if the radar beam is in azimuth-scanning mode, providing spatial information to compare with the images.

In summary, this fusion technique is based on the core idea that when the ISR beam is azimuth-scanning (fast enough) it becomes possible to obtain vertical information from different parts of a single depletion band by means of determining the beam location in the allsky images. It should be noted that this technique requires the radar to have beam-scanning capability and a high signal-to-noise-ratio (SNR) since the faster the beam rotates, the less the SNR becomes due to shorter time-averaging. The necessary calculations are done automatically by means of a computer code. The steps taken are as follows:

1) The exact time of each allsky image is found.
2) The corresponding vertical profile from the ISR data is located and shown on the ISR RTI plot.
3) The depletion height is calculated from the profile using a threshold (in percentage).
4) The azimuth angle for the profile is found.
5) The horizontal location of the beam is calculated from the azimuth angle and assumed airglow emission height.
6) The location of the radar beam, along with its direction, is mapped on the flattened allsky image.

7) The depletion height at the horizontal location of the beam relative to the MSTID band is recorded for analysis.
8) The results are used to understand the three dimensional shape of the MSTID bands.

The technique shown here can also be applied when one of the ISR beams is fixed. This way, the data from the azimuth-scanning beam provide the connection between the imager (horizontal) and ISR (vertical) datasets whereas the data from the fixed beam provides unaliased vertical information that is easier to interpret. However, no such dataset (that includes azimuth-scanning beam, vertical beam, and allsky imager) was available for this study.

2.3. Empirical Model of MSTIDs

To confirm and further investigate the observational findings summarized above, a model is necessary. A simple empirical 3D model of the nighttime MSTID bands is constructed to better understand the relationship between imager and ISR observations, and for successful interpretation of the complex (aliased) ISR azimuth-scanning results. That is, the swinging beam provides complex (time/location aliased) vertical and horizontal local information, while the allsky image provides only horizontal information on the mesoscale, allowing us to construct a simple 3D model of MSTIDs based on these observations. This model is designed to replicate the allsky imager and ISR observations, and so the model parameters are adjusted to reproduce what the radar and allsky imager see. The model, in-turn, proves to be very useful for interpretation of the azimuth-scanning radar results.

The model consists of a 3D array in which the value of each pixel represents the electron concentration for that location. The geometry and intensity of the model MSTID bands and the background ionosphere are based on observations. 3D sketches of the modeled MSTID bands from various look-angles in addition to vertical and horizontal (along and across the MSTID bands) cross-sections are given in **Figure 2.7**. The F-layer (and its vertical oscillation due to MTM-BW) is shown in the cross-sectional **Figures 2.7b-2.7e**, but not in the 3D sketch in **Figure 2.7a**. The vertical cross-section in **Figure 2.7b** (perpendicular to the bands) looks similar to the ISR result in **Figure 2.1b** since the propagation direction of the MSTIDs is perpendicular to their orientation. The other vertical cross-section in **Figure 2.7e** (parallel to the bands) shows the uplifted F-layer causing the MSTID. As the MSTIDs are modeled to describe the uplift of ionospheric regions (with the shape shown in **Figure 2.7a**), they appear in the horizontal cross-sections as depletion bands or regions at low altitudes (**Figure 2.7c**), and as enhancement bands or regions at high altitudes (**Figure 2.7d**).

The total volume of the model is 500 km (N-S) x 500 km (altitude) x 1250 km (E-W) with a basic resolution cube of 2.5 km on each side (20 million pixels). The total run-time is 10 hrs with a time resolution of 45 s (800 time steps). As this model is based on and tested against June 16-17 and March 22-23, 2004, observations, we use four consecutive (periodic) slabs or bands all of which have the same shape, but each has a different location (in altitude and latitude). As was the actual case for March 22-23 in **Figure 2.2,** one of the bands is farther north and can not be observed by the vertical (fixed-zenith) ISR beam located at the center. The bands get thicker (both horizontally and vertically) farther to the south and have a rounded shape closer to a bubble-shape rather than simple rectangular slabs. The southwestern edge is modeled as nearly vertical since both the vertical beam ISR and allsky observations suggest that the southwestern edge transition is much steeper or sharper than the one on the northeastern or trailing side of the band. The modeled bands cover the whole extent of the model volume along N-S (500 km) and extend from 200-300 km up to 300-400 km in altitude. As in the actual observations, the maximum height of the bands depends on the F-peak height variation due to the midnight collapse. Each band in the model is tilted westward by 30° and downward by 10°, propagating to the southwest with a speed of 125 km/hr and a horizontal wavelength of 125 km which results in a period of 1 hr. The depletion/enhancement transitions are smoothed and a simple night-time F-layer, along with a simple midnight collapse, is also included in the model.

As can be seen from **Figure 2.1b** and **Figure 2.2**, the actual MTM has a vertical collapse of ~100 km and occurs over ~23 LT to ~29 LT, lasting about 6 hrs. Previous studies, such as **Colerico et al. (1996)**, found that the MTM is stationary with respect to the Sun which means it would appear to a stationary observer (such as an allsky imager) to propagate at the same speed with the rotation of the Earth (~1600 km/hr at the equator). This means that the horizontal scale of the MTM must be very large (since 6 hr x 1600 km/hr = 9600 km). The modeled MTM caused midnight collapse (seen as a brightness wave on the imager) replicates the 100 km vertical collapse and is also compressed in horizontal scale to replicate observed midnight collapse behavior through the night. In addition, since the MTM propagation direction does not affect the model ISR result, the MTM is modeled to propagate in the same direction with the MSTID bands for further simplicity. In summary, since only the vertical scale and the time duration of the MTM are relevant for the ISR results, both the horizontal scale and the speed of the MTM used in the model are taken to be more than ten times smaller than the actual values to keep the time duration constant.

Furthermore, a virtual ISR is located at the bottom center of the geometry and its beam swings at 15° zenith with a total period of 30 min (15 min for a full circle with a 6° time step). In addition, an imaginary allsky imager that shows the horizontal data averaged from 200-300 km is utilized for comparisons with the actual allsky imager observations. The MSTID bands are modeled such that they have similar parameters with the ones calculated from the allsky images and ISR RTI plots. **Table 2.2** summarizes the parameters of the model and the computer code of the model (written in IDL) is provided in the **Appendix.**

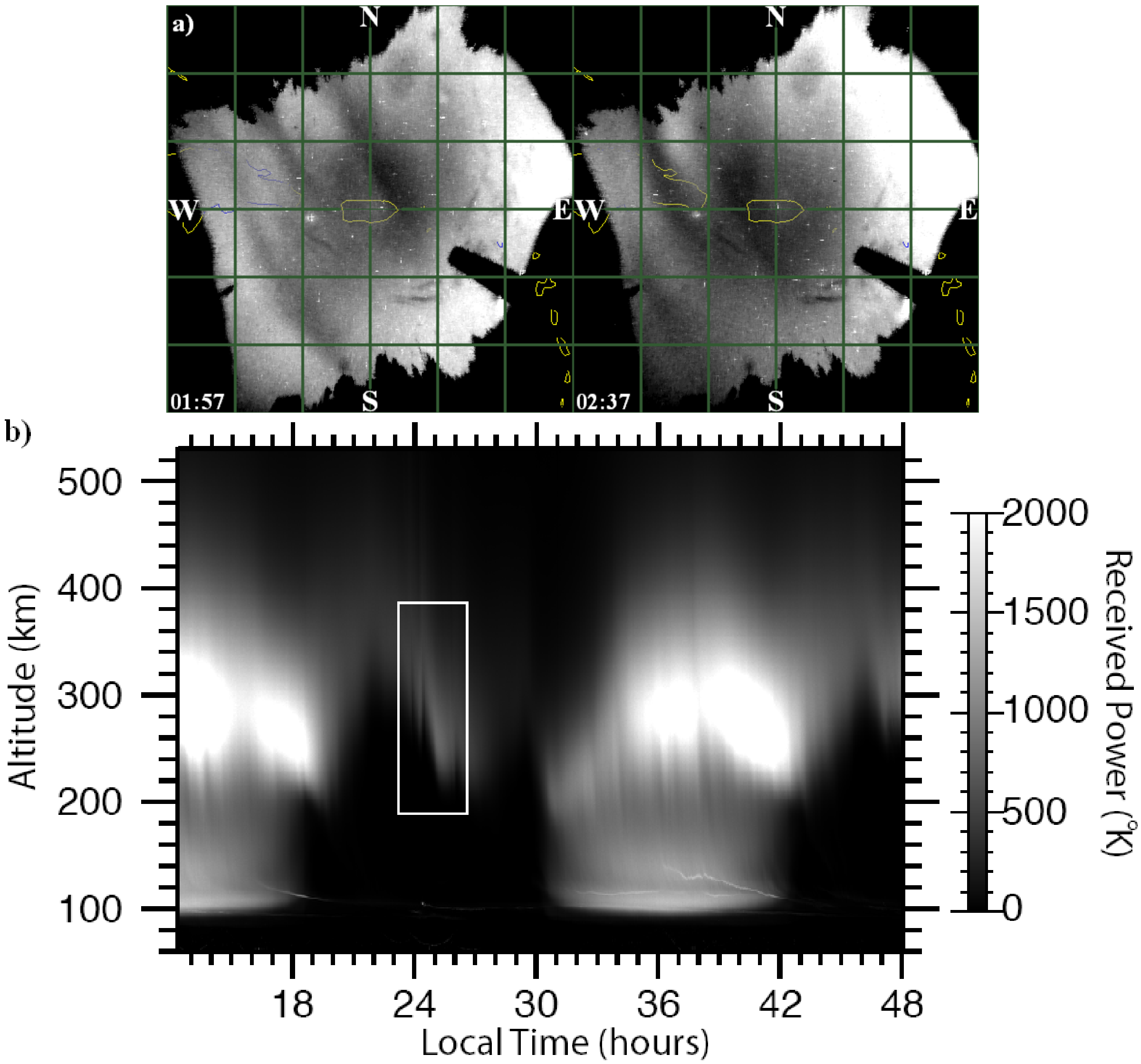

Figure 2.1. (a) Two allsky images from March 22-23, 2004, mapped to geographical coordinates. The grid size is 200 km x 200 km. (b) Corresponding vertical ISR observation. The spikes caused by the MSTIDs are shown with a rectangle. **(Seker, 2006)**

Table 2.1. MSTID parameters (from the allsky imager and ISR observations).

Horizontal thickness	50-250 km
Horizontal wavelength	100-200 km
Horizontal speed	100-200 km/hr
Vertical extent	~100 km
Period	~1 hr
Intensity variation	5-15%
Tilt angle	20°-40° westward from north

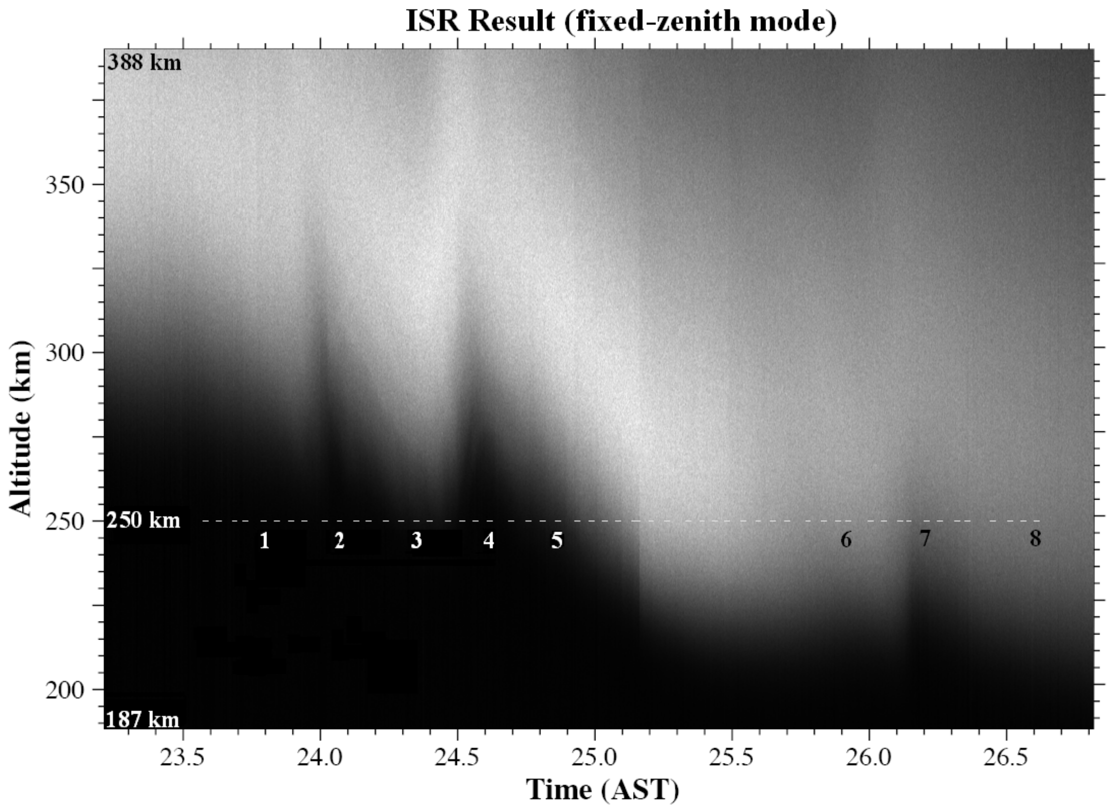

Figure 2.2. The rectangular region of **Figure 2.1b** in more detail. The dashed lines and numbers shown in the figure correspond to the available allsky images and the images shown in **Figure 2.3**, respectively. Three dark spikes caused by uplift of the ionosphere are clearly visible. (**Seker, 2006**)

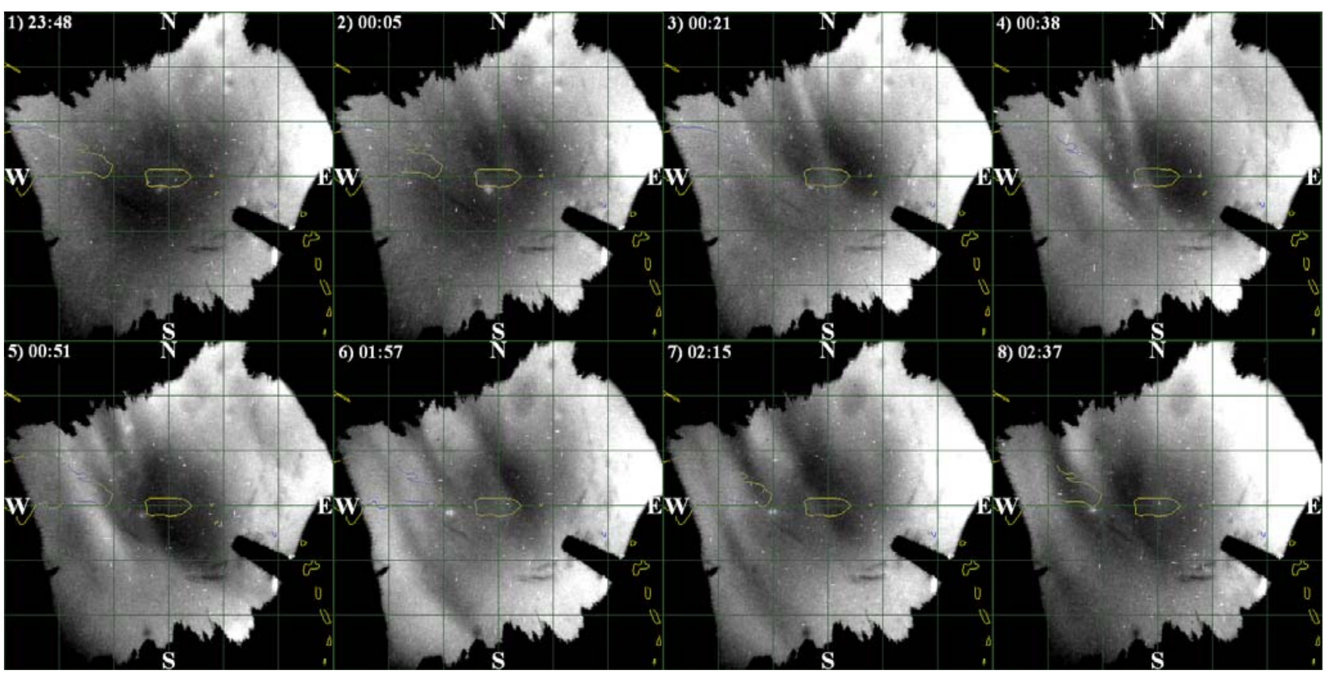

Figure 2.3. Allsky images taken with the 630 nm filter of PSASI. The grid size is 200 km × 200 km. The island of Puerto Rico is shown with a yellow contour at the center of each frame. The frame numbers correspond to the numbers shown in the ISR result in **Figure 2.2**. The frames illustrate the bubble shape and southwestward propagation of the MSTID depletion bands. (**Seker, 2006**)

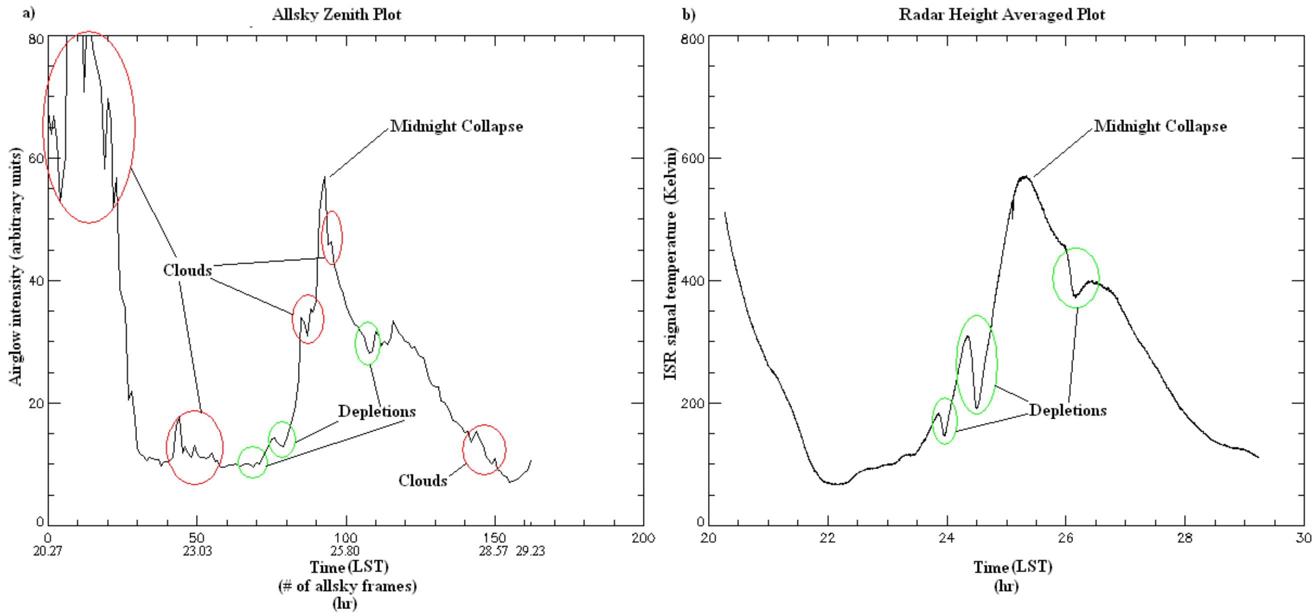

Figure 2.4. (a) The airglow intensity (in arbitrary units) at the center of allsky images vs. time. (b) The corresponding ISR signal temperatures in time averaged through the 630 nm airglow layer (from 210 km to 330 km). Depletion bands, clouds, and midnight collapse are indicated. (**Seker, 2006**)

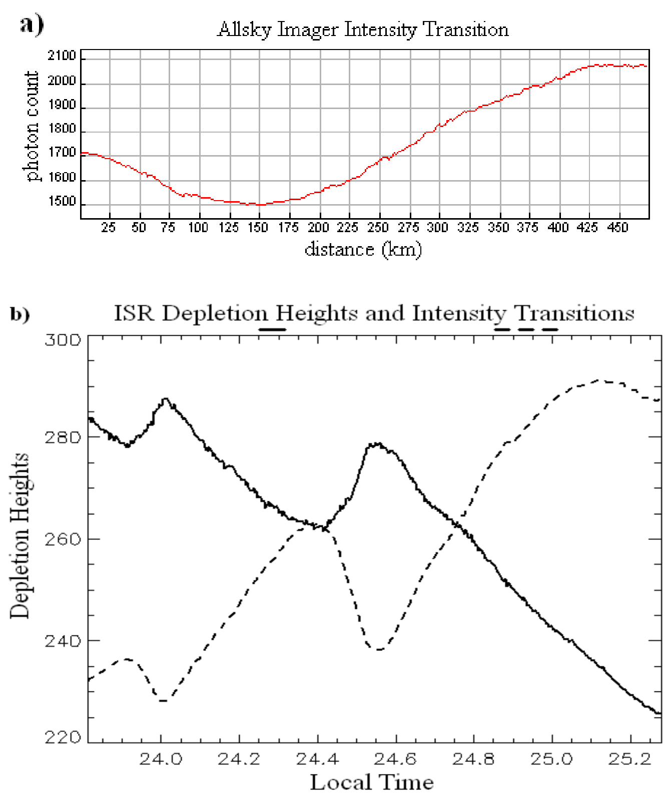

Figure 2.5. (a) The airglow intensity across the thick depletion band at 24.5 LT. (b) The ISR electron concentration (shown with dashed-lines) averaged from 300 km to 330 km across the two MSTID bands at 24 LT and 24.6 LT and the heights of the depletions calculated using a constant threshold for each ISR vertical profile. The electron concentration is shown with arbitrary units since it is normalized in order to show the two results in the same plot. These results confirm that the intensity transition at the southwestern edge of an MSTID band is sharper than the transition at its northeastern edge.

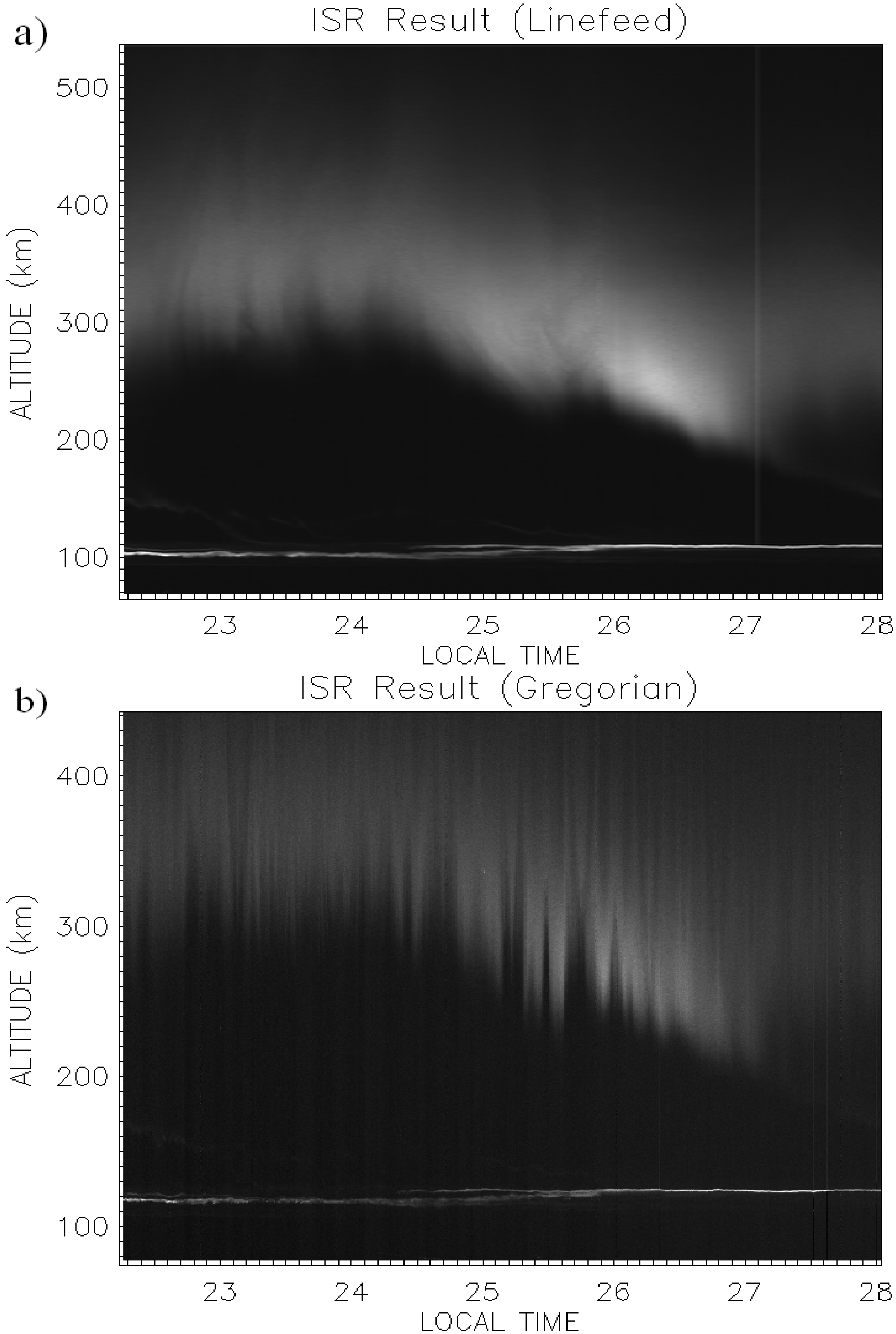

Figure 2.6. (a) Vertical-beam ISR RTI plot from 21-22 September 2005. (b) The corresponding azimuth-scanning ISR result illustrating the vertical striations caused by the beam swinging.

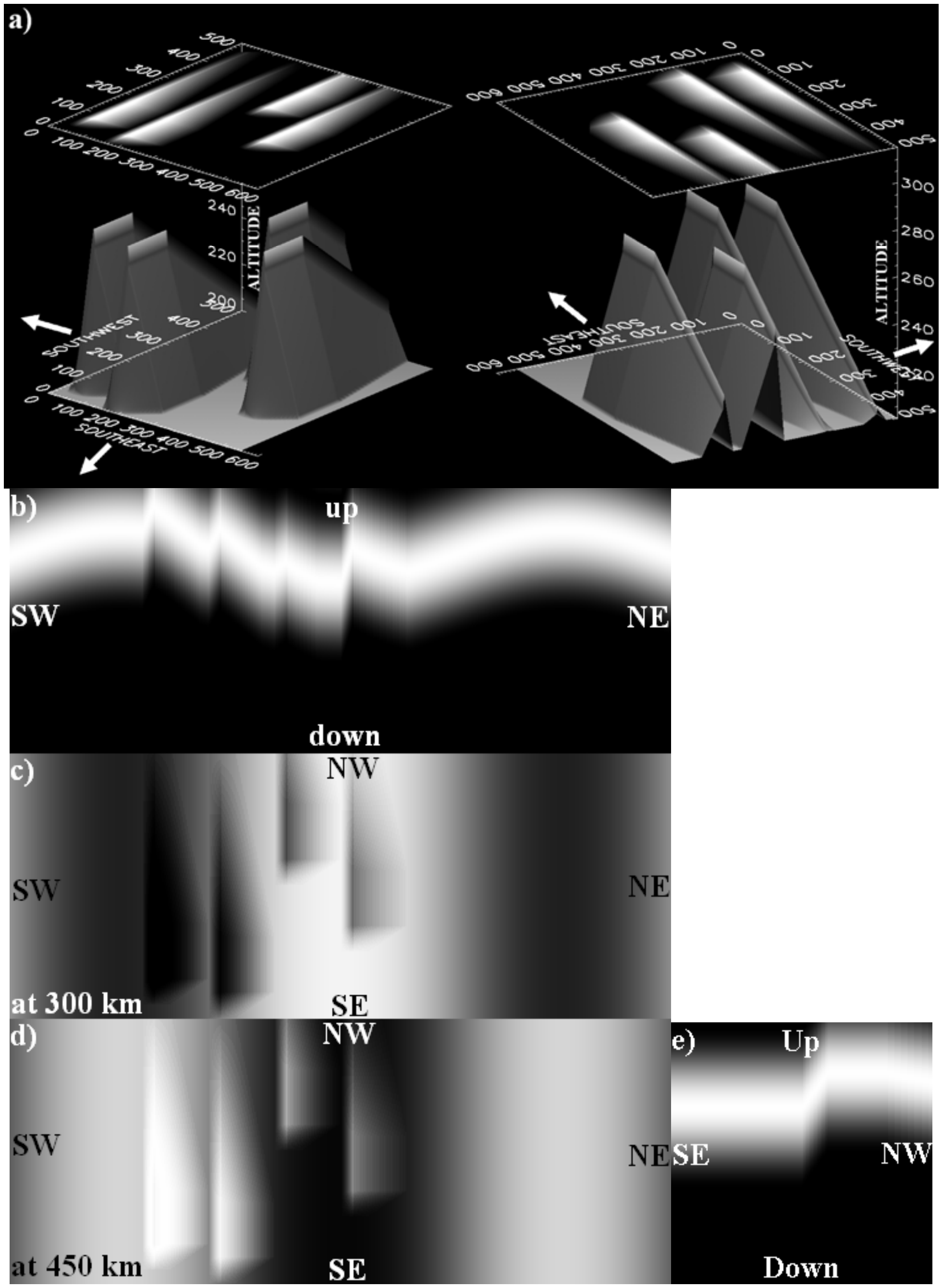

Figure 2.7. (a) 3-D sketches from two different look angles showing the geometry of the empirically modeled MSTID bands. The effect of midnight collapse on the altitudes is excluded. The vertical tilt angle seems to be much more than the actual tilt (10°) since the vertical and horizontal scales of the plot are different. Cross-sections of the model (b) parallel to the bands (along NW-SE), (c)-(d) at two different altitudes, and (e) perpendicular to the bands (along SW-NE). The directions shown are not the geomagnetic directions since the horizontal tilt of the bands (~30° westward from the north) is slightly different than that of the field lines (~10° westward from the north).

Table 2.2. Model parameters

Volume	500 km (N-S) x 500 km (altitude) x 1250 km (E-W)
Total Time	10 hrs
Spatial Resolution	2.5 km (200 x 200 x 500 = 20 million pixels)
Time Resolution	45 sec (800 time steps)
MSTID Altitude Extent	depletions from 200-300 km to 300-400 km (varies with F-layer altitude) enhancements from 400-500 km to 500-600 km (varies with F-layer altitude)
N-S Extent	~500 km (different N-S position for each band)
(Horizontal) Wavelength	125 km (thicker further south to count for the bubble shape)
(Horizontal) Speed	125 km/hr
(Horizontal) Period	1 hr
Alignment	30° westward (horizontal), 10° downward (vertical) from north
ISR	beam swings at 15° zenith, 30 min full period,18° per time step
Imager	averaged from 200 km to 300 km
Included	smooth edges, F layer, midnight collapse, bubble shape, sharp southwestern edge

3. RESULTS

This chapter has two main sections. The first section shows the results of applying the fusion technique described in the previous chapter to a specific MSTID event observed both by the allsky imager and the azimuth-scanning ISR at Arecibo. The second section presents the results from the empirical model and compares them with the actual observations.

3.1. Fusion of Imager and Radar Observations

A typical azimuth-scanning ISR result from AO is shown in **Figure 3.1**. The observations, which cover around 40 hours, were made with both Gregorian and linefeed beams in azimuth-scanning mode on 16-18 June 2004, a geomagnetically quiet period (Kp~2). The durations of the midnight collapse for each night are indicated by the two bars at the bottom of the figure. Even though the azimuth-scanning may blur the details, spike-like depleted plasma features can still be observed clearly during the night of 16-17 June as highlighted by a rectangle. The MSTID bands observed in June 2004 are not as intense as the ones observed in March 2004 and the MSTID bands appear distorted due to azimuth-scanning which makes it more difficult to directly compare the imager and radar results. Nevertheless, the azimuth-scanning mode provides E-field and plasma drift information and makes it possible to better fuse the radar and imager results using the aforementioned technique.

The dark spikes caused by the MSTIDs and beam swinging are highlighted in **Figure 3.2** which reveals the fine details of the features in the rectangular area of **Figure 3.1**. The two long lines at the top show the time intervals of the two separate MSTID bands passing over the radar. The squares/circles, the letters A and B, and the short lines at high altitudes are placed to show the effects of 3D geometry on the azimuth-scanning ISR data and their meanings will be explained later in this section. In addition, an azimuth angle versus time plot is inserted above **Figures 3.2a** and **3.2b** to emphasize the effect of beam swinging on the ISR data. The dots (located at approximately 260 km) correspond to the times of all available allsky images from that night. **Figure 3.3** shows a series of allsky images taken by PSASI during the night of 16-17 June 2004. The times of the allsky frames correspond to the times labeled with letters (a through p) in **Figure 3.2**. The arrow indicates the location of the ISR beam at 630 nm airglow altitude, and the white dot at the center of the frames correspond to the zenith of the radar. The other dot corresponds to the geographic north location of the radar beam at 250 km and the arrow shows which way the radar beam is rotating. The yellow contour shows the island of Puerto Rico.

As shown in **Figure 3.2a** and **Figure 3.3**, it is possible to precisely track the MSTID bands even when the radar is in azimuth-scanning mode by means of locating the radar beam in the allsky images. For example, from the allsky images in frames c, h, k, and n of **Figure 3.3**, it is seen that the ISR beam is pointing at the MSTID band while the ISR data shows uplifted/depleted regions. Similarly, in frames a, e, and f, the ISR beam is pointing at an enhanced region while the ISR data shows enhanced electron concentration. Most importantly, there are the transition regions (edges) which prove how well the two data sets agree with each other. For example, frames d, i, and k in both **Figures 3.2a** and **3.3** correspond to the regions where the beam is about to transit from depletion to enhancement; and the frames b, j and m correspond to the regions where the beam is about to transit from enhancement to depletion. The position of the radar beam relative to the position of the MSTID structures seems to be very critical. For example, in frame j of **Figure 3.3**, the radar beam is slightly off the depleted region and the corresponding ISR profile in **Figure 3.2a** is an enhancement profile, not a depletion one. This illustrates how sharp the gradients at the edges of these MSTID bands are, a fact which was also found by previous studies such as **Makela et al. (2001a)**. Clearly, the very narrow radar beam (~1 km width at 300 km range) gives only very local information.

Furthermore, in the ISR plot, a single MSTID band appears as multiple narrow bands as a result of the beam swinging, as is the case in **Figure 3.2**. In other words, packets of several thin spikes seen in azimuth-scanning ISR data are actually created by a single MSTID band. However tracking the ISR beam in the allsky images, as was done in **Figure 3.3,** reveals whether the depletion spikes in the ISR plot are created by the same MSTID band or not. For example, there are several spikes in the ISR data for each of the two depletion bands, shown by the long black lines at the top of the plot. That is, the thickness and spacing of the spikes vary for a single band due to the relative motion between the swinging radar beam and MSTID bands. This will also be demonstrated in the next section using a 3D model that is based on the observations. Another common feature of the swinging beam data is the fork-shaped spike pairs (e.g., indicated with "A" and "B" in **Figures 3.2a** and **3.2b**). The time between each leg of the pair varies. Comparison with the allsky images reveals that these spike pairs are the artifacts of the observation of the northern parts of a band with swinging beam. As the beam swings around geographic north, when the depletion band is located slightly west of north, the beam passes through this MSTID band twice, moving in opposite directions, and that creates the fork with legs appearing close to each other. Similarly, when the depletion band appears farther to the west (after it propagates farther southwest), this would create a larger time delay between two legs. The beam usually catches the band at the southeast also, but since there is no beam direction reversal south (north for line feed), this results in a single thick spike in the ISR data. This also explains the reason for seeing double-spikes and thicker spikes often in series. This double-spike feature is also demonstrated in the next section using a 3D model.

As mentioned earlier, the major advantage of using the allsky images in conjunction with the ISR (in scanning mode) is that it enables the study of the three dimensional structure of the ionospheric structures such as MSTIDs. More specifically, by tracking the location of the radar beam at airglow altitudes on the allsky images, the vertical extent of the depletion can be found at different locations within a single depletion band. For instance, the depletions at points k, n, and o in **Figure 3.3** do not extend as high as the depletion at point g. The squares (circles) in this figure represent the points in time when the ISR beam was pointing at (geomagnetically) northern (southern) parts of a band. The selection between a circle and a square is made by finding the location of the ISR beam relative to the band in the corresponding allsky image and assuming the slab remains approximately fixed between each allsky frame (~ 4 min). It should be kept in mind that the azimuthal locations of the squares (circles) will only be to the NW (SE) when the structure is directly over the radar. The altitudes of the squares/circles are found by applying an intensity threshold to the radar data and they show the maximum heights of the depletions (the upper limit of the slabs). We found that a constant threshold of 10% of the average maximum electron concentration best defines the bottom-side of the F-region when there is no depletion. On the other hand, the calculated heights of the depletion peaks match the observed heights the most when the threshold is taken to be 70% of the average maximum. Since we are interested only in the height of the depletions rather than the base of the F-region, we used a 70% threshold. It is apparent in the figure that the circles are always higher than the nearby squares (as also demonstrated in the next section and in **Seker et al. (2009)** using a 3D model), meaning that the <u>southern part of an MSTID band reaches higher altitudes than the northern part</u>. This new finding is further confirmed by comparing the Gregorian and line feed data which allows us to compare two different points in space simultaneously. **Figure 3.4** shows the allsky frames corresponding to the letters A and B in **Figures 3.2a** and **3.2b**. G and L represent the Gregorian and line feed, respectively. In **Figure 3.4A**, the Gregorian beam is at the southern part of the MSTID band, whereas the line feed beam is at the northern part. And, as expected, the corresponding spike in **Figure 3.2a** (labeled with circle A) is at a higher altitude than the corresponding spike in **Figure 3.2b** (labeled with square A). The beams switch positions in **Figure 3.4B**. The Gregorian beam is now at the northern part of the MSTID band, whereas the line feed beam is at the southern part. So, the corresponding spike in **Figure 3.2a** (labeled with square B) is now at a lower altitude than the corresponding spike in **Figure 3.2b** (labeled with circle B). This is an important result, since it again suggests that the MSTID bands are tilted vertically with the northern component of the depletion band at a lower altitude than the southern component.

Figure 3.5 shows the smoothened ISR beam profiles corresponding to B in **Figures 3.2** and **3.4**. The threshold for calculating the heights of the squares and circles in **Figure 3.2** is also shown. These results suggest the sketch of the vertical cross-section of a tilted MSTID band shown in **Figure 3.6**. The positions of the ISR beam at northern and southern parts of the MSTID band are also indicated. It is found from the geometry in **Figure 3.6** that the equation relating the height ratio to the dip angle is $\alpha = \arctan[2h_2/h_1 - 1.7] - 15°$. According to **Figure 3.5**, the maximum height difference is only 319 km – 286 km = 33 km (h_2/h_1 = ~1.12), which corresponds to a vertical tilt angle of ~12°. Although this tilt is similar in direction to that of the magnetic field line, it is much smaller than the actual magnetic dip angle which is ~46° at AO. Since the actual height differences between the squares and circles are usually smaller, it seems that the vertical tilt of the depletion bands is usually even smaller than 12°.

An alternative explanation that does not have to exclude the vertical field-alignment is related to the shape of the structures. For instance, if these bands are like vertically field-aligned elongated bubbles (that are curved at the southern tip), they could appear as vertically tilted less or even in opposite direction, depending on the relative position of the band with respect to the ISR beam as shown in **Figure 3.6**. The same result is observed when the ISR beams are not located at the center of the MSTID band. When the beams are pointing near the edges of the MSTID band, the apparent tilt in the ISR data is less than that of the geomagnetic field-line. This is also likely due to the curvature of the side (E-W) edges of the MSTID bands. Apparently, the bands are tilted more (more vertical) at the center and less tilted (more horizontal) at the edges. That is, the depletion band edges are rounded.

Finally, the high altitude bands, which vary with the swing period, are indicated with short lines in **Figure 3.2**. It seems that these high altitude bands exist even before or after the occurrence of MSTID bands, and their durations (i.e., the length of the short lines) appear to get shorter during the passage of MSTID bands. These two features are replicated with an empirical model which will be shown in the next section and discussed in **Section 4.1.2.** Furthermore, these high altitude bands are inverted or shifted relative to the lower altitude bands and spikes. This is expected, since each of these high altitude bands is mainly due to a neighboring band at a particular instant, and not due to the one just overhead. At high altitudes, the tilted beam extends enough horizontally to detect the nearby band. The neighbor of a dark band is an enhanced band and vice versa. As a result, each high altitude band appears as intensity-inversed with respect to the (over-head) band that appears at lower altitudes for that particular time instant in the ISR RTI plot. This is also confirmed using allsky images and is replicated in the next section using an empirical model.

3.2. Empirical Model of MSTIDs

Figure 3.7 compares actual allsky images from PSASI and the synthesized allsky images from the empirical model which was introduced in **Section 2.3**. The imaginary allsky image in **Figure 3.7b** is created simply by vertical integration of the electron concentration from 200 km up to 300 km altitude. Although the actual airglow mechanism in **Figure 3.7a** is much more complex, the averaging serves well for our purpose, which is to make certain the horizontal shape, size, orientation, and speed of the structures are similar in both sets of results. As is obvious from the comparison, the shape of the modeled structures resembles that of the actual depletion bubbles (i.e., the southwestern edge is sharper and the bands become larger farther south). Also, the MTM-caused midnight collapse appears in the model allsky images as a large scale brightness wave covering the field of view.

Figure 3.8 shows the synthesized ISR results from the model, demonstrating the separate effects of the MTM and the MSTID bands on the ISR results. The ISR beam is vertical in the upper panel and azimuth-scanning in the lower one, whereas the left and right sides of each panel show the results for MTM only and MSTID only cases, respectively. As can be seen however, the ISR vertical striations can manifest from both MTM and MSTIDs. It is important to emphasize once again that the MSTIDs would only cause the lower altitude striations, not the high altitude ones, if they were only depletions instead of being caused by uplift of the F-layer.

In order to make certain that the empirical model is valid, it is essential to demonstrate that the results from the model ISR and the actual ISR closely agree with each other. Once this is accomplished for the vertical radar beam, it is expected that the azimuth-scanning ISR results from the model and observations will also be similar. Model details are then adjusted to obtain maximal agreement in the azimuth-scanning ISR results. **Figures 3.9a** and **3.9b** compare the actual vertical beam (fixed at 0° zenith angle) ISR data from March 22-23, 2004 with the corresponding outputs from the model. As discussed before, the MSTID bands appear as saw-tooth-like triangles with leading (southwestern) edges being much steeper than trailing (north-eastern) edges. As is the case for actual observations (**Figure 3.9a**), the spikes in the model ISR RTI plot also move up and down following the MTM wave, and one of the bands is not detected by the ISR beam and thus is missing in the RTI plot since that band passes to the north of the radar location as **Figure 3.7** shows.

Figure 3.9c shows the observationals from the azimuth-scanning ISR data from June 16-17, 2004. The same dataset was discussed extensively in the previous section**. Figure 3.9d** shows the model ISR RTI plot corresponding to **Figure 3.9b** when the beam is azimuth-scanning (swinging) at 15° zenith angle. The azimuth-angle variations are shown below the plots. This model ISR result (corresponding to the March 22-23, 2004, observations) has many similarities with the actual ISR data shown in **Figure 3.9c**

(corresponding to the June 16-17, 2004, observations). Although **Figures 3.9c and 3.9d** are not from the same date (as we could not locate a date that included data from both azimuth-scanning and vertical beams in addition to the allsky images), the comparison is still valuable since most MSTID bands have similar properties. These results are discussed in detail in the next chapter.

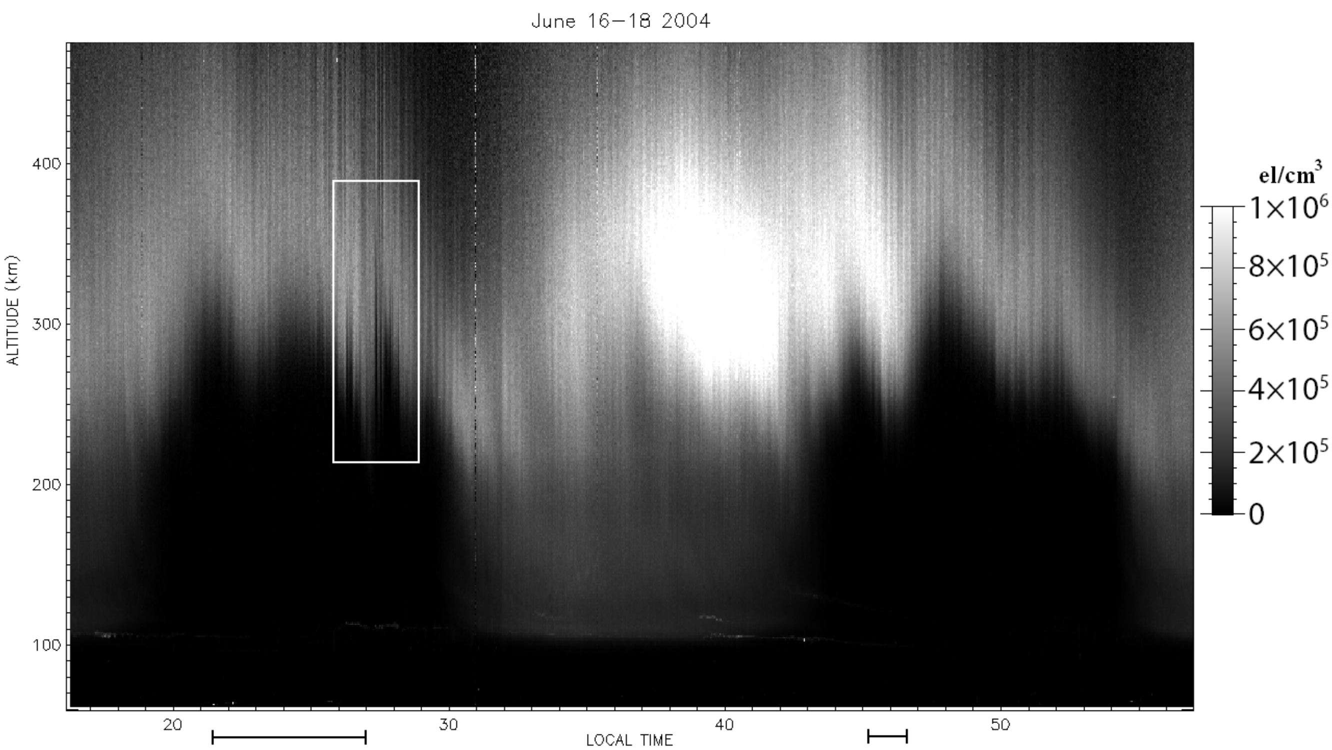

Figure 3.1. A typical azimuth-scanning (Gregorian beam) AO ISR RTI plot from 16-18 June 2004. The zenith angle is 15º. The lines at the bottom of the figure indicate the approximate duration of the midnight collapse. (**Seker, 2006**)

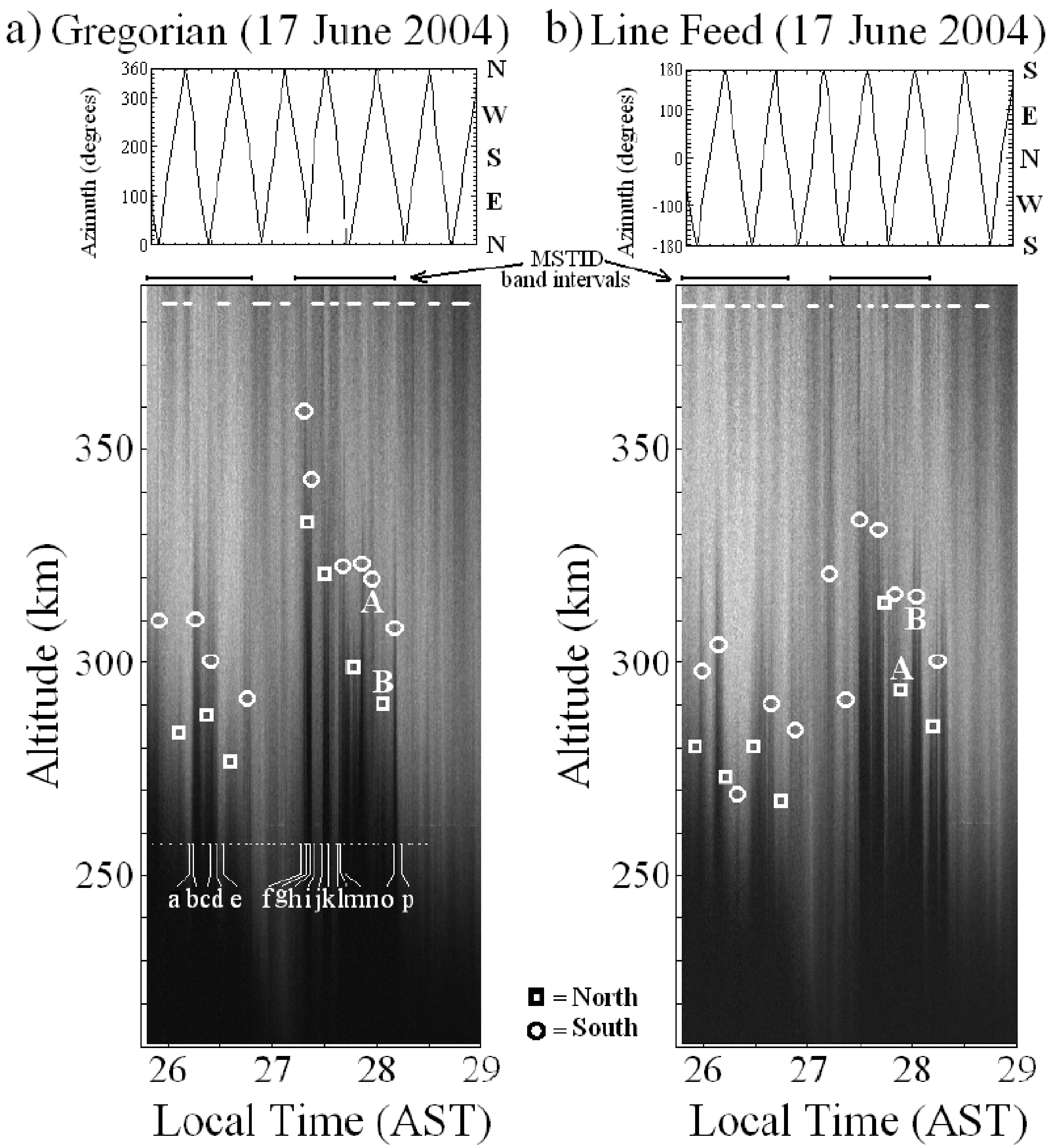

Figure 3.2. The rectangular area of **Figure 3.1** in more detail. The dots at around 260 km and the letters in (a) correspond to all available allsky images from that night and to the allsky images shown in **Figure 3.3,** respectively. The allsky frames corresponding to letters A and B are shown in **Figure 3.4.** The long black lines at the top represent the two MSTID bands passing over. The white lines at high altitudes show the high altitude striations, and the squares (circles) correspond to the height of the spikes when the beam is positioned at northern (southern) parts of a depletion band. Azimuth angle variation is also shown to indicate the direction of the radar beam. The very distinct edges, for example at around 27.5 hrs, reveal very sharp edges in the F-region plasma distribution. (b) Corresponding data from the linefeed that is pointed 180° from the Gregorian feed.

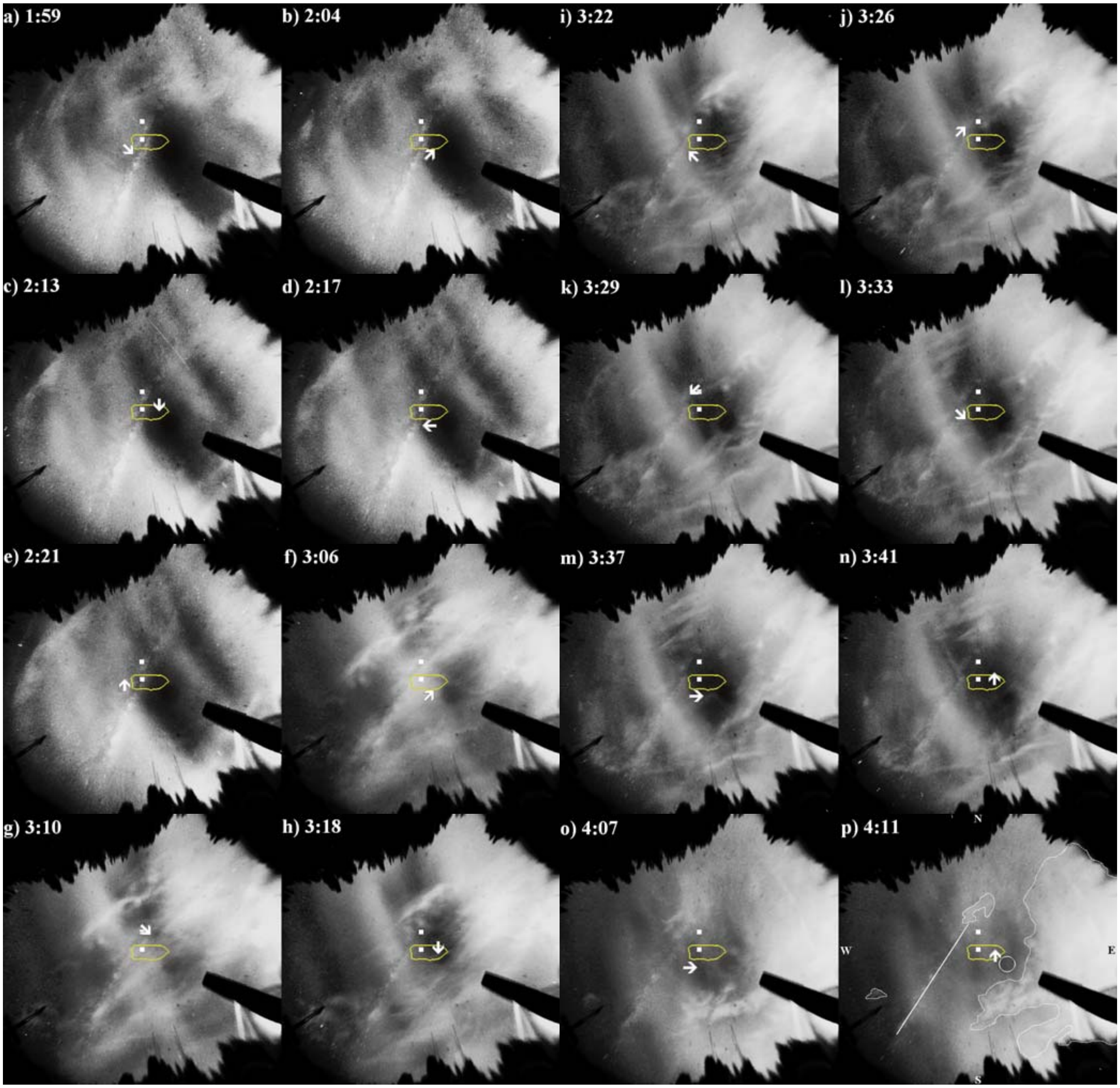

Figure 3.3. Flattened 60 s time-averaged allsky images from PSASI corresponding to the times labeled with letters in **Figure 3.2a**. The rotating arrow indicates the location (at ~250 km) of the ISR beam and direction, and the two dots at and near the center of the frames correspond to the zenith and north (i.e., 0º azimuth angle) directions (at 250 km), respectively. The yellow contour shows the island of Puerto Rico (~ 150 km x 50 km). The images are enhanced by removing the stars using a median filter and performing histogram equalization in order to show the weak plasma depletion event (i.e., MSTID bands) with a better contrast. The depletions are partially blocked by clouds, especially between 3 am and 4 am. Features that can be seen in the images along with the geographical directions are indicated in the last frame p. Clouds are contoured and the Milky Way galactic plane is shown with a line. The relatively darker, fixed, circular region (shown with a white circle) is due to dirt on one of the optical lenses.

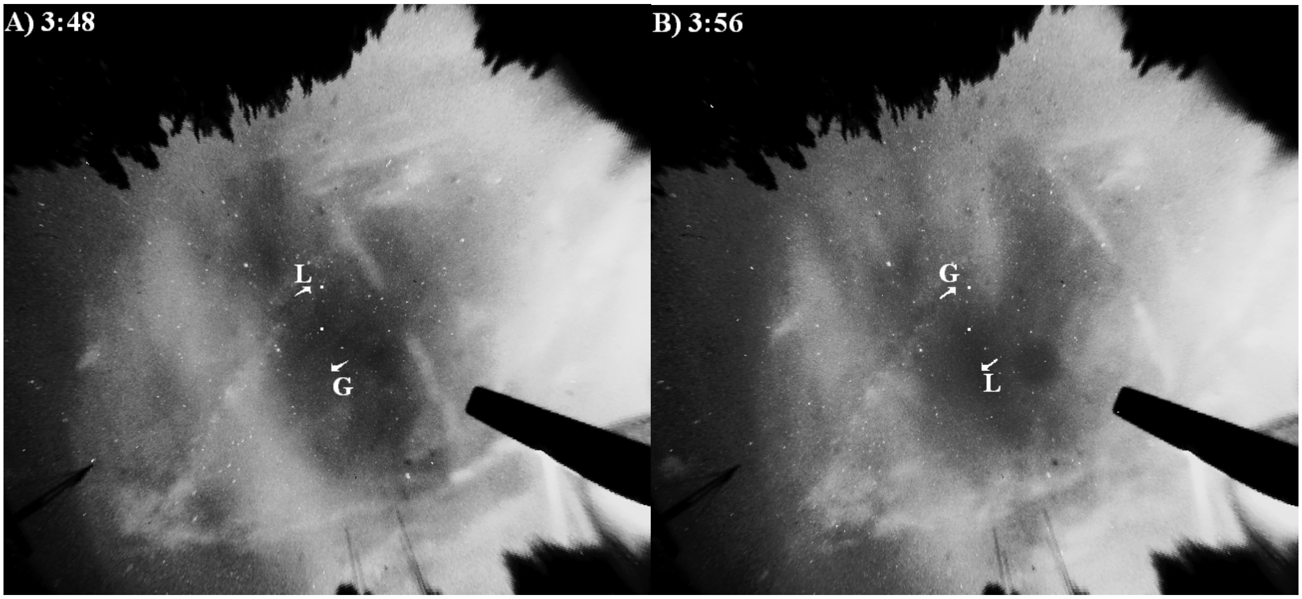

Figure 3.4. The allsky frames corresponding to A and B in **Figure 3.2**. L and G show the location of the line feed and Gregorian beams, respectively.

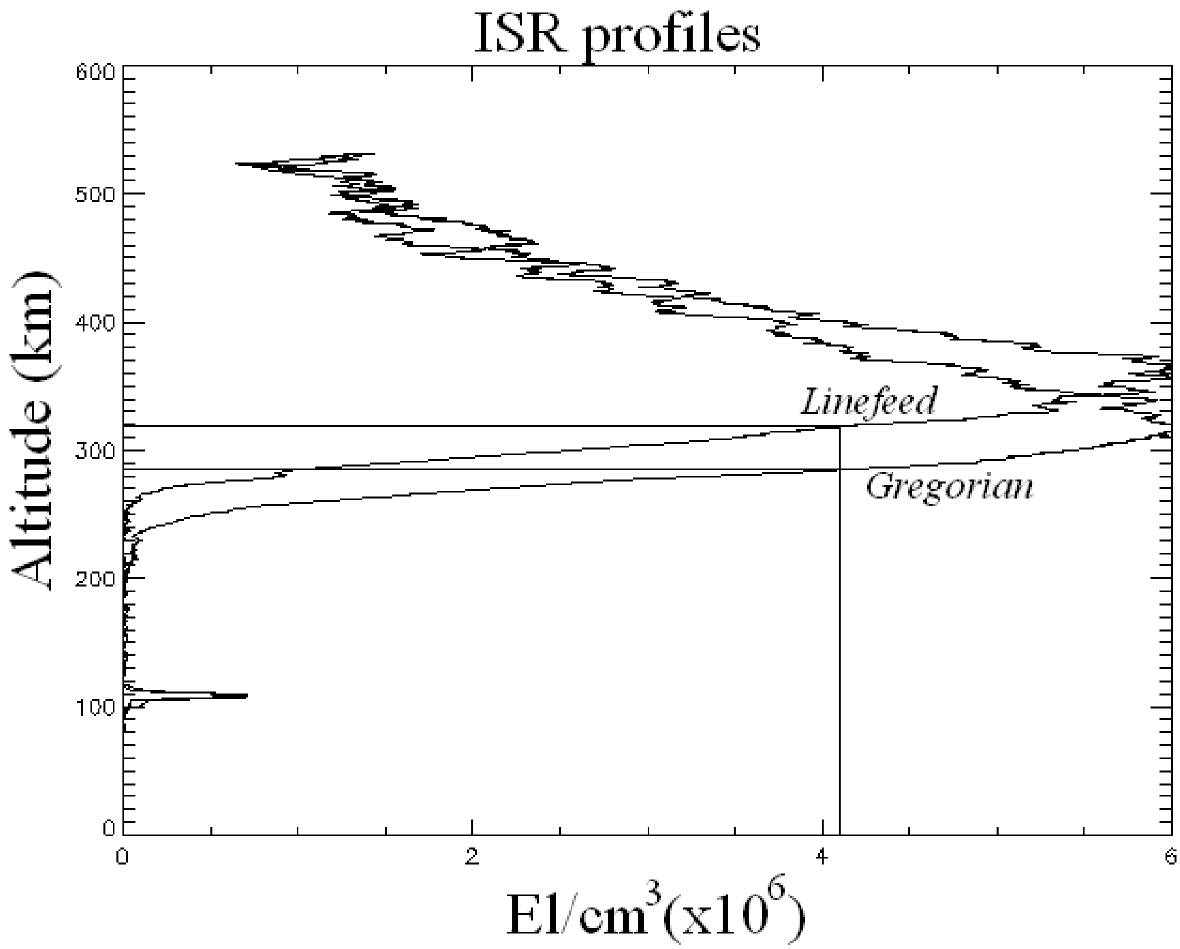

Figure 3.5. ISR (linefeed and Gregorian) beam profiles at around 4 am (corresponding to B in **Figures 3.2** and **3.4**). A threshold value of $4.1x10^6$ el/cm^3 (~70% of the maximum) is used to calculate the depletion heights h_2 and h_1 that are shown in **Figure 3.6**.

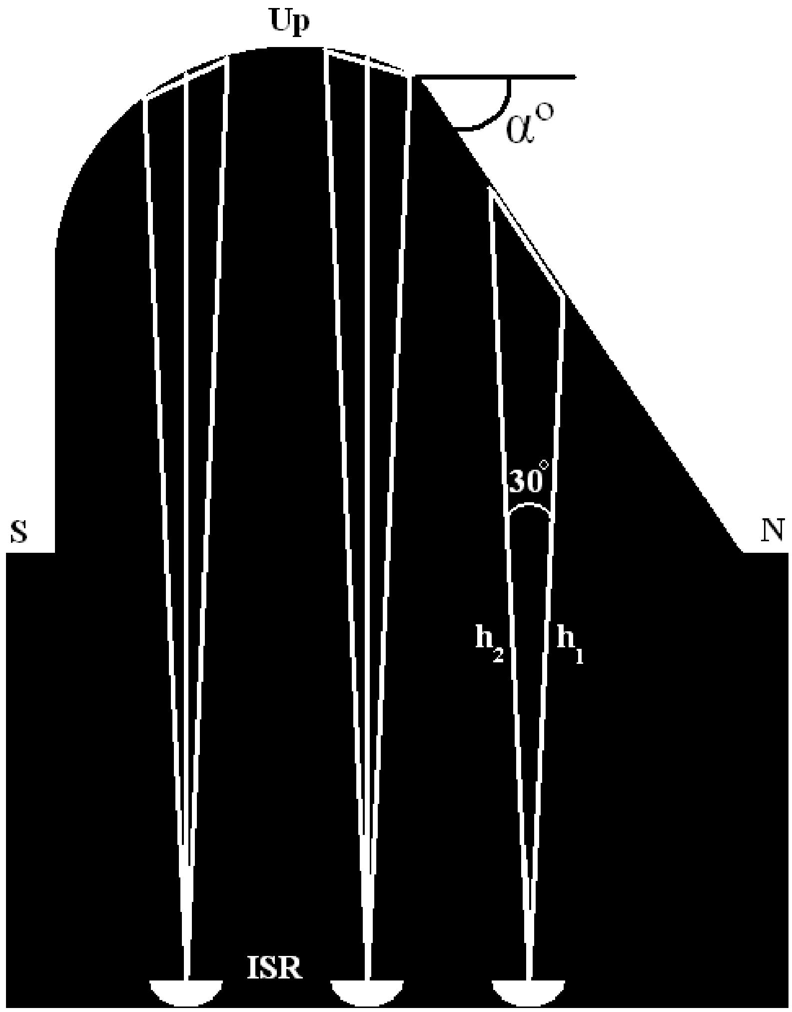

Figure 3.6. Sketch of the vertical cross-section of a tilted MSTID band. The geomagnetic north and south are labeled as N and S, respectively. The three lines represent the zenith and the ISR beam's positions at geomagnetic north and south. Different positions of the ISR relative to the MSTID band result in different apparent tilts due to the curvature of the bubble shape.

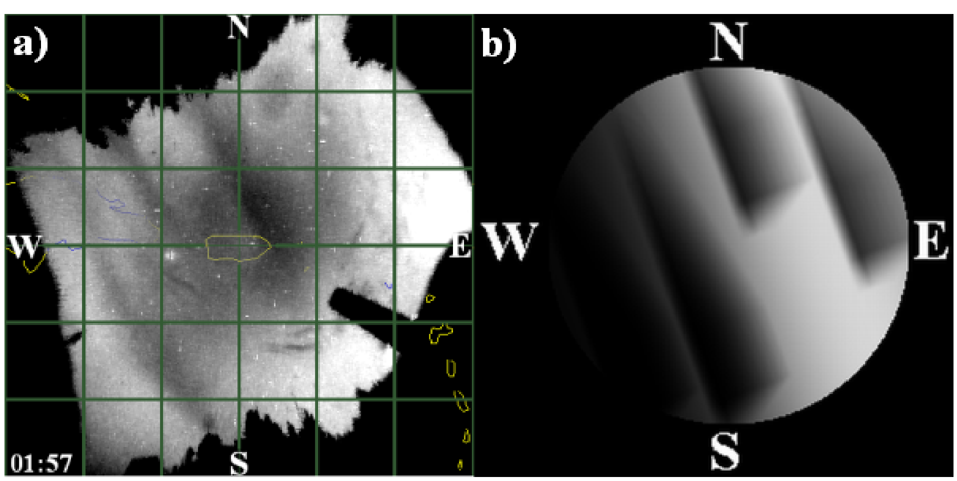

Figure 3.7. (a) A real allsky image from PSASI. (b) An imaginary allsky image from the model.

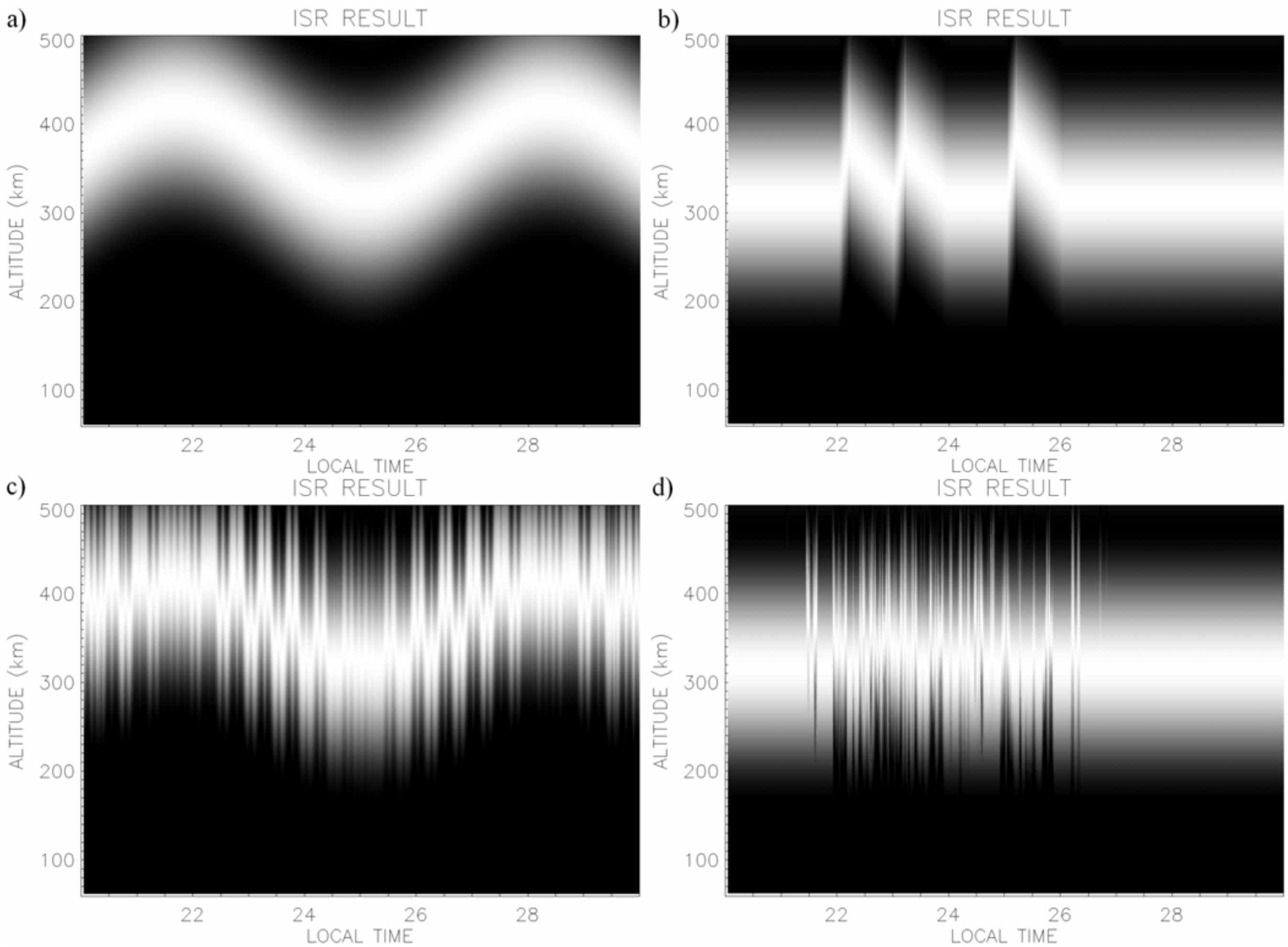

Figure 3.8. Synthesized ISR results from the model. First row: vertical ISR beam; (a) MTM only, (b) MSTID only. Second row: azimuth-scanning ISR beam; (c) MTM only, (d) MSTID only.

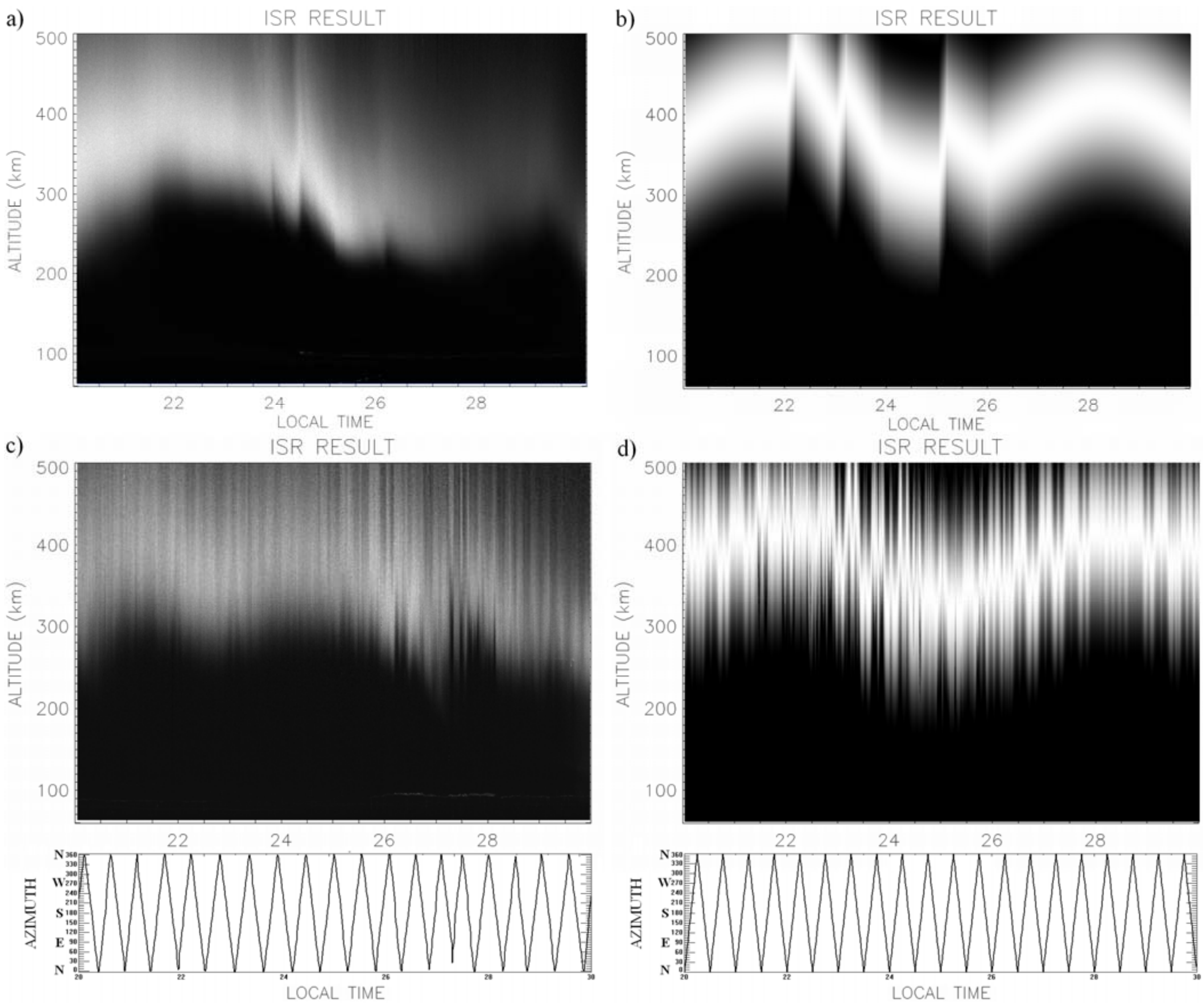

Figure 3.9. (a) Vertical ISR observations from March 22-23, 2004, (b) Vertical ISR result from the model, (c) Azimuth-scanning ISR observations from June 16-17, 2004, (d) Azimuth-scanning ISR result from the model.

4. DISCUSSION

This chapter starts with a discussion of the properties of MSTIDs obtained from the fusion of imager and radar observations, followed by an evaluation of the empirical model results presented in the previous chapter. Afterwards, inferences on the electrodynamics of the MSTIDs based on this and other recent studies will be made. The chapter concludes with a summary of findings and ideas for future research.

4.1. Properties of MSTIDs

4.1.1. Fusion of Imager and Radar Observations

A single instrument alone, such as an allsky imager, is not sufficient for understanding ionospheric structures (such as MSTIDs) since it only provides horizontal information. To better understand the ionosphere one has to use multiple data sets from a variety of instruments. Vertical and azimuth scanning ISR and allsky imager observations complement each other. That is why ISR, which gives mostly vertical information from a very narrow beam, is most useful when used in collaboration with an allsky imager, which gives horizontal information only, and vice-versa. This is especially true when the ISR is in azimuth-scanning mode.

When the ISR beam is swinging, the mesoscale slower variations are modulated by the rapid oscillations (with 16 min. period) that are due to the beam azimuth-scanning across large-scale gradients in the ionosphere. Thus, it is harder to detect waves with ~1 hr period in the azimuth-scanning mode compared to the fixed-zenith mode. In other words, in this case, the ISR data are heavily aliased spatially and temporally. On the other hand, in addition to providing the plasma drift velocities and E-fields, (when used with the allsky images) the azimuth-scanning ISR data also provide information about the vertical structure of the bands at different locations within the band itself. The results shown here reveal that much information about 3D structure of MSTIDs can be learned by using these two instruments together.

The high altitude striations at the beam swing period observed in the ISR result (shown with dashed lines in **Figure 3.2**) are due to the horizontal inhomogeneity of the top-side of the night-time ionosphere. This high altitude horizontal inhomogeneity appears to be caused by two effects: periodic MSTID bands and/or the larger horizontal scale background ionosphere. In **Seker et al. (2008)** it was argued, based on the GPS-TEC results, that the MSTID bands are most likely depletions (not uplifts) that must be periodic and that must reach an altitude of 500 km or more in order for these high-altitude striations to occur. However, further examination of the ISR results reveals that the MSTID depletion bands do not go above 400 km and the high-altitude striations are actually caused by sharp, ~100 km uplift, of the ~200 km thick F-layer. This uplifted layer of ionization is observed as striations as the beam sweeps through the layer at high altitudes. This means there is an enhancement band above each depletion band reaching up to 600 km. This can appear as high-altitude horizontal inhomogeneity assuming that the MSTIDs are highly periodic. A second possibility, which does not require highly periodic MSTIDs, is the diurnal vertical oscillation of the background ionosphere complicated by the MTM (that often appears as the “midnight collapse” in AO ISR results). We clarify these possibilities in the next section using the model we have developed.

Most importantly, from the ISR observations, the bands are found to be tilted vertically. For the first time, it was shown that the southern parts of an MSTID band reach a higher altitude than the northern part. This vertical alignment is similar in direction to the geomagnetic field but the observed maximum tilt angle (~12°) is less than the dip angle at AO (46°). **Livneh et al. (2009)** found, using ISR data from various observation sites, that the vertical wavelength of MSTIDs increases with latitude. This result can also be explained by the vertically tilted (or field-aligned) MSTIDs since the dip angle is larger at high latitudes. The tilt angle is also found to vary depending on the relative positions of the ISR beam and MSTID band. Curvature or rounding on the southern tip of the depletion bubble could explain this as illustrated in **Figure 3.6**.

Certain features seen in allsky images are explained better based on the finding that the MSTID bands are actually vertically tilted structures. First, this interpretation agrees with the inherit assumption of field-alignment of the smaller scale structures inside the depletion bands in the Perkins Instability theory. Second, the bands observed with the imager are actually wider to the south relative to the north, because, if they are vertically tilted, that means they reach higher altitudes to the south and the bubble shape expands as expected due to vertical inhomogeneity of the F-region. This also causes the bands to become more vertical at higher altitudes, as can be observed in the ISR results. The vertical tilt of the MSTID bands (the tilt being similar to the orientation of the magnetic field line) provides clues on their generation mechanism also. In the allsky images (from mid-latitudes), the plasma depletion bands appear mostly from the northern edge of the allsky images. This suggests that they must originate at higher latitudes, and consequently at lower altitudes as a result of the vertical tilt (as can be seen from the field line geometry in **Figure 1.4**). This suggests that these F-region irregularities are possibly seeded by lower altitude (e.g., tropospheric or mesospheric) gravity waves that are generated farther north of AO.

4.1.2. Empirical Model of MSTIDs

Important clues regarding the features seen in the swinging-beam ISR RTI plot were discussed in **Section 3.1** and will be summarized at the end of this chapter. The model presented here serves as a means of confirming these features and providing interpretation of various details. The model is intended to replicate the observations as best as possible. That is, the model, once correctly adjusted, is useful in interpretation of the radar and imager data. The model is tested using an imaginary beam-swinging ISR and allsky imager and comparing their outputs with observations. In this way, certain MSTID features seen in the ISR plots and allsky images are better understood.

The model was designed to replicate the imager and radar data as best as possible. As expected, the major features of the MSTIDs as shown in the real allsky imager and vertical ISR results in **Figures 3.7a** and **3.9a** are replicated in the modeled allsky imager and vertical ISR outputs in **Figures 3.7b** and **3.9b**, respectively. These features include horizontal scale, alignment, propagation direction and speed, elongated bubble shape, the steep southwestern edge, midnight collapse, and depletion spikes or uplifts embedded within it. In addition, as is the case in the actual imager data, each MSTID band has a different horizontal location (or latitude); and as is the case in the actual ISR data, the altitudes of the modeled depletions vary similarly with the altitude of the oscillating F-layer caused by the midnight collapse.

The most obvious feature of the modeled azimuth-scanning ISR RTI plots in **Figure 3.9d** is the periodic vertical striations in the background ionosphere caused by the ISR beam swing and the horizontal inhomogeneity of the night-time F-region. As explained earlier, this horizontal inhomogeneity (and striations) is caused partially by the MSTID bands and partially by the MTM wave. In the model these striations are easily replicated in the top-side and bottom-side ionosphere either by implementing the uplift-caused MSTID bands or simply by introducing the ~6 hr MTM wave modulation thus causing the horizontal inhomogeneity. This is illustrated in **Figure 3.8** which shows that the striations can be caused either by the midnight collapse or the MSTID bands (caused by the uplift of the nighttime F-layer). Although each striation type appears differently in the model azimuth-scanning ISR results in **Figures**

3.8c and **3.8d**, the combined model result in **Figure 3.9d**, in which the striations due to the midnight collapse and MSTID bands overlap at least during the passage of MSTID bands, demonstrates that it is almost impossible to differentiate the two. Since the beam sweeps more horizontal arc per unit time at higher altitudes, one would expect to observe, in addition to the features with beam swing period (16 min.), several thin spikes that last shorter in time than the beam swing period. This is especially true for the striations caused by the MSTID bands since the inhomogeneity due to the midnight collapse have a much larger horizontal scale than the one caused by the presence of MSTIDs. In other words, the striations caused by the midnight collapse are mostly dominated by the 16 min. beam swing periodicity, and thus appear thicker than the striations caused by the MSTIDs which are equally affected by two factors: the propagation of the MSTID bands and the swinging of the radar beam. It would not be possible to explain these features without the assistance of the 3D model geometry.

Second, even a single MSTID band could appear complex due to time/space aliasing caused by the beam swing and the southwestward MSTID propagation. As the radar beam, which moves cyclically, goes in and out of a periodic MSTID band, each band in the ISR plot is spread out in time and thus appears as several narrow spikes. This is best demonstrated by the narrow spikes at 24.5-26.5 LT in **Figure 3.9d**, all of which are caused by a single MSTID band observed at 25-26 LT in **Figure 3.9b**. In addition, since at higher altitudes the radar beam rotates faster spatially (covers a larger area per unit time), the higher the altitude the thinner these spikes get (e.g., for a zenith angle of 15º, the radius of the horizontal circle around which the beam swings reaches 134 km at 500 km altitude).

Another common feature is the spike-pairs discussed in detail in **Section 3.1**. Tracking the azimuth-scanning ISR beam in the imaginary allsky images reveals once again that these spike pairs are caused by the beam-reversal around north (e.g., at around 27.25 LT and 27.5 LT in the actual ISR plot in

Figure 3.9c, and at around 22.3 LT, 23.3 LT, 23.5 LT, and 24.3 LT in the imaginary ISR plots in **Figure 3.9d**).

Finally and most importantly, the model further confirms the aforementioned finding that the bands are tilted vertically causing the apparent difference among the height of the spikes in **Figures 3.9c** and **3.9d**. Specifically, the dark spikes in the model ISR data in **Figure 3.9d** are higher in the southern part of an imager band than in the northern part. For example, the (southern) spikes at around 22.1 LT and 22.4 LT are higher than the (northern) spikes at around 22 LT and 22.3 LT.

Even though the simplest model (such as vertical, rectangular MSTID bands) was found to be useful for demonstrating the main features of the ISR observations, the empirical model was modified (e.g., by improving the shape of the modeled MSTID bands) until the model ISR and allsky imager results best replicate the actual observations. Once this is accomplished the resulting 3D geometry can be used to test any physics-based numerical or theoretical model. In other words, although even without the theoretical model support, important results, such as vertical tilt of the MSTID bands, have been found, the empirical model introduced here provides a much easier transition from the observations to the theory, thus simplifying the process of theoretical modeling of the mid-latitude F-region.

4.2. Electrodynamics of MSTIDs

Undoubtedly, in order to fully understand the mid-latitude F-region MSTID bands, the physical generation mechanism must be understood. It is not trivial to explain the electrodynamics of these depletion bands, mainly due to the fact that the actual horizontal and vertical tilts of the bands (~30° and ~12°) are similar to, but somewhat different from, that of the magnetic field-line (11° and 46° respectively). On the other hand, a difference of 20°-35° is relatively small compared to a possible maximum difference of 180°. Consequently, it could be argued that these MSTID bands are not too far from being field-aligned, meaning that the B-field plays a major role as compared to the E-field and the neutral winds (at least one of which must also play a minor role in order to explain the deviation from the field lines). In the literature the most commonly accepted candidate to explain these structures (especially their spatial orientation) has been the Perkins Instability (**Perkins, 1973; Garcia et al., 2000; Zhou et al., 2006**), which inherently assumes small-scale field-aligned irregularities and shows that they grow in time in that particular direction for mid-latitudes. It explains the NW-SE alignment of the bands and, with addition of a polarization electric field (**Kelley and Makela, 2001**), SW propagation but its growth rate is too small and independent of scale.

Numerical solutions of the Perkins equations for simulation of nighttime F-region electrodynamic processes (**Zhou et al., 2005, 2006; Zhou and Mathews, 2006**) indicate that the depletion/enhanced structures (observed in the allsky camera) develop northwest-to-southeast aligned wave fronts that propagate to the southwest in the northern hemisphere (see **Figure 1.9**). These simulations are valid when the F-region is electrodynamically decoupled from the E-region and the conjugate ionosphere. In practice, the numerical simulations are most valid when geomagnetic activity is low and large-scale E-fields are small. However we note that observations have shown strong E/F-region electrodynamic coupling during low Kp, intense spread-F events (**Mathews et al., 2001a; Swartz et al., 2002; Kelley et al., 2003a**). As yet unpublished simulations that involve the solution of the Perkins equations in the presence of horizontal F-region structure indicate that growth rates are significantly larger in this (expected) situation and match observed growth rates (**Zhou et al., 2009**). However, the Perkins Instability does not involve the necessary seeding mechanism, and thus cannot explain the periodic nature of MSTID bands. Moreover, it applies to the nighttime ionosphere only, whereas ISR and GPS-TEC studies have revealed that the MSTIDs also occur throughout the day. Furthermore, the Perkins Instability assumes field-aligned structures by definition giving results in 2D.

Recent papers have linked the MSTID structures with atmospheric gravity waves (AGW), based upon their periodic nature. Gravity wave hypothesis can explain the periodicity and the horizontal wavelength. According to Figure 4 of **Philbrick et al. (1978)**, which shows the horizontal and vertical wavelengths (limited by viscous dissipation and ground reflection) of the propagating modes expected in the mesosphere and lower thermosphere, gravity waves with 1 hour period and vertical and horizontal wavelengths of 10 km and 100 km respectively can easily propagate into the lower thermosphere. However, it is not trivial to understand how gravity waves might reach F-region heights without dissipating. Furthermore, the gravity wave hypotheses cannot explain the very large vertical wavelength of MSTID bands in the F-region and their directionality, which is explained by the Perkins Instability (**Shiokawa et al., 2003a**). Based on these results, it appears that a combination of the two theories is the best explanation for the generation of MSTIDs. More specifically, it is most likely that the MSTID bands presented here are seeded by AGW at upper E-region altitudes, coupled to plasma at higher altitudes due to ion-neutral collisions, and then this modulated plasma obeys mid-latitude nighttime F-region electrodynamics (such as the Perkins Instability) at higher altitudes. This explanation emerges as the best one so far for our dataset and for mid-latitude MSTID bands in general.

Statistical studies show that the MSTID features appear more often and are more intense during the midnight collapse period (e.g., **Shiokawa et al., 2003a**), as can also be observed in **Figures 2.1b** and **3.1**. On the other hand, as discussed in the introduction, **Livneh et al. (2007)** examined ~35 hours of ISR observations on 22-23 March 2004 and showed using a (non-ringing) high-pass filter that the dark bands seen in the ISR data presented in **Figure 2.1b** are actually a part of a continuous wave structure (with ~1 hr period) that persists through the day and extends from the E region through the top of the F-region (see **Figure 1.7**). As the results from the fusion technique described in this study reveal, the dark spikes seen in the ISR data and the depletion bands seen in the allsky images are actually the same phenomenon. On the contrary, it is not yet clear whether the quasi-periodic waves revealed by the high-pass filtered ISR results and the nighttime dark spikes seen in the unprocessed ISR data are also the same phenomenon. However, if they are, it then means that the MSTID bands seen in the allsky images at nighttime actually persist during the day. This is important, since, if this is the case, then the Perkins Instability theory, which works only at nighttime when the E-region and F-region are decoupled, would not be sufficient to explain the electrodynamics of MSTID bands. The properties and possible origins of these waves are extensively discussed in **Livneh et al. (2007, 2009)**. It should be noted that Figure 2 of **Vadas (2007)** gives Acoustic-Gravity Wave (AGW) dissipation heights below 200 km for cold thermosphere (solar minimum) conditions whereas we observe these waves at ~250 km in the camera images and to altitudes in excess of 600 km in the high-pass filtered ISR results. This leads to the conclusion that the collisional coupling between the neutral atmosphere and the F-region plasma weakens rapidly with increasing altitude and that, as pointed out above, the electrodynamics of waves in the nighttime F-region must obey the electrodynamic equations given by **Perkins (1973)** and elucidated in **Zhou et al. (2005, 2006)** and **Zhou and Mathews (2006)**. In particular, to the extent to which the F-region is decoupled from the E-region, the propagation of wavelike features in the F-region is enhanced to the southwest (and northeast) while damped to the northwest/southeast, thus providing a filtering mechanism, as well as a possible amplification (growth/instability) mechanism (e.g., **Taylor et al., 1998**), that certainly influences what we observe with both the ISR and the allsky camera systems. Further, we note that the F-region plasma is incompressible for motions parallel to the geomagnetic field. Thus, as the neutral atmosphere AGW forcing of the plasma decouples at the base of the F-region due to decreasing collision frequency (and also due to altitude progressive AGW losses), the field-aligned plasma motions at the decoupling altitude are imposed on the entire plasma along that flux tube.

Livneh et al. (2009) showed similar periodicities in the solar wind, magnetosphere, and the mid-latitude ionosphere revealing the importance of the coupling mechanisms among these regions. This suggests that the periodic MSTID bands in the ionosphere might have their origins in the magnetosphere and/or solar wind. As discussed in the introduction, there are several ways this coupling might be occurring: the penetration of electric fields across geomagnetic field lines to low L-shells, the modulation of the whole magnetosphere-ionosphere system, or the indirect coupling by the propagation of gravity waves generated in auroral regions (via joule heating and Lorentz force) to mid/low-latitudes without dissipating. An alternate seeding mechanism was proposed by **Shiokawa et al. (2003b)** which showed that an oscillating electric field can also generate the MSTID bands. This finding strengthens the idea that the MSTIDs are generated by the penetration of electric fields across geomagnetic field lines.

Although there has been no previous in-depth study on the correlation between geomagnetic activity and mid-latitude plasma depletion bands, one study showed that when the solar activity is high, the equatorial plumes are observed more often and more toward mid-latitudes (**Sahai et al., 2000**). An examination of geomagnetic activity (e.g., Kp values) in comparison with the strength and occurrence frequency of MSTID activity in the allsky imager (PSASI) dataset supports the idea that these depletion bands appear more intense and more often when Kp is lower (as is the case for both March and June 2004 events). From these, it could be inferred that it becomes more likely to observe MSTID bands instead of equatorial plumes reaching AO latitudes when the geomagnetic activity is low. However, more elaborate research using a larger set of instruments is required in order to better understand this F-region phenomenon, including its day-to-day variability, climatology, seeding mechanism, and relation to solar activity.

4.3. Summary and Conclusions

A common phenomenon of mid-latitudes, MSTID bands, have been investigated in this study. Combining the observational attributes of an allsky imager and an ISR proved to be very useful by revealing that the features seen in the azimuth-scanning ISR data correspond directly to imager features and, most importantly, by additionally providing important clues on the 3D structure of these MSTID bands.

Although there have been many other studies which reported similar MSTID parameters, the study here showed for the first time – via fused ISR and imager data – that the MSTID bands are vertically tilted from north to south. The MSTID observational findings (using the fusion technique described above), which were extensively discussed in **Chapter 3,** are summarized below. These findings form a set of rules for interpretation of ISR data. They are summarized below:

1) The imager and ISR intensity transitions at the southwestern edge of an MSTID band are sharper or steeper than the northeastern edge and the imager MSTID bands are horizontally wider to the south than in the north.
2) Packets of several closely-spaced thin spikes seen in azimuth-scanning ISR actually result from scanning a single MSTID band.
3) The “mirror” or “fork-shaped” spike pairs seen in azimuth-scanning ISR data are due to the ISR beam reversing direction and rapidly moving in and out of a single MSTID band as confirmed by tracking the beam in the allsky images.
4) The weak, (time-wise) thick, high-altitude bands (that appear inverse or shifted relative to the lower altitude bands) with the beam swing period are caused by the horizontal inhomogeneity of the top-side ionosphere which is caused both by the uplifted neighboring MSTID bands and the vertical oscillation of the F-layer. The striations caused by the midnight collapse are more prevalent and appear thicker (in time) because the horizontal scale of the midnight collapse is much larger than the MSTID bands.

5) Most importantly, the bands are found to be tilted not only horizontally (aligned northwest-to-southeast), but also vertically as well, with southern parts of a band reaching a higher altitude than the northern part (vertically tilted upwards by 12° towards magnetic south). The tilt is similar to the dip of the magnetic field lines, though the apparent tilt found from the ISR data is less than the dip angle. A possible explanation for this would be the curvature at the southern tip and the side edges into an elongated bubble shaped depletion.

Based on these results, we suggest that the geometry of the MSTID bands is "vertically tilted bubbles" with the following parameters: northwest-to-southeast aligned at ~20° east of the geomagnetic south, depletion bubbles tilted ~12° vertically from horizontal towards geomagnetic south, 50-250 km (geomagnetic) E-W thickness (thicker at higher altitudes, or lower latitudes), 100-200 km horizontal wavelength in the direction of propagation, 100-200 km/hr horizontal propagation speed, and 1-hr period. These parameters are consistent with previous studies (e.g., **Shiokawa et al., 2003a**). Since the bands are vertically tilted and have the bubble shape, their vertical wavelength seems to vary. As shown in **Figure 3.6**, the lower edges of the bands seem to merge with the depleted E-region at ~ 200 km, otherwise enhanced plasma regions would have been observed below the spikes in the ISR data. Also, the depletions (enhancements) appear in the ISR data to reach from 200-300 km (400-500 km) up to 300-400 km (500-600 km) depending on the altitude of the F-layer (which varies with time due to midnight collapse) and on the position of the band relative to the ISR beam due to the curvature of the southern tip and the sides of the bubble as demonstrated in **Figure 3.6**.

An empirical 3D model of these MSTID bands based on the allsky imager and ISR observations was presented in **Sections 2.3** and **3.2**. The empirical model is needed to interpret the complex ISR data and to fuse the data from the two instruments. The accuracy of the model is tested using a model vertical-looking and beam-swinging ISR and a hypothetical allsky imager to assess whether or not the model results agree with the observations. Using the model azimuth-scanning ISR, it was further confirmed that these MSTID bands are caused by the vertical uplift of the night-time F-layer and they are vertically tilted with the southern part reaching higher altitudes than the northern part. As designed, the synthesized azimuth-scanning ISR results from this model also confirmed and demonstrated all of the aforementioned findings and features of the azimuth-scanning ISR data (multiple spikes, sharp edge, spike pairs, high altitude striations, bubble shape) revealing the true nature of each feature. That is, the model not only provided a 3D picture of MSTID structures, but also served to test the validity of previously observed and predicted properties of the MSTID bands as listed in **Table 2.1**, and summarized earlier in this section.

Based on the model outcome (derived from the imager and ISR data), we suggest that the night-time MSTID bands are vertically-tilted, periodic, bubble-shaped (at the south) slabs caused by the sudden (horizontally sharp) vertical uplift of the F-layer. As stated in **Section 4.1.1**, the vertical tilt also hints at the electrodynamics and origins of MSTID bands. For the specific reasons discussed in the previous section, we believe that the most likely generation mechanism of these night-time mid-latitude MSTID bands would be “atmospheric gravity wave seeded Perkins Instability”. On the other hand the Perkins Instability does not work for the day-time ionosphere and several studies showed that these MSTIDs are formed during the day-time also. In addition, there are clues to the possible origins of MSTIDs in the solar wind and magnetosphere. More elaborate research using a larger set of instruments is required in order to better understand the electrodynamics of this F-region phenomenon and its seeding mechanism. The empirical model introduced here will be useful for future studies of MSTIDs in that it provides a 3D representation of MSTID bands by allowing efficient fusion of ISR and imager results.

The scientific and engineering contributions made by this research activity are summarized below:

Engineering:

- Devised a technique that allows the fusion of allsky imager and azimuth-scanning ISR data.
- Explained the various features observed in the azimuth-scanning ISR data, such as the packets of thinner spikes, mirror-spikes, and high-altitude striations.
- Designed a 3D empirical model based on the imager and radar observations.

Scientific:

- Revealed that the MSTID bands are vertically tilted.
- Showed that the MSTIDs are not simply plasma depletions but rather nearly field-aligned uplifts.
- Illustrated the 3D shape of the MSTID bands.
- Confirmed the observational findings using the model.
- Proved that the high-altitude striations can be caused either by the MSTIDs or the MTM.
- Established a basis for a theory based electrodynamic modeling effort.

4.4. Future Research

The results in this thesis reveal that plenty of information can be learned about F-region MSTIDs by using several instruments together. Using a new technique to combine radar and imager data, new clues to the 3D structure of MSTIDs are found. Most importantly, it is shown for the first time that the southern part of MSTID bands reaches higher altitudes than the northern part. A 3D model of the MSTID bands based on the observations presented here was also introduced. Using a hypothetical azimuth-scanning ISR, it was further confirmed that these MSTID bands are vertically tilted. The model not only confirmed the findings, but also made it possible to better understand the complex azimuth-scanning ISR data. However, it should be emphasized that the dataset here is very limited and it is crucial to analyze a larger dataset with these techniques to obtain more accurate and detailed results.

Since the empirical model is modified until its results agree with the observations, the model can be used as a medium for making the transition from the observations to the theory. Naturally, the next step is to construct a firm theoretical basis that could explain the 3D model results. In other words, the theory will have to be modified until the results agree with the empirical model. When this is accomplished, the MSTID phenomena will be much better understood. That is, previous theories should be further examined and compared to the observations, and if possible, they need to be modified to better agree with the model results.

Since the characteristics of the MSTIDs observed at different mid-latitude locations are very similar, the results from the model will be useful for similar MSTID events observed at other mid-latitude sites (such as Japan, Brazil, and Australia). Furthermore, although the data used are from the mid-latitude F-region, the techniques described here are not limited to F-region or mid-latitudes; they could be applied to any other night-time E-region or F-region phenomenon which can be observed by both radar and imager (e.g., equatorial spread-F plumes).

Although significant progress has been made in understanding the mid-latitude MSTIDs, there are still several important questions that remain unanswered. For example, why do they mostly appear in allsky images from north of Arecibo Observatory (AO), with a typical horizontal tilt, and only when Kp is low? Furthermore, it is yet unknown how long the MSTID bands are along NW-SE due to the limited coverage of a single allsky imager. There are many other basic questions. Why are the imager and ISR intensity transitions at the southwestern edge of an MSTID band sharper or steeper than the northeastern edge? Why are the imager bands horizontally wider to the south than to the north? Why are they not observed at low-latitudes? Why do they appear weaker at high-latitudes? Most importantly, the electrodynamics and generation mechanism of MSTIDs (the source) are still not well known. More specifically, it is not clear what causes the periodicity of these waves and whether they are seeded at lower altitudes (e.g., the mesosphere) or higher altitudes (e.g., the magnetosphere). Furthermore, it is also unknown whether they originate locally at mid-latitudes or propagate from lower (e.g., equatorial) or higher (e.g., auroral) latitudes. Recent studies suggest a connection between the periodicities observed in solar wind, magnetosphere, and ionosphere. However, further research is required to learn more about the ways solar or magnetospheric activity might affect the occurrence and properties of the MSTIDs.

Although the origins of the MSTIDs are not yet clear, several possible explanations have been proposed - Perkins instability, atmospheric gravity waves, and magnetospheric influence - each of which has a different shortcoming. For example, the magnetospheric origin hypothesis might explain the periodicity of MSTIDs but it is not clear how exactly this could happen. On the other hand, Perkins instability can explain the orientation of MSTID bands but its growth rate is too small, it cannot explain the periodicity and scale, works only for the night-time ionosphere, and requires a seeding mechanism. An alternative theory assumes gravity wave seeding from lower altitudes which can explain the periodicity, fast growth rate, and scale, but not the orientation and propagation direction. Consequently, it appears at the moment that the most likely generation mechanism of these mid-latitude MSTID bands is “gravity wave seeded Perkins Instability”. However, extensive theoretical and modeling studies should be done to further strengthen this claim.

On the other hand, it is also quite important to understand the effects of solar activity on the MSTIDs. As stated earlier, preliminary results reveal that, when Kp is high, spread-F plumes are observed with the allsky imager, whereas MSTIDs are observed when it is low, and that MSTIDs are not always observed even when Kp is low. Statistical methods should be used on the imager dataset to further investigate this apparent connection and to reveal how the occurrence and properties of MSTIDs are related to the solar activity. Statistical analysis of MSTIDs could also prove to be very useful to understand the climatology of MSTIDs (e.g., the variability of various properties of the MSTIDs with respect to various conditions such as local time, season, solar activity, and latitude).

Space-based observations are invaluable for revealing the vertical extent of the MSTID signatures and the location of their potential sources in the upper ionosphere, magnetosphere, and solar wind. They can help us understand whether the mid-latitude irregularities are seeded at higher latitudes/altitudes (e.g., via solar wind-magnetosphere-ionosphere coupling), or at lower latitudes (e.g., via gravity waves). A significant advantage of satellite observations is the fact that they can provide global coverage in-addition to in-situ data, both of which are not possible for ground-based instruments. Instruments such as GPS transmitters, magnetometers, plasma probes, interferometers, and imagers aboard satellites can be used to provide useful information such as scintillation, TEC, E-field, B-field, plasma density and drift, energetic particles, temperatures, neutral winds, and airglow.

BIBLIOGRAPHY

Aponte, N., S. A. Gonzalez, M. C. Kelley, C. A. Tepley, X. Pi, B. Iijima, Advection of the equatorial anomaly over Arecibo by small storm related disturbance dynamo electric fields, Geophysical Research Letters, 27, 2833-2836, 2000.

Appleton, E. V., Two anomalies in the ionosphere, Nature, 157, 691, 1946.

Behnke, R. A., F layer height bands in the nocturnal ionosphere over Arecibo, Journal of Geophysical Research, 84 (A3), 974, 1979.

Broadfoot, A. L., and K. R. Kendall, The airglow spectrum, 3100-10,000 Ǻ, Journal of Geophysical Research, 73 (1), 426–428, 1968.

Chamberlain, J. W., Physics of the aurora and airglow", Academic Press, New York, 1961.

Chaturvedi, P. K., and S. L. Ossakow, Nonlinear theory of the collisional Rayleigh–Taylor instability in equatorial spread-F. Geophysical Research Letters, 4, 558, 1977.

Colerico, M. J., M. Mendillo, D. Nottingham, J. Baumgardner, J. Meriwether, J. Mirick, B. W. Reinisch, J. L. Scali, C. G. Fesen, and M. A. Biondi, Coordinated measurements of F region dynamic related to the thermospheric midnight temperature maximum, Journal of Geophysical Research, 101, 26783-26793, 1996.

Forbes, J. M., and R. S. Lindzen, Atmospheric solar tides and their electrodynamic effects. I - the global Sq current system. II - the equatorial electrojet, Journal of Atmospheric and Terrestrial Physics, 38, 897-920, 1976.

Forbes, J. M., The equatorial electrojet, Reviews of Geophysics and Space Physics, 19, 469-504, 1981.

Garcia, F. J., M. C. Kelley, J. J. Makela, and C. -S. Huang, Airglow observations of mesoscale low-velocity traveling ionospheric disturbances at midlatitudes, Journal of Geophysical Research, 105, 18407-18415, 2000.

Hanson, W. B., and R. J. Moffett, Ionization transport effects in the equatorial F region, Journal of Geophysical Research, 71, 5559, 1966.

Herrero, F. A., and J. W. Meriwether, 6300-Å airglow meridional intensity gradients, Journal of Geophysical Research, 85, 4191-4204, 1980.

Jursa, A. S., Handbook of geophysics and the space environment, Air Force Geophysics Laboratory, Springfield, VA, 1985.

Kelley, M. C., J. J. Makela, W. E. Swartz, S. C. Collins, S. Thonnard, N. Aponte, C. A. Tepley, Caribbean ionosphere campaign, year one: Airglow and plasma observations during two intense mid-latitude spread-F events, Geophysical Research Letters, 27, 2825-2828, 2000a.

Kelley, M. C., J. J. Makela, and A. Saito, On the electrical structure of airglow depletion/height layer bands over Arecibo, Geophysical Research Letters, 27, 2837-2840, 2000b.

Kelley, M. C., and J. J. Makela, Resolution of the discrepancy between experiment and theory of midlatitude F-region structures, Geophysical Research Letters, 28, 2589–2592, 2001.

Kelley, M. C., J. J. Makela, and A. Saito, The mid-latitude F region at the mesoscale: some progress at last, Journal of Atmospheric and Solar-Terrestrial Physics, 64, 1525-1529, 2002.

Kelley, M. C., C. Haldoupis, M. J. Nicolls, J. J. Makela, A. Belehaki, S. Shalimov, and V. K. Wong, Case studies of coupling between the E and F regions during unstable sporadic-E conditions, Journal of Geophysical Research, 108(A12), 1447, doi:10.1029/2003JA009955, 2003a.

Kelley, M. C., J. J. Makela, M. N. Vlasov, and A. Sur, Further studies of the Perkins stability during space weather month, Journal of Atmospheric and Solar-Terrestrial Physics, 65, 1071-1075, 2003b.

Kelley, M. C., J. J. Makela, L. J. Paxton, F. Kamalabadi, J. M. Comberiate, and H. Kil, The first coordinated ground- and space-based optical observations of equatorial plasma bubbles, Geophysical Research Letters, 30(14), 1766, doi:10.1029/2003GL017301, 2003c.

Kelley, M., J. J. Makela, J. L. Chau, and M. J. Nicolls, Penetration of the solar wind electric field into the magnetosphere/ionosphere system, Geophysical Research Letters, 30, doi:10.1029/2002GL016321, 2003d.

Kepko, E. L., and H. E. Spence, Observations of discrete, global magnetospheric oscillations directly driven by solar wind density variations, Journal of Geophysical Research, 108 doi:10:1029/2002JA009676, 2003.

Kil, H., S.-Y. Su, L. J. Paxton, B. C. Wolven, Y. Zhang, D. Morrison, and H. C. Yeh, Coincident equatorial bubble detection by TIMED/GUVI and ROCSAT-1, Geophysical Research Letters, 31, L03809, doi:10.1029/2003GL018696, 2004.

Link, R., and L. L. Cogger, A reexamination of the OI 6300-Å nightglow, Journal of Geophysical Research, 93, 9883, 1988.

Livneh, D. J., I. Seker, F. T. Djuth, and J. D. Mathews, Continuous quasi-periodic thermospheric waves over Arecibo, Journal of Geophysical Research, 112, A07313, doi:10.1029/2006JA012225, 2007.

Livneh, D. J., I. Seker, F. T. Djuth, and J. D. Mathews, Omnipresent vertically coherent fluctuations in the ionosphere with a possible worldwide-midlatitude extent, Journal of Geophysical Research, in press, doi:10.1029/2008JA013999, 2009.

Livneh, D. J., Coherent omnipresent fluctuations in the ionosphere, Ph.D. Thesis, Electrical Engineering, The Pennsylvania State University, University Park, PA, 2009.

Makela, J. J., S. A. González, B. MacPherson, X. Pi, M. C. Kelley, and P. J. Sultan, Intercomparisons of total electron content measurements using the Arecibo incoherent scatter radar and GPS, Geophysical Research Letters, 27, 2841-2844, 2000.

Makela, J. J., M. C. Kelley, J. J. Sojka, X. Pi, and A. J. Mannucci, GPS normalization and preliminary modeling results of total electron content during a midlatitude space weather event, Radio Science, 36, 351-361, 2001a.

Makela, J. J., M. C. Kelley, S. A. González, N. Aponte, R. P. McCoy, Ionospheric topography maps using multiple-wavelength all-sky images, Journal of Geophysical Research, 106, 29161-29174, 2001b.

Makela, J. J., B. M. Ledvina, M. C. Kelley and P. M. Kintner, Analysis of the seasonal variations of equatorial plasma bubble occurrence observed from Haleakala, Hawaii, Annales Geophysicae, 22, 3109-3121, 2004.

Makela, J. J., A review of imaging low-latitude ionospheric irregularity processes, Journal of Atmospheric and Solar-Terrestrial Physics, 68(13), 1441-1458, doi:10.1016/j.jastp.2005.04.014, 2006.

Martinis, C., J. Baumgardner, S. M. Smith, M. Colerico, and M. Mendillo, Imaging science at El Leoncito, Argentina, Annales Geophysicae, 24, 1375-1385, 2006.

Martinis, C., and M. Mendillo, Equatorial spread F-related airglow depletions at Arecibo and conjugate observations, Journal of Geophysical Research, 112, doi:10.1029/2007JA012403, 2007.

Mathews, J. D., The incoherent scatter radar as a tool for studying the ionospheric D region, Journal of Atmospheric and Terrestrial Physics, 46, 975-986, 1984.

Mathews, J. D., Incoherent scatter radar probing of the 60-100 km atmosphere and ionosphere, IEEE Transactions on Geoscience and Remote Sensing, GE-24, 765-776, 1986.

Mathews, J. D., Sporadic E: current views and recent progress, Journal of Atmospheric and Solar-Terrestrial Physics, 60, 413-435, 1998.

Mathews, J. D., D. W. Machuga and Q. Zhou, Evidence for electrodynamic linkages between spread-F, ion rain, the intermediate layer, and sporadic E: results from observations and simulations, Journal of Atmospheric and Solar-Terrestrial Physics, 63, 1529-1543, 2001a.

Mathews, J. D., S. Gonzales, M. P. Sulzer, Q.-H. Zhou, J. Urbina, E. Kudeki and S. Franke, Kilometer-scale layered structures inside spread-F, Geophysical Research Letters, 28, 4167-4170, 2001b.

Mendillo, M., J. Baumgardner, D. Nottingham, J. Aarons, B. Reinisch, J. Scali, and M. C. Kelley, Investigations of thermospheric-ionospheric dynamics with 6300-Å images from the Arecibo Observatory, Journal of Geophysical Research, 102, 7331-7343, 1997.

Moore, J. G., E. J. Weber, OI 6300 and 7774 Å airglow measurements of equatorial plasma depletions, Journal of Atmospheric and Terrestrial Physics, Vol. 43, p. 851 – 858, 1981.

Nelson, G. J., and L. L. Cogger, Dynamical behavior of the nighttime ionosphere over Arecibo, Journal of Atmospheric and Terrestrial Physics, 33, 1711, 1971.

Nicolls, M. J., M. C. Kelley, A. J. Coster, S. A. González, and J. J. Makela, Imaging the structure of a large-scale TID using ISR and TEC data, Geophysical Research Letters, 31, L09812, doi:10.1029/2004GL019797, 2004.

Ogawa, T., N. Balan, Y. Otsuka, K. Shiokawa, C. Ihara, T. Shimomai, and A. Saito, Observations and modeling of 630 nm airglow and total electron content associated with traveling ionospheric disturbances over Shigaraki, Japan, Earth Planets Space, 54, 45–56, 2002.

Ogawa, T., E. Sagawa, Y. Otsuka, K. Shiokawa, T. I. Immel, S. B. Mende, and P. Wilkinson, Simultaneous ground- and satellite-based airglow observations of geomagnetic conjugate plasma bubbles in the equatorial anomaly, Earth Planets Space, 57, 385-392, 2005.

Otsuka, Y., T. Kadota, K. Shiokawa, T. Ogawa, S. Kawamura, S. Fukao, and S.-R. Zhang, Optical and radio measurements of a 630-nm airglow enhancement over Japan on 9 September 1999, Journal of Geophysical Research, 108(A6), 1252, doi:10.1029/2002JA009594, 2003.

Otsuka, Y., K. Shiokawa, T. Ogawa, and P. Wilkinson, Geomagnetic conjugate observations of medium-scale traveling ionospheric disturbances at midlatitude using all-sky airglow imagers, Geophysical Research Letters, 31, doi:10.1029/2004GL020262, 2004.

Perkins, F. W., Spread F and ionospheric currents, Journal of Geophysical Research, 78, 218-226, 1973.

Philbrick, C. R., J. P. Noonan, E. T. Fletcher Jr., T. Hanrahan, J. E. Salah, D. W. Blood, R. O. Olsen, B. W. Kennedy, Atmospheric Properties from Measurements at Kwajalein Atoll on 5 April 1978, interim report, Air Force Surveys in Geophysics, 396, 1978.

Philbrick, C. R., F. J. Schmidlin, K. U. Grossmann, G. Lange, D. Offermann, K. D. Baker, D. Krankowsky, U. von Zahn, Density and temperature structure over northern Europe, Journal of Atmospheric and Terrestrial Physics, 47, 159-172, 1985.

Pi, X., M. Mendillo, W. J., Hughes, M. J. Buonsanto, D. P. Sipler, J. Kelly, Q. Zhou, G. Lu, and T. J. Hughes, Dynamical effects of geomagnetic storms and substorms in the middle-latitude ionosphere: An observational campaign, Journal of Geophysical Research, 105, 7403-7417, 2000.

Sahai, Y., P. R. Fagundes, and J. A. Bittencourt, Transequatorial F-region ionospheric plasma bubbles, Journal of Atmospheric and Solar-Terrestrial Physics, 62, 1377-1383, 2000.

Samson, J. C., R. A. Greenwald, J. M. Ruohonniemi, A. Frey, and K. B. Baker, Goose Bay radar observations of Earth-reflected atmospheric gravity waves in the high-latitude ionosphere, Journal of Geophysical Research, 95, 7693-7709, 1990.

Seker, I., Categorization and analysis of the significant results from the Penn State Allsky Imager at Arecibo, M.S. Thesis, Electrical Engineering, The Pennsylvania State University, University Park, PA, 2006.

Seker, I., J. D. Mathews, J. Wiig, P. F. Gutierrez, J. S. Friedman, and C. A. Tepley, First results from the Penn State Allsky Imager at Arecibo Observatory, Earth Planets Space, 59, 165-176, 2007.

Seker, I., D. J. Livneh, J. J. Makela, and J.D. Mathews, Tracking F-region plasma depletion bands using GPS-TEC, incoherent scatter radar, and all-sky imaging at Arecibo, Earth Planets Space, 60, 633-646, 2008.

Seker, I., D. J. Livneh, and J. D. Mathews, A 3D empirical model of F-region MSTID bands using incoherent scatter radar and allsky imaging at Arecibo, Journal of Geophysical Research, in press, doi:10.1029/2008JA014019, 2009.

Shiokawa, K., C. Ihara, Y. Otsuka, and T. Ogawa, Statistical study of nighttime medium-scale traveling ionospheric distrurbances using midlatitude airglow images, Journal of Geophysical Research, 108(A1), 1052, doi:10.1029/2002JA009491, 2003a.

Shiokawa, K., Y. Otsuka, C. Ihara, T. Ogawa, and F. J. Rich, Ground and satellite observations of nighttime medium-scale traveling ionospheric disturbance at midlatitude, Journal of Geophysical Research, 108(A4), 1145, doi:10.1029/2002JA009639, 2003b.

Shiokawa, K., Y. Otsuka, T. Tsugawa, T. Ogawa, A. Saito, K. Ohshima, M. Kubota, T. Maruyama, T. Nakamura, M. Yamamato, and P. Wilkinson, Geomagnetic conjugate observation of nighttime medium-scale and large-scale traveling ionospheric disturbances: FRONT3 campaign, Journal of Geophysical Research, 110, doi:10.1029/2004JA010845, 2005.

Smith, S. M., M. J. Taylor, G. R. Swenson, C. Y. She, W. Hocking, J. Baumgardner and M. Mendillo, A multidiagnostic investigation of the mesospheric bore phenomenon, Journal of Geophysical Research, 108(A2), 1083, doi:10.1029/2002JA009500, 2003.

Swartz, W. E., S. C. Collins, M. C. Kelley, J. J. Makela, E. Kudeki, S. Franke, J. Urbina, N. Aponte, S. Gonzalez, M. P. Sulzer, and J. S. Friedman, First observations of an F-region turbulent upwelling coincident with severe E-region plasma and neutral atmosphere perturbations, Journal of Atmospheric and Solar-Terrestrial Physics, 64, 1545–1556, 2002.

Tascione, T. F., Introduction to the space environment, 2nd ed., Krieger Publishing Company, Malabar, Florida, 1994.

Taylor, M. J., D. N. Turnbill, and R. P. Lowe, Spectrometric and imaging measurements of a spectacular gravity wave event observed during the ALOHA-93 campaign, Geophysical Research Letters, 22, 2849–2852, 1995.

Taylor, M. J., A review of advances in imaging techniques for measuring short period gravity waves in the mesosphere and lower thermosphere, Advances in Space Research, 19, 667-676, 1997.

Taylor, M. J., J.-M. Jahn, S. Fukao, and A. Saito, Possible evidence of gravity wave coupling into the mid-latitude F region ionosphere during the SEEK campaign, Geophysical Research Letters, 25, 1801-1804, 1998.

Thome, G. D., Incoherent Scatter observations of traveling ionospheric disturbances, Journal of Geophysical Research, 69 (19), 4047-4049, 1964.

Tsugawa, T., N. Kotake, Y. Otsuka, Medium-scale traveling ionospheric disturbances observed by GPS receiver network in Japan: a short review, GPS Solutions, 11, 139-144, doi:10.1007/s10291-006-0045-5, 2007a.

Tsugawa, T., Y. Otsuka, A. J. Coster, and A. Saito, Medium-scale traveling ionospheric disturbances detected with dense and wide TEC maps over North America, Geophysical Research Letters, 31, L22101, doi:10.1029/2007GL031663, 2007b.

Vadas, S. L., Horizontal and vertical propagation and dissipation of gravity waves in the thermosphere from lower atmospheric and thermospheric sources, Journal of Geophysical Research, 112, doi: 10.1029/2006JA011845, 2007.

Vlasov, M. N., M. J. Nicolls, M. C. Kelley, S. M. Smith, N. Aponte, and S. A. González, Modeling of airglow and ionospheric parameters at Arecibo during quiet and disturbed periods in October 2002, Journal of Geophysical Research, 110, A07303, doi:10.1029/2005JA011074, 2005.

Wen, C.-H., D. J. Livneh, J. F. Doherty, and J. D. Mathews, Pulse-level interference and meteor processing of Arecibo ISR data, Journal of Atmospheric and Solar-Terrestrial Physics, 69, 973-980, 2006.

Zhou, Q.-N., J. D. Mathews, Q. Du, and C. A. Miller, A preliminary investigation of the pseudo-spectral method numerical solution of the Perkins instability equations in the homogeneous case, Journal of Atmospheric and Solar-Terrestrial Physics, 67, 325-335, 2005.

Zhou, Q.-N., and J. D. Mathews, On the physical explanation of the Perkins instability, Journal of Geophysical Research, 111, A12309, doi:10.1029/2006JA011696, 2006.

Zhou, Q.-N., J. D. Mathews, C. A. Miller, and I. Seker, The evolution of nighttime mid-latitude mesoscale F-region structures: A case study utilizing numerical solution of the Perkins instability equations, Planetary and Space Science, 54, 710-718, 2006.

Zhou, Q.-N., J. D. Mathews, and Q. Du, Linear stage theoretical and numerical solutions of the Perkins instability equations in the inhomogeneous TEC case, Planetary and Space Science, in revision, 2009.

APPENDIX: IDL Code of the Model

```
pro MSTID_model

;adjust color table
device, decomposed=0
loadct, 0

;PARAMETERS
x=200.0 ;along NW-SE
z=500 ;along SW-NE
n=10    ;# of MSTID bands
z1=z/n  ;horizontal wavelength of one MSTID band
ze=15*3.14/180  ;zenith angle of ISR beam (15 deg)
t=800.0 ; # of time steps
swg=1 ;whether the ISR beam is swinging (azimuth-scanning) or fixed (vertical)
pos=99 ;position (along x) of the radar relative to the MSTID
;grid size = 200x200x500 pixels = 500x500x1250 km
;1 pixel = 500/200 = 2.5 km
;total time = 10 hrs
;1 time step = 10*60/t min =  45 sec
;ISR beam full swing period = 30 mins
;azimuth angle step = (600/t)*(360/30) = 9 deg
;MSTID wavelength = 100 km
;MSTID speed = 100 km/hr
;MSTID period = 1 hr

;create ISR array, height (x) vs time (t)
ISR=findgen(t,x)
ISR[*,*]=0

;load the ISR azimuth angle and the 3D MSTID/MTM geometry
restore, 'az.sav'
restore, 'slabg.sav'

window, 2, xsize=800, ysize=1000 ;window for the ISR plot

;move slabs (in time)
for j=0, t-1 do begin
  for h=0,x-1 do begin

    ;swinging ISR beam at certain height (y=h) and time (t=j)
    if (swg EQ 1) then begin
      r=h*tan(ze) ;radius
      ;horizontal location (a,b) of ISR beam at height h and time j
      az0=(az[j]+30)*3.14/180 ;azimuth angle
      e=r*cos(az0) ;x location with respect to radar
      f=r*sin(az0) ;z location with respect to radar/origin
      a=pos+e ;x location with respect to origin
      ;instead of shifting the whole 3D volume, shift the radar beam
      shft=round((z-1)*j/(t-1)) ;the amount/speed of the shift
      b=f+shft ;the new z location

      ;make sure the beam is not outside the volume
      ;this works since the start and end are the same
      if (b LT -0.499) then b=b+500
```

```
      if (b GT 499.499) then b=b-500

      ;get the ISR data at time j, height h, and azimuth angle az0
      ISR[j,h]=slab[round(a),h,round(b)]

    ;vertical ISR beam at certain height and time
    endif else begin
    shft=round((z-1)*j/(t-1))
    ISR[j,h]=slab(pos,h,shft)
    endelse
  endfor

  ;ISR RTI plot at certain h vs time/azimuth
  rdr=rebin(ISR,800,1000) ;enlarge the figure to twice its size
  tv,rdr ;plot it for each time step to avoid waiting for a long time
endfor

;save the ISR result
write_bmp, 'ISR.bmp', rdr

end
```

pro azimuth

```
;set colors
!p.background=16777215
!p.color=0

;parameters
t=600 ;total time in mins
tn=800 ; # of time steps
dt=30 ;ISR beam swing full period (720 deg) in mins
n=t/dt ;# of full periods
dtn=tn/n ;time steps per one full period (720 deg)

;create azimuth array for half period (360 deg)
daz=720/dtn ;angle increment per time step
az0=findgen(dtn/2)*daz
azinv=rotate(az0,2) ;azimuth for the remaining half period (360 deg)
az1=[az0, 360, azinv(0:dtn/2-2)] ;combine the two half to get a full swing (720 deg)
;create t/dt=20 such swings
az2=[az1, az1, az1, az1, az1]
az3=[az2, az2]
az=[az3, az3]

;plot azimuth angle vs time
time=findgen(tn)*10.0/tn+20
window, xsize=1135, ysize=300
plot, time, az, ystyle=1, ytickinterval=30, thick=1.5, font=2, xtitle='Local Time', title='Azimuth Angle';, charsize=3

;save azimuth array
save, filename='az.sav', az

end
```

pro geometry

```
;parameters
```

```
x=200
z=500

;load the background
restore, 'bg_mc.sav'
slab=bg*255
;load the MSTID shape
restore, 'shape.sav'

;implement the uplifts
for i=0,x-1 do begin
  for k=0, z-1 do begin
    slab[i,*,k]=shift(slab[i,*,k],geo[i,k])
    slab(i,0:geo[i,k],k)=0
  endfor
endfor

;save the 3D geometry
save, filename='slabg.sav', slab

end
```

pro background

```
;create the background array
x=200
z=x*2.5
bg=findgen(x,x,z)
bg[*,*,*]=0

;create a sinusoidal nighttime F-layer and midnight collapse
for k=0,z-1 do begin
  for j=70, x-1 do begin
    val=0.5*sin((j-sin(k*3.14/167)*20+260)/20.0)+0.5
    bg(*,j,k)=val
  endfor
  ;clean up the residual at low altitudes
  jj=88+sin(k*3.14/167)*20
  bg(*,0:jj,k)=0
  plot, bg(0,*,k) ;plot the altitude profile vs z-axis
endfor

;show background in y-z plane.
bckg=reform(bg(0,*,*)*255)
tv, rotate(bckg, 1)

;save background ionosphere
save, filename='bg_mc.sav',bg

end
```

pro uplifts

```
;parameters
x=200
z=x*2.5
n=10
```

```
z1=z/n

f=10.0
e1=50.0
e2=20.0
d1=30.0
d3=20.0
d4=60.0
n1=[2,3,4,5]
n0=[10,0,100,50]
nn=size(n1) ;# of slabs
nnn=nn[1]-1

;MSTID surface array
geo=findgen(x,z)
geo[*,*]=0

;shape of MSTID geometry (uplift amount)
for k=0, f-1 do begin

  for i=0, d3-1 do begin
   e=(e1-e2)*i/d3+e2
   d=d1*i/d3
   rise=k*(d/f)
   for n2=0, nnn do begin
    ii=i+n0[n2]
    kk=k+n1[n2]*z1
    if (ii LT 200) then geo[ii,kk]=rise
   endfor
  endfor

  e=e1
  d=d1
  rise=k*(d/f)
  for i=d3, d4-1 do begin
   for n2=0, nnn do begin
    ii=i+n0[n2]
    kk=k+n1[n2]*z1
    if (ii LT 200) then geo[ii,kk]=rise
   endfor
  endfor

  for i=d4, x-1 do begin
   e=(e2-e1)*(i-d4)/(200-d4)+e1
   d=-d1*(i-d4)/(200-d4)+d1
   rise=k*(d/f)
   for n2=0, nnn do begin
    ii=i+n0[n2]
    kk=k+n1[n2]*z1
    if (ii LT 200) then geo[ii,kk]=rise
   endfor
  endfor

endfor

for k=f, z1-1 do begin

  for i=0, d3-1 do begin
   e=(e1-e2)*i/d3+e2
```

```
    d=d1*i/d3
    rise=d*(k-e)/(f-e)
    for n2=0, nnn do begin
      ii=i+n0[n2]
      kk=k+n1[n2]*z1
      if (ii LT 200) and (rise GT 0) then geo[ii,kk]=rise
    endfor
  endfor

  e=e1
  d=d1
  rise=d*(k-e)/(f-e)
  for i=d3, d4-1 do begin
    for n2=0, nnn do begin
      ii=i+n0[n2]
      kk=k+n1[n2]*z1
      if (ii LT 200) then geo[ii,kk]=rise
    endfor
  endfor

  for i=d4, x-1 do begin
    e=(e2-e1)*(i-d4)/(200-d4)+e1
    d=-d1*(i-d4)/(200-d4)+d1
    rise=d*(k-e)/(f-e)
    for n2=0, nnn do begin
      ii=i+n0[n2]
      kk=k+n1[n2]*z1
      if (ii LT 200) and (rise GT 0) then geo[ii,kk]=rise
    endfor
  endfor

endfor

;save MSTID shape
save, filename='shape.sav', geo

end
```

pro display_geometry

```
restore,'shape.sav'

;horizontal tilt and scaling (pixel to km)
geo=rotate(geo, 4)*2.5

;create the axes
a1=90
a2=310
xs=1000
ys=800
window, 1, xsize=xs, ysize=ys
lvl=findgen(115)/2.0+200
x=findgen(a2-a1+1)*2.5
y=findgen(200)*2.5

;animation (rotation)
for j=355,0,-50 do begin
;plot the 3-D MSTID geometry and contours
```

```
result=geo[a1:a2,*]+200
set_shading, /reject, light=[0,1,1], values=[0, 255]
shade_surf, result, x, y, az=j, /save, zrange=[200,315], charsize=4, xtitle='SOUTHEAST', ytitle='SOUTHWEST', thick=3,
charthick=2, zaxis=3, zstyle=1, ztitle='ALTITUDE'
contour, result, x, y, /fill, levels=lvl, /t3d, zvalue=1, /noerase, charsize=4, charthick=2
write_bmp, strcompress(string(1000+j))+'.bmp',tvrd(0,0,xs,ys,1) ;write each frame
endfor

end
```

pro display_cross-sections

```
;load the 3D volume
restore, 'slabg.sav'
;window, 0, xsize=500, ysize=500

z=500
x=400

;enlarge the volume
slabg=rebin(slab,x,x,z)

;this loop allows user to show cross-sections in the each direction
;1 for x, 2 for y, 3 for z, 0 to quit
repeat begin
read, d

;cross-sections along x
;save cross-sections in order to create a movie
if (d eq 1) then begin
for i=0,x-1 do begin
  crossec=rotate(reform(slabg[i,*,*]),4)
  tv, crossec
  write_jpeg,'C:\cross-sec\x\'+strcompress(string(i))+'.jpg', crossec
endfor
endif

;cross-sections along y
if (d eq 2) then begin
for i=0,x-1 do begin
  crossec=rotate(reform(slabg[*,i,*]),4)
  tv, crossec
  write_jpeg,'C:\cross-sec\y\'+strcompress(string(i))+'.jpg', crossec
endfor
endif

;cross-sections along z
if (d eq 3) then begin
for i=0,z-1 do begin
  crossec=slabg[*,*,i]
  tv, crossec
  write_jpeg,'C:\cross-sec\z\'+strcompress(string(i))+'.jpg', crossec
endfor
endif

wdelete, 0
endrep until (d eq 0)
end
```

```
pro display_allsky

;parameters
x=200.0
z=500.0
t=800.0
hmin=100.0
hmax=140.0

;load the 3D volume
restore, 'slabg.sav'

;create imager array
allsky=findgen(x,x) ;single image
alsky=findgen(x,x,21) ;movie

;set the window size
window, 2, xsize=400, ysize=400

;allsky fisheye lens
mask=findgen(x,x)
mask[*,*]=0
for i=0,x-1 do begin
  for j=0, x-1 do begin
    r=sqrt((i-x/2)^2+(j-x/2)^2)
    if (r LT 100) then mask[i,j]=1
  endfor
endfor

;move slabs in time (exposure is 45 sec)
for tt=0, 400,20 do begin
  ;average through airglow layer
  allsky[*,*]=0 ;delete the previous image
  d=round((z-1)*tt/(t-1)) ;amount of propagation
  ;integrating over the airglow layer at time=tt
  for h=hmin,hmax do begin
    slice=reform(slab[*,h,0+d:199+d]) ;horizontal cross-section at h
    allsky=allsky+slice ;integrate corss-sections
  endfor
  ;normalization, orientation, smoothen, and apply allsky mask
  allsky=rotate(allsky,4)/(hmax+1-hmin)
  allsky=rot(allsky, 330, /interp)
  allsky=smooth(allsky,2)*1.5*mask

  asky=rebin(allsky,400,400) ;zoom image
  tvscl, asky ; display image
  alsky[*,*,tt/20]=allsky ;add frame to movie
endfor

;save the movie
;save, filename='allsky.sav',alsky

end
```

VITA

ILGIN SEKER

Educational Experience

2005 – 2009: *PhD,* Communications and Space Sciences Laboratory (CSSL), Electrical Eng., The Pennsylvania State Uni., University Park, PA, *GPA:* 4.00

2003 – 2006: *MSc,* Communications and Space Sciences Laboratory (CSSL), Electrical Eng., The Pennsylvania State Uni., University Park, PA, *GPA:* 4.00

1999 – 2003: *BSc,* Electrical and Electronics Eng., The Middle East Technical Uni., Ankara, Turkey, *GPA: 3.84*

1999 – 2003: *Minor (Certificate),* Physics, The Middle East Technical Uni. Ankara, Turkey, *GPA: 3.43*

Professional Experience

2003 – 2009: *Graduate Research Assistant*, Communications and Space Sciences Laboratory (CSSL), Electrical Eng., The Pennsylvania State Uni., University Park, PA, *Supervisor:* Prof. John D. Mathews

2007: *Resident Graduate Student,* five months, Arecibo Observatory, Arecibo, PR

2004: *Summer Graduate Student,* six weeks, Arecibo Observatory, Arecibo, PR

2002: *Summer Internship,* one month, Turkey Radio and Television Network (TRT), Ankara, Turkey

2001: *Summer Internship,* one month, Microelectronics, Guidance and Electro-Optics (MGEO) Division, ASELSAN, Ankara, Turkey

Journal Publications

Seker, I., D. J. Livneh, and J. D. Mathews, A 3D empirical model of F region Medium-Scale Traveling Ionospheric Disturbance bands using incoherent scatter radar and all-sky imaging at Arecibo, *J. Geophys. Res.*, 114, A06302, doi:10.1029/2008JA014019, 2009.

Seker, I., D. J. Livneh, J. J. Makela, and J. D. Mathews, Tracking F-region plasma depletion bands using GPS-TEC, incoherent scatter radar, and all-sky imaging at Arecibo, *Earth Planets Space*, 60, 2008.

Seker, I., J. D. Mathews, J. Wiig, P. F. Gutierrez, J. S. Friedman, and C. A. Tepley, First results from the Penn State Allsky Imager at Arecibo Observatory, *Earth Planets Space*, 59, 2007.

Livneh, D. J., *I. Seker*, F. T. Djuth, and J. D. Mathews, Omnipresent vertically coherent fluctuations in the ionosphere with a possible worldwide-midlatitude extent, *J. Geophys. Res.*, 114, A06303, doi:10.1029/2008JA013999, 2009.

Livneh, D. J., *I. Seker*, F. T. Djuth, and J. D. Mathews, Continuous quasi-periodic thermospheric waves over Arecibo, *J. Geophys. Res.*, 112, A07313, doi:10.1029/2006JA012225, 2007.

Zhou, Q.-N., J. D. Mathews, C. A. Miller, and *I. Seker*, The evolution of nighttime mid-latitude mesoscale F-region structures: A case study utilizing numerical solution of the Perkins instability equations, *Planetary and Space Science*, 54, 710-718, 2006.